Experiments on two-component quantum gases on an atom chip

ACADEMISCH PROEFSCHRIFT

ter verkrijging van de graad van doctor
aan de Universiteit van Amsterdam
op gezag van de Rector Magnificus
prof. dr. D.C. van den Boom
ten overstaan van een door het college voor promoties ingestelde
commissie, in het openbaar te verdedigen in de Agnietenkapel
op dinsdag 4 december 2012, te 12:00 uur

door

Philipp Wicke

geboren te Kiel, Duitsland

Promotiecommissie:

Promotor: prof. dr. J.T.M. Walraven
Co-promotor: dr. N.J. van Druten

Overige leden: prof. dr. H.-C. Nägerl
prof. dr. G. Shlyapnikov
prof. dr. H.B. van Linden van den Heuvell
prof. dr. M.S. Golden
prof. dr. J.-S Caux

Faculteit der Natuurwetenschappen, Wiskunde en Informatica

ISBN: 978-94-6191-502-3

Cover photo: Katja Weber, Lago de Atitlán/Guatemala, 2004

The work described in this thesis was carried out
in the group “Quantum Gases & Quantum Information”, at the
Van der Waals-Zeeman Instituut of the University of Amsterdam,
Science Park 904, 1098 XH Amsterdam, The Netherlands,
where a limited number of copies of this thesis is available.
A digital version of this thesis can be downloaded from
`http://iop.uva.nl`
or: `http://dare.uva.nl`
This work is part of the research programme of the
Foundation for Fundamental Research on Matter (FOM),
which is financially supported by the Netherlands Organization
for Scientific Research (NWO).

Contents

Chapter 1

Introduction

The wave-particle duality is deeply embedded in quantum mechanics. It attributes wave character to every particle and vice-versa. For particles, this is enshrined in the famous relation named after Louis de Broglie, who proposed that the quantum wavelength λ associated to an object with momentum p is given by $\lambda = h/p$, where h is Planck's constant. It becomes shorter as mass and velocity get larger. This is the reason why we usually do not experience quantum mechanical effects in everyday life. We are used to massive objects being exactly located in space and time and moving along well-described trajectories. This changes however when small objects or even single atoms at low energies are studied. Under appropriate conditions, atoms can then no longer be regarded as localized particles. Instead, they can be described in terms of waves whose amplitude contains information about the probability of an atom being at a certain position. Typical wave phenomena such as interference and diffraction can then be observed with matter.

A further consequence of the quantum mechanical character of nature is exhibited when a thermal ensemble of identical particles is cooled to sufficiently low temperatures. One can associate a characteristic quantum wavelength, the *thermal* de Broglie wavelength, with the temperature. One can think of this wavelength as the distance around the notional position of the object where its quantum behavior may be observed. Quantum phenomena now dominate when the thermal de Broglie wavelength becomes larger than the average inter-particle distance. The indistinguishability of the particles becomes essential and they can no longer be described individually. Instead, collective behavior emerges with often very peculiar properties, that persists at the macroscopic scale and in the presence of (even strong) interactions. Examples of such *macroscopic quantum phenomena* are the superfluid flow of liquid helium, and superconductivity in certain solid-state materials. These are dramatic illustrations of the role of quantum mechanics in objects with a scale that is visible with the naked human eye. Over the last two decades, quantum gases have emerged as profound new systems in which macroscopic quantum phenomena can be observed.

1.1 Quantum gases

The most basic form of a macroscopic quantum phenomenon was predicted by A. Einstein in 1924/25 [1, 2, 3]. Inspired by the work of S.N. Bose on the quantum statistics of light [4], Einstein considered a somewhat different system, namely that of a gas of indistinguishable massive particles where the number of particles is conserved. Einstein found that when such a gas is cooled below a certain critical temperature, there is a sudden change in behavior, where a large (macroscopic) fraction of the atoms occupies the single particle ground state. This fraction can then be considered as a single, macroscopically occupied matter wave. This behavior, which is now known as Bose-Einstein condensation (BEC) is typical for bosons, particles with integer spin. It is at the heart of the phenomena of superfluidity and superconductivity. However, it had not been realized in its most pure form (in an ultra-cold gas) until 1995, when advances in laser cooling and evaporative cooling as well as magnetic and optical trapping of neutral atoms allowed for the first experimental realization of BEC [5, 6, 7]. Since these first experiments the field of ultra cold atomic physics or quantum gases has made overwhelming progress. The preparation of degenerate quantum gases has become a standard procedure in hundreds of laboratories throughout the world [8, 9].

After the basic properties of these systems were studied, the field has developed in many directions: The cooling techniques that led to BEC were also applied to fermions, neutral atoms with half-integer spin obeying Fermi-Dirac statistics, forbidding two identical particles to be in the same quantum state. This led to the realization of degenerate Fermi gases [10] and ultra-cold mixtures of bosons and fermions [11, 12, 13, 14, 15, 16].

Nowadays, quantum gases are increasingly used as model systems for interacting many-body systems. An important mechanism to tune interactions, that is extensively used, is employing a so-called Feshbach resonance [17]. Modifying the strength of interatomic interactions and even changing between attractive and repulsive interactions, is achieved by simply adjusting the magnitude of the background magnetic field. This has led to e.g. the observation of the BEC-BCS crossover between a BEC of strongly paired fermions forming composite bosonic molecules to weakly paired fermions obeying BCS theory [18, 19, 20]. Long-range dipolar (anisotropic) interactions are studied in systems of degenerate atoms with high magnetic dipole moments, in particular chromium [21, 22] and cold Rydberg atoms [23, 24]. Spinor quantum gases, where atoms are in a superposition of internal quantum states, offer the opportunity to study the interplay between internal (spin) and external (motion) degrees of freedom [25, 26, 27, 28, 29, 30, 31, 32, 33].

Advances in optical and magnetic trapping of ultra-cold gases have played an essential role in opening up novel avenues in quantum many-body physics by providing experimental access to new physical regimes [8]. In particular, one-dimensional (1D) quantum gases, can be created by restricting the motion in the two transverse directions using optical lattices or atom chips (see following section). Such 1D gases exhibit a surprisingly rich variety of regimes not present in 2D or 3D [34, 35, 36, 37, 38, 39, 40, 41, 42]. For example, a 1D Bose gas becomes more *strongly* interacting as the density *decreases*. Furthermore, the many-body eigenstates and thermodynamic properties of these 1D systems can often be described using exact *Bethe Ansatz* methods [43, 44, 45, 46, 47], and direct comparisons between theory and experiment are possible [38, 48, 40, 41, 30, 33]. Adding the possibility to dynamically control the strength of atomic interactions, for example via Feshbach resonances [30, 49, 50, 17], there is now a strong impetus to extend these experimental and theoretical studies to non-equilibrium dynamics [51, 30, 52].

As sketched above, experiments on ultra-cold gases offer unparalleled opportunities to explore quantum many-body physics, with excellent control over key parameters including temperature, density, interactions and even dimensionality.

Besides the fundamental research along the directions contoured above, there is a growing number of applications for quantum gases. Neutral atoms are a promising candidate for quantum information processing (QIP). Their weak interactions with the environment and among themselves result in long lived internal and external states, required for the storage and manipulation of quantum information [53, 54, 55, 24, 56]. The coherence property of BECs can be utilized to build highly sensitive sensors for interferometrically measuring magnetic fields and inertia [57, 58]. The latter, sensing local gravitation is for instance helpful in oil resource development, while sensing rotation with gyroscopes based on quantum gases [59] could improve inertial navigation in aircraft. Furthermore, ultra-cold gases employed in atomic clocks offer increased accuracy. The International System of Units (SI) has defined the second based on a microwave transition frequency in Cesium. Standard atomic clocks are based on measuring this frequency. Using higher frequency optical transitions in an ultra-cold gas of atoms one can substantially increase accuracy and reduce Doppler shifts as well as collisional shifts [60]. Recently, the noise of such clocks has been reduced to below the standard quantum limit by using spin-squeezed states [61, 62]. Improved atomic clocks installed in navigation satellites would lead to a greatly enhanced positioning precision.

1.2 Toolbox for atom manipulation

The main tools for manipulating ultra-cold atoms are optical (laser) fields and (DC and AC) magnetic fields. Both can be used to generate low-dimensional quantum gases and create state-dependent potentials.

Optical fields shift the energy of the electronic ground state via the AC Stark effect. In particular, standing waves of coherent light are used to generate optical lattices: one-, two- or three-dimensional periodic potentials for neutral atoms [63]. With this technique key properties of quantum systems like the superfluid to Mott-insulator transition became measurable for the first time [64, 65]. Likewise, the high degree of control and the absence of impurities make these systems ideal simulators for solid state systems. A prime example for this is research undertaken [66] to help understand the transition from the antiferromagnetic to the superconducting phase in cuprate (CuO) compounds by mimicking this system with two-component Fermi-mixtures loaded into optical lattices, potentially shedding light on high-Tc superconductivity. Furthermore, state-dependent optical lattice potentials have previously found use for spin-dependent transport and entanglement of atoms [67, 68] and are promising candidates for the implementation of quantum gates in QIP [69]. Generally, the use of optical traps allows freedom in the choice of the magnetic field, and hence permits the use of Feshbach resonances. The main limitation is then that only a single control parameter (the magnetic field strength) is available and a suitable Feshbach resonance needs to be available for the atomic system under study.

Another approach to manipulating ultra-cold atoms is based on micro-fabricated wire and/or permanent magnet patterns [70, 71, 72]. With these so-called atom chips, atoms can be trapped in strong magnetic gradients at a distance of a few to a few hundred μm from the chip surface. Employing multiple layers of wires, almost arbitrary potential landscapes can be realized, including conveyor belts for atoms [73], on-chip single atom detectors [74] and interferometers [75, 76].

In addition to magnetostatic potentials, alternating electrical currents can be applied to the wires of an atom chip, to produce strong radio-frequency (RF) or microwave (MW) near-fields. Coupling the Zeeman levels of trapped atoms by means of a RF magnetic field, results in a modified potential.

This is implicitly used in RF-induced evaporative cooling in magnetic traps [77, 78].Its use for modifying the trap minimum was investigated by Zobay and Garraway [79] with a spatially homogenous RF field. Later, a full description of these adiabatic RF induced potentials taking into account the full vector nature of the electromagnetic field was worked out [80]. By using RF induced potentials in a pioneering experiment, for the first time a coherent on-chip beam splitter for neutral atoms was demonstrated [81]. Another useful property of RF potentials is their inherent state-dependence. The coupling of the atomic state depends on the ellipticity of the RF polarization through the sign of the g-factor. Recently, state-dependent microwave dressing was used to generate spin squeezing in 3D Bose-Einstein condensates by varying the wavefunction overlap for two hyperfine states to control collisions [82, 61], and state-dependent potentials created by combining an optical trap with a magnetic field gradient were used to obtain record low spin temperatures via spin gradient demagnetization cooling of a quantum gas [83].

1.3 This thesis

In this work, we study the (thermo)dynamics of a two-component Bose gas in one dimension. For generating the one-dimensional magnetic trap we employ an atom chip. As experimental system we chose the two magnetically trappable clock states in ^{87}Rb [27, 29], in part because they experience equal trapping potentials and have nearly spin-independent interactions [84, 85, 86]. The drawback of this choice is that no convenient Feshbach resonances are available for these states, preventing precise control of the three relevant (inter and intra-state) interaction strengths. We show how this limitation is overcome by use of the aforementioned state-dependent RF potentials.

As a main result we show a new way to tune interactions in one-dimensional quantum gases using state-dependent dressed potentials, enabling control over non-equilibrium spin motion in a two-component gas of ^{87}Rb. The accessible range includes the point of spin-independent interactions where exact quantum many-body solutions are available via the Bethe Ansatz and the point where spin motion is frozen. This versatility opens a new route to experiments on spin waves and the relation between superfluidity and magnetism in low-dimensional quantum gases.

This thesis is organized as follows: **Chapter 2** summarizes the theory needed to explain and model the experiments described in this thesis. After a brief discussion of the theory of trapping ultra-cold atoms in static magnetic potentials, the focus is shifted to radio-frequency adiabatic potentials and their state-dependent character. Next, potential-dependent effective interaction parameters and a formalism of coupled Gross-Pitaevskii (GP) equations for one-dimensional Bose gases are introduced to show a new way to tune interatomic interactions using state-dependent RF potentials. To characterize the behavior of a 1D two-component gas, the concept of a spin velocity is developed, leading to a diagram identifying different regimes for the system studied.

In **chapter 3**, the apparatus used to perform the experiments described in this thesis is detailed. After a brief discussion of the vacuum system, the laser system, the atom chip and RF generation, the generation and application of microwave radiation is described in detail. Furthermore, an optical system for imaging along the 1D axis and a superimposed optical lattice are characterized. The chapter ends with a summary of the experimental sequence used to attain a 1D two-component Bose gas.

Chapter 4 presents a series of experiments performed to produce a one-dimensional two-component gas in thermal equilibrium. The experimental data is characterized employing models based on the solutions from Bethe Ansatz theories.

Chapter 5 presents the main results of this work. Spin motion in a 1D gas after a sudden change in internal states is shown to lead to a focus in the density of one component. After a characterization of state-dependent RF potentials, two situations are emphasized for the changes in the spin evolution. These situations correspond to equal interactions between the atoms and equal effective potentials. The coupled one-dimensional GP equations are shown to model the experiments with excellent accuracy. The chapter concludes with an outlook.

A design of a novel atom-chip based apparatus for experiments with Bose-Fermi (and Bose-Bose) mixtures (namely ^{87}Rb and ^{40}K) is described in **chapter 6**.

Appendix A provides detailed information about the experimental sequence used to generate the two-component quantum gases, studied in this thesis. Special emphasis is given to the technical details on creating RF induced state-dependent potentials and state-selective imaging.

Chapter 2

Theoretical background

2.1 Introduction

This chapter provides the theoretical background relevant to the experiments described in subsequent chapters, in particular chapter 5. After a brief discussion of magnetic trapping of neutral atoms in section 2.2, radio-frequency (RF)-dressed potentials are introduced with a focus on state-dependent potentials in section 2.3. In section 2.4 we show how the effective interatomic interactions in a Bose gas change when the trapping potential is reduced to one dimension. This description is extended in section 2.5 to a two-component system, enabling us to treat two different internal states in a 1D situation. Section 2.6 combines the previous sections to show how RF-dressing causes modified potentials which enable tuning of the interatomic interactions in one dimension (section 2.7).

2.2 Trapping of ultra-cold atoms

The Zeeman shift can be utilized to trap neutral atoms. The internal energy of atoms depends on the interaction of the magnetic moments μ with an external magnetic field $\mathbf{B}$. An atom with total electronic angular momentum $\mathbf{J}$ and nuclear spin $\mathbf{I}$ has total spin $\mathbf{F} = \mathbf{I} + \mathbf{J}$ with values for F from $|I - J|$ to $I + J$. For weak magnetic fields, specific Zeeman states are conveniently labeled by F and m_F, the projection of $\mathbf{F}$ on the direction of the magnetic field $\mathbf{B}$, where the magnetic quantum number m_F ranges from $-F, ..., F$.

Experiments described in this thesis were exclusively performed with the electronic ground state of ^{87}Rb ($J = 1/2, I = 3/2$), so that $F = 1$ or $F = 2$. The Zeeman level structure of these states is schematically indicated in figure 2.1. For modest field strengths, where the hyperfine splitting of the ground state ($h \times 6.83468\,\mathrm{GHz}$) is much larger than the Zeeman energy, the Zeeman shifts are approximately linear in $|\mathbf{B}|$ and the interaction energies become

$$U_{mag}(r) = -\boldsymbol{\mu} \cdot \mathbf{B} = g_F m_F \mu_B |\mathbf{B}(r)|, \tag{2.1}$$

with g_F and μ_B denoting the Landé g-factor for a specific F and the Bohr magneton, respectively. Zeeman states for which the interaction energy increases with the magnitude of the magnetic field are called "low-field seeking states". They can be trapped in a magnetic field minimum. For ^{87}Rb these states are $|F, m_F\rangle = |2, 2\rangle$, $|2, 1\rangle$ and $|1, -1\rangle$.

A magnetic field with a local minimum to trap neutral atoms is most easily realized by

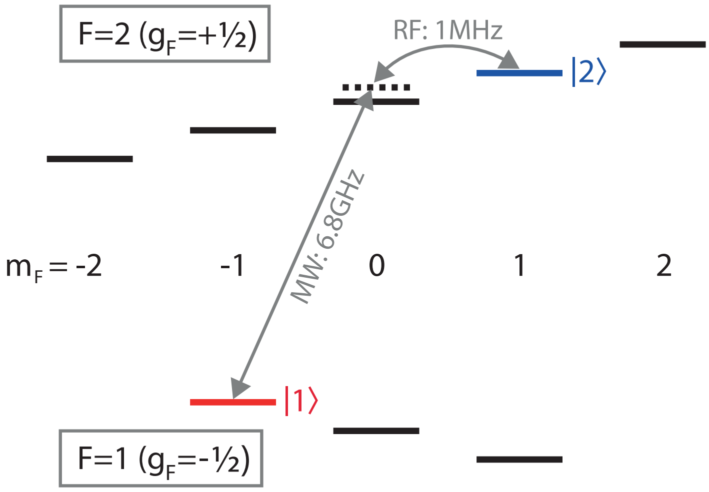

Figure 2.1: Level diagram (not to scale) of the $^5S_{1/2}$ electronic ground state of ^{87}Rb. The degeneracy of the magnetic sublevels is lifted by a magnetic field of 3.23 G. States $|1\rangle = |F\!=\!1, m_F\!=\!-1\rangle$ and $|2\rangle = |F\!=\!2, m_F\!=\!1\rangle$ are highlighted in red and blue, respectively. These states constitute the two-component system being of central importance to this work. They are coupled via a two-photon microwave/radio frequency transition (see chapter 3.2), as indicated by the grey arrows.

two coils in anti-Helmholtz configuration. The resulting spherical quadrupole trap has a central point where the fields exactly cancel to zero and from where the modulus of the field increases linearly in all directions. Strictly speaking, equation (2.1) only holds if the magnetic quantum number is a constant of motion, i.e. when the spin adiabatically follows the direction of **B**. If, however, an atom enters a region where the magnetic field is small ($|B(r)| \simeq 0$) and its Larmor frequency

$$\omega_L = |g_F \mu_B B|/\hbar \tag{2.2}$$

is small compared to the rate of change of the magnetic field as seen from the rest frame of the atom, there is a high probability for the atom to undergo a spin-flip transition to an untrapped state. To prevent these so-called Majorana losses the adiabaticity condition

$$\omega_L \gg |\frac{d}{dt}\mathbf{B}|/|\mathbf{B}| \tag{2.3}$$

has to hold at all times. One way of achieving this is enhancing the quadrupole potential to a Ioffe-Pritchard(IP) potential, which has a non-zero minimum in $|\mathbf{B}|$.

This type of potential has first been devised by Ioffe for plasma trapping [87] and later adapted by Pritchard for neutral atoms [88]. The trap consists of a two-dimensional quadrupole field in the radial direction ($\rho = \sqrt{y^2 + z^2}$) with gradient $\alpha = (\partial B_\perp/\partial\rho)_{x=x_0}$ and a harmonic potential with curvature $\beta = (\partial^2 B_x(0,0,x)/\partial x^2)_{x=x_0}$ plus a constant field B_0 along the axial direction (x). In polar coordinates, the magnetic field can be expressed as [89]

$$\begin{aligned} B_\perp(\rho,\phi,x) &= \alpha\rho\sin(2\phi) - \tfrac{1}{2}\beta\rho(x-x_0), \\ B_\phi(\rho,\phi,x) &= \alpha\rho\cos(2\phi), \\ B_\parallel(\rho,\phi,x) &= B_0 + \tfrac{1}{2}\beta(x-x_0)^2 - \tfrac{1}{4}\beta\rho^2. \end{aligned} \tag{2.4}$$

Depending on the temperature of the atoms, this trap shows two different regimes: Hot atoms with a temperature $T \gg \mu_B B_0/k_B$ experience a linear potential in the radial direction and a harmonic potential in the axial direction. On the other hand, cold atoms with $T \ll \mu_B B_0/k_B$ (positioned at the very bottom of the potential), are exposed to an anisotropic potential which is approximately harmonic in all directions. The harmonic approximation of such a potential is

$$U(x,y,z) \approx U_0 + \frac{1}{2}m\omega_x^2 x^2 + \frac{1}{2}m\omega_y^2 y^2 + \frac{1}{2}m\omega_z^2 z^2, \tag{2.5}$$

where m is the atomic mass and ω_i are the single-particle oscillator frequencies or trap frequencies. From this, together with equations (2.1) and (2.4), the axial and radial trap frequencies are found to be

$$\omega_\parallel = \sqrt{\frac{g_F m_F \mu_B}{m}\beta}, \tag{2.6}$$

$$\omega_\perp = \sqrt{\frac{g_F m_F \mu_B}{m}(\frac{\alpha^2}{B_0} - \frac{\beta}{2})}. \tag{2.7}$$

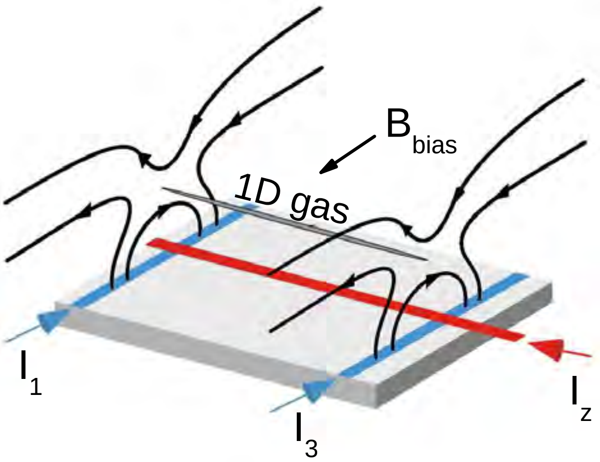

Figure 2.2: Schematic of an atom chip based magnetic trap (adapted from [90]). The circular field generated by current I_z superimposed with the homogeneous external field B_{bias} results in a linear quadrupole field at a certain height above the wire. The currents I_1 and I_3 provide longitudinal trapping along I_z.

One-dimensional microtraps on atomchips

Throughout this work, microtraps created by “atom chips” (see figure 2.2) are used to generate Ioffe-Pritchard potentials for trapping. The benefit of such traps becomes apparent when one looks at the gradient generated by a single wire

$$\alpha = \frac{\mu_0 I}{2\pi r^2}. \tag{2.8}$$

Reducing the dimensions of the field-generating element and trapping atoms only micrometers away from it results in very steep potentials. This facilitates evaporative cooling and, by providing extremely anisotropic confinement, atom chips are naturally suited to study quantum gases in (quasi) 1D geometries.

For instance, the condition for being thermally in the 1D regime is $k_B T < \hbar\omega_\perp$, which is easier to achieve when $\omega_\perp$ is high. Typically, in our experiments, we have $\omega_\perp \approx 2\pi \cdot 2\,\mathrm{kHz}$, which translates to a 3D-1D crossover temperature of $\hbar\omega_\perp / k_B = 100\,\mathrm{nK}$.

2.3 State-dependent RF-dressed potentials

Evaporative cooling [78, 77], the technique that made possible the last step in phase space density from a cold gas to a Bose-Einstein condensate (BEC), is now commonly used in experiments involving ultracold gases. It relies on coupling hot atoms in trapped states to untrapped states. In magnetic traps this is typically done by means of radio-frequency (RF) or less frequently microwave (MW) transitions. In this manner hot atoms are selectively removed from the trap. The remaining atoms rethermalize via collisions, resulting in cooling.

In 2001, radio-frequency coupling was also proposed for the generation of two-dimensional trapping geometries [79]. In this context one speaks of RF-dressed potentials, refering to the dressed-atom picture developed by Cohen-Tannoudji [91, 92]. Figure 2.3 describes how the coupling of a (quantized) radiation field to an atom with quantized internal states leads to new, so-called dressed states. While the quantized nature of radiation is not needed for our purposes, the dressed atom description remains relevant. RF-dressed potentials have been used in a number of experiments, most prominently to create double-well potentials for matter-wave interference [81]. A detailed theoretical treatment of RF-dressed potentials can be found in references [80, 93].

In a situation with only a static magnetic field present, virtually no changes of the internal state occur as the atom moves in the trap, as long as the adiabaticity condition (2.3) holds throughout the motion. This changes when an oscillating radio-frequency field with a frequency ω_{rf} close to the Larmor frequency couples the Zeeman states. Given a linear Zeeman shift, there is only one resonance frequency which couples all levels within a manifold. For a linearly polarized RF-field with a single frequency ω_{rf}, the dressed potential depends on the detuning $\Delta = \omega_{rf} - \omega_L$ from the Larmor frequency and the strength of the coupling, characterized by the Rabi frequency

$$\Omega_{lin} = \frac{|g_f|\mu_B}{2\hbar} \frac{|\mathbf{b}_{rf} \times \mathbf{B}|}{|\mathbf{B}|}, \tag{2.9}$$

with $\mathbf{b}_{rf}$ the vector field of the magnetic part of the RF-field. Equation (2.9) indicates that only the part of $\mathbf{b}_{rf}$ which is perpendicular to the local direction of the static magnetic field $\mathbf{B}$ contributes to the dressing. This fact can be utilized to engineer rather counter-intuitive trap shapes [94], which cannot be realized by static magnetic trapping alone.

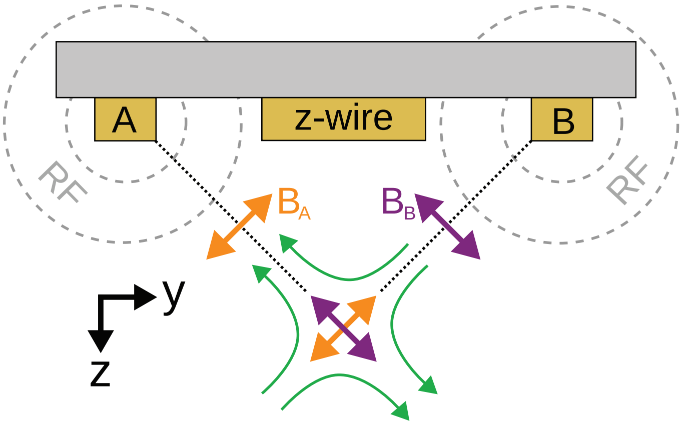

Figure 2.3: Cross section of the atom chip used for generating RF-dressed potentials. The magnetic quadrupole field, indicated by green arrows, is provided by the z-wire and an external bias field (see figure 2.2). We attach the outer chip wires A and B to a RF source. The RF polarization in the y-z-plane is indicated by orange and purple arrows. It results from a superposition of the two fields involved. By varying the relative phase or the amplitudes of the RF currents through the individual wires, the polarization can be set arbitrarily.

In the experiments described in this thesis, the RF field originates from two parallel wires on the atom chip (see figure 2.3). The local magnetic field consists of a static and an oscillating part

$$\mathbf{B}(\mathbf{r}) = \mathbf{B}_{static}(\mathbf{r}) + \mathbf{B}_{rf}(\mathbf{r}). \tag{2.10}$$

The static field is generated by running a constant current through the center z-shaped wire, while the RF field is a superposition of the fields radiated by the neighboring wires which are labeled A and B

$$\mathbf{B}_{rf}(\mathbf{r}) = \mathbf{B}_A(\mathbf{r}) \cos(\omega t + \phi_A) + \mathbf{B}_B(\mathbf{r}) \cos(\omega t + \phi_B). \tag{2.11}$$

In complex notation, equation (2.11) becomes

$$\mathbf{B}_{rf}(\mathbf{r}) = \mathbf{b}_{rf}(\mathbf{r}) e^{i\omega t} + \mathbf{b}^*_{rf}(\mathbf{r}) e^{-i\omega t}, \tag{2.12}$$

with $\mathbf{b}_{rf}$ a complex-valued vector. This can be decomposed into a sum of right-circular and left-circular RF fields, where the circularity is defined with respect to the direction of $\mathbf{B}_{static}$

$$\mathbf{b}_{rf} = b_+\hat{\mathbf{e}}_+ + b_-\hat{\mathbf{e}}_-, \tag{2.13}$$

with $\mathbf{b}_\pm$ two complex-valued amplitudes. Taking a local coordinate system with $\hat{\mathbf{x}}$ along $\mathbf{B}_{static}$, the circular unit vectors $\hat{\mathbf{e}}_+$ and $\hat{\mathbf{e}}_-$ can be written as

$$\hat{\mathbf{e}}_\pm = \frac{1}{\sqrt{2}}(\hat{\mathbf{y}} \mp i\hat{\mathbf{z}}). \tag{2.14}$$

The amplitudes of the right- and left-circular components of the RF field can now be obtained by projection onto the unit vectors:

$$b_\pm(\mathbf{r}) = \hat{\mathbf{e}}^*_\pm(\mathbf{r}) \cdot \mathbf{b}_{rf}(\mathbf{r}). \tag{2.15}$$

We now consider magnetically trapped atoms in the states $i = \{1, 2\}$ corresponding to $|1\rangle = |F = 1, m_F = -1\rangle$ and $|2\rangle = |F = 2, m_F = 1\rangle$ of ^{87}Rb. Since the states have opposite g-factors $g_{F,1} = -1/2$ and $g_{F,2} = +1/2$, they couple differently to the RF field. The Rabi-frequency Ω_1 depends on the projection of the negative circular polarization component of the RF field on the direction of the local static field (assumed to be along z), whereas Ω_2 depends on the positive circular component. The corresponding Rabi-frequencies are

$$\Omega_{1,2} = |g_F|\mu_B|b_{+,-}|/\hbar. \tag{2.16}$$

This leads to state-dependent RF-dressed potentials

$$U_i = \tilde{m}_f\sqrt{(\hbar\omega_L - \hbar\omega_{rf})^2 + \hbar^2\Omega_i^2}, \tag{2.17}$$

where ω_L denotes the Larmor frequency and ω_{rf} is the radio frequency used for dressing the atomic states.

2.4 Effective interactions in 1D

The properties of quantum gases change drastically with dimensionality. In the three-dimensional (3D) case, a gas of weakly interacting bosons at zero temperature can be described by a mean-field theory where the local chemical potential becomes $\mu(r) = n(r)g$, with 3D density n and interaction parameter

$$g_{3D} = \frac{4\pi\hbar^2 a}{m}. \tag{2.18}$$

Here, a denotes the s-wave scattering length. The global ground state of the system is described by the time independent Gross-Pitaevskii (GP) equation [95, 96] for the mean field wavefunction $\Psi(\mathbf{r})$

$$\left[-\frac{\hbar^2}{2m}\nabla^2 + U_{ext}(\mathbf{r}) + g_{3D}|\psi(\mathbf{r})|^2\right]\Psi(\mathbf{r}) = \mu\Psi(\mathbf{r}), \tag{2.19}$$

where U_{ext} is the external confining potential, and μ is now the global chemical potential.

The Bogoliubov approximation is used to find the basic excitations of this system. Here, the wave function is modeled as the sum of the equilibrium wavefunction and a small perturbation ($\Psi = \Psi_0 + \delta\Psi$). Substituting this into equation (2.19) yields the excitation spectrum of a BEC

$$\hbar\omega = \sqrt{\frac{\hbar^2 k^2}{2m}\left(\frac{\hbar^2 k^2}{2m} + 2g_{3D}n\right)}. \tag{2.20}$$

For large momentum k, the spectrum resembles the quadratic spectrum of a free particle, while it is linear for small k. In the latter case (for $T \approx 0$), the sound velocity within the condensate can be written as

$$c_{3D} = \sqrt{\frac{ng_{3D}}{m}}. \tag{2.21}$$

One speaks of a one-dimensional (1D) quantum gas, if the confinement is strongly increased along two spatial dimensions and the temperature as well as the chemical potential fulfill the condition

$$\mu, k_B T \ll \hbar\omega_\perp. \tag{2.22}$$

In this case, the radial motion of the atoms is frozen and only the ground state of the radial potential is populated. A detailed overview the different regimes of 1D gases can be found in [35]. A peculiar difference of a 1D system when compared to a 3D system is that in the 1D case, interactions *increase* with *decreasing* density [43, 34]. Therefore to describe a 1D gas as weakly interacting, the density needs to be sufficiently high. Then the atomic wave functions can, like in the 3D case, be represented by a mean-field approach.

In the regime where the 1D conditions (2.22) are met, the effective 1D interaction parameter was found by Olshanii [34] to be

$$g_{1D} = \frac{2\hbar^2 a}{ml_\perp^2}\left(1 - \mathcal{C}\frac{a}{\sqrt{2}l_\perp}\right)^{-1}, \tag{2.23}$$

with the transverse oscillator length $l_\perp = \sqrt{\hbar/m\omega_\perp}$ and a constant $\mathcal{C} = 1.4603$. For $a \ll$

$l_\perp$, the second term in equation (2.23) becomes negligible and the interaction parameter can be approximated by

$$g_{1D} \approx \frac{2\hbar^2 a}{m l_\perp^2} = 2\hbar\omega_\perp a. \tag{2.24}$$

This expression can also be obtained by averaging the 3D interactions over the radial density profile [97]. The approximation $a \ll l_\perp$ is justified for our experiments with ^{87}Rb, since the scattering length is $a = 5.24$ nm, while the transverse oscillator length is of the order of a μm for realistic transverse trapping frequencies $\omega_\perp$ of a few kHz. Equation (2.24) is central to this work, as it shows that the effective interactions between atoms in a 1D Bose gas can be controlled by changing the transverse confinement.

2.5 Coupled 1D Gross-Pitaevskii equations

The above approach can be extended to a two-component Bose gas. We begin with the two-component coupled Gross-Pitaevskii equations (GPEs) in three dimensions. Following Mertes et al. [85] and Egorov et al. [98] they can be written as

$$\begin{aligned} i\hbar\frac{\partial \Psi_1}{\partial t} &= \left[-\frac{\hbar^2\nabla^2}{2m} + U_1 + g_{11}|\Psi_1|^2 + g_{12}|\Psi_2|^2 - i\Gamma_1\right]\Psi_1 \\ i\hbar\frac{\partial \Psi_2}{\partial t} &= \left[-\frac{\hbar^2\nabla^2}{2m} + U_2 + g_{22}|\Psi_2|^2 + g_{12}|\Psi_1|^2 - i\Gamma_2\right]\Psi_2. \end{aligned} \tag{2.25}$$

where $g_{ij} = 4\pi\hbar^2 a_{ij}/m$ are the 3D coupling constants in terms of the scattering lengths a_{ij} for elastic interactions between atoms in states i and j. The dominant decay rates for our states $|1\rangle$ and $|2\rangle$ in ^{87}Rb $\Gamma_1 = \frac{\hbar}{2}(\gamma_{111}|\Psi_1|^4 + \gamma_{12}|\Psi_2|^2)$ and $\Gamma_2 = \frac{\hbar}{2}(\gamma_{12}|\Psi_1|^2 + \gamma_{22}|\Psi_2|^2)$. The values for the three-body decay constant γ_{111} and the two-body decay constants γ_{12} and γ_{22} are taken from [98].

We reduce this set of equations to the one-dimensional form by substituting the transverse ground state (gaussian) wavefunction and integrating over the radial directions [99]. Assuming direction- and state-dependent transverse trapping potentials $\omega_{i(y,z)}$ we find a coupled set of 1D GPEs for the longitudinal wavefunctions $\psi_i = \psi_i(x)$

$$\begin{aligned} i\hbar\frac{\partial \psi_1}{\partial t} &= \left[-\frac{\hbar^2\nabla^2}{2m} + V_1(x) + u_{11}|\psi_1|^2 + u_{12}|\psi_2|^2 - iK_1\right]\psi_1 \\ i\hbar\frac{\partial \psi_2}{\partial t} &= \left[-\frac{\hbar^2\nabla^2}{2m} + V_2(x) + u_{22}|\psi_2|^2 + u_{12}|\psi_1|^2 - iK_2\right]\psi_2 \end{aligned} \tag{2.26}$$

where $V_i(x)$ is the longitudinal dependence of the external potential and the resulting 1D interaction constants are

$$\begin{aligned} u_{11} &= 2\hbar\sqrt{\omega_{1y}\omega_{1z}}a_{11} \\ u_{22} &= 2\hbar\sqrt{\omega_{2y}\omega_{2z}}a_{22} \\ u_{12} &= 4\hbar\sqrt{\frac{\omega_{1y}\omega_{2y}\omega_{1z}\omega_{2z}}{(\omega_{1y}+\omega_{2y})(\omega_{1z}+\omega_{2z})}}a_{12}. \end{aligned} \tag{2.27}$$

The one-dimensional loss rates $K_1 = \frac{\hbar}{2}(k_{111}|\psi_1|^4 + k_{12}|\psi_2|^2)$ and $K_2 = \frac{\hbar}{2}(k_{12}|\psi_1|^2 + k_{22}|\psi_2|^2)$ involve corresponding coefficients

$$\begin{aligned} k_{111} &= \frac{m^2}{3\pi^2\hbar^2}\omega_{1y}\omega_{1z}\gamma_{111} \\ k_{12} &= \frac{m}{\pi\hbar}\sqrt{\frac{\omega_{1y}\omega_{2y}\omega_{1z}\omega_{2z}}{(\omega_{1y}+\omega_{2y})(\omega_{1z}+\omega_{2z})}}\gamma_{12} \\ k_{22} &= \frac{m}{2\pi\hbar}\sqrt{\omega_{2y}\omega_{2z}}\gamma_{22}. \end{aligned} \tag{2.28}$$

2.6 Tuning scattering properties in 1D

In experiments with ultra-cold gases, Feshbach resonances (see [17] for a comprehensive review) are most commonly used for changing inter-atomic interactions. In the vicinity of a such a resonance, the s-wave scattering length a can typically be tuned over orders of magnitude and also between positive and negative values simply by changing a magnetic field. This makes Feshbach resonances a versatile tool that has been used for example to create a BEC of bosonic molecules from a Fermi gas [100].

Feshbach resonances have been predicted and found for most alkali atoms [101]. However, in ^{87}Rb no practical Feshbach resonances exist in the magnetically trappable states. At high magnetic fields, resonances do exist in the optically trappable $|1,1\rangle$ state [102]. Furthermore, a mixed-spin-channel resonance involving high field seeking states $|1,1\rangle$ and $|2,-1\rangle$ at a magnetic field as low as 9 Gauss has been reported [103].

A key point of this thesis is that state-dependent potentials offer an attractive alternative to Feshbach resonances for achieving tunability of the relevant interaction parameters. The intra- and interstate scattering lengths for states $|1\rangle$ and $|2\rangle$ in ^{87}Rb, as indicated in figure 2.1, are $a_{11} = 100.4 \cdot a_0$, $a_{22} = 95.44 \cdot a_0$ and $a_{12} = 98.006 \cdot a_0$ [98], where a_0 is the Bohr radius. The near-equality of these values is a unique feature of ^{87}Rb. This is highly advantageous for our purposes, since we primarily aim at investigating around the point where all three scattering lengths are equal. The main point here is that the RF-based method described above allows us to tune the interactions over an interesting range.

To elaborate, as explained in section 2.4, in one dimension the collisional interaction strength depends both on the scattering length and the transverse confinement frequency.

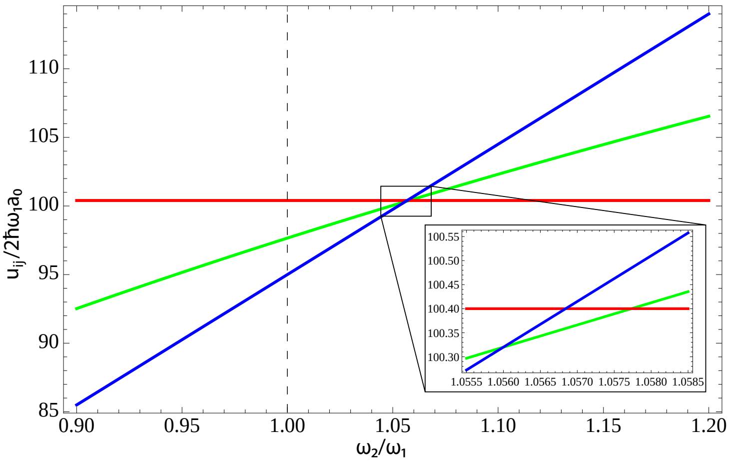

Figure 2.4: 1D interaction parameters for ^{87}Rb and fixed ω_1. The intra- and interstate interaction parameters u_{11},u_{22} and u_{12}, according to equation (2.27), are indicated in red, blue and green, respectively. The inset shows a zoom on the point where the three interaction parameters differ the least. The dashed vertical line indicates the unmodified case.

As the additional RF field modifies the external potential in a state-dependent way, it is therefore possible to precisely tune atomic interactions in this system via the parameters of the RF field. In general, both the modification to the external (longitudinal) potential and the change in interaction strengths need to be taken into account. Figure 2.4 shows the 1D interaction parameters as a function of the ratio of the transverse trapping frequencies of both states for radially symmetric trapping $\omega_{iy} = \omega_{iz} = \omega_i$. At $\omega_2/\omega_1 = 1.057$, these parameters are equal to within 0.09 % (see inset in figure 2.4). This corresponds to a reduction of differences between the interaction parameters by a factor of 30, when compared to the unmodified case. Demonstrating this novel way of tuning the interactions much closer to the point of equality is the main accomplishment reported in this thesis (see chapter 5).

In equations (2.27) and (2.28), the trap frequencies ω_i depend on the dressing parameters δ_i. The modified trap frequencies are

$$\tilde{\omega}_i^2 \quad = \delta_i \omega_i^2, \text{where } \delta_i \quad = \Delta/\sqrt{\Omega_i^2 + \Delta^2}, \tag{2.29}$$

with detuning $\Delta = \omega_L - \omega_{rf}$ and ω_L being the Larmor frequency.

2.7 Spin motion

A very useful way to characterize the properties of the two coupled GP equations, and to analyze their stability, is to study small perturbations around a steady state. Using this approach, one finds two dispersion relations, for two different excitation modes. For long wavelengths, the dispersion relations are linear, and the corresponding propagation velocities are given by [104]

$$c_\pm^2 = \frac{(c_1^2 + c_2^2) \pm \sqrt{(c_1^2 - c_2^2)^2 + 4\alpha_{12} c_1^2 c_2^2}}{2}, \tag{2.30}$$

with $\alpha_{12} = u_{12}^2/(u_{11}u_{22})$, the sound velocities $c_j = \sqrt{n_j u_{jj}/m}$ (see equation (2.21)) and $j = 1, 2$.

Close to the point of equal interactions ($u_{11} \approx u_{12} \approx u_{22}$), the excitations take on the character of (i) variations in the total density, with velocity c_+, and (ii) variations in the difference in density $n_1 - n_2$, with velocity c_-. The density difference can be regarded as a spin polarization, hence we refer to the latter velocity as the spin velocity.

We are particularly interested in the parameter region around $\alpha_{12} \approx 1$. In this region, equation (2.30) can be rewritten as

$$c_\pm^2 = \left(\frac{c_1^2 + c_2^2}{2}\right)\left(1 \pm \sqrt{1 + 4\alpha(\alpha_{12} - 1)}\right), \tag{2.31}$$

with the shorthand $\alpha = (c_1^2 c_2^2)/(c_1^2 + c_2^2)^2$. Note that $0 \leq \alpha \leq 1$. For instance, equation (2.31) shows directly that $c_-^2 = 0$ and $c_+^2 = c_1^2 + c_2^2$ for $\alpha_{12} = 1$. More generally, for $\alpha_{12} \approx 1$ or more precisely for $|\alpha_{12} - 1|\alpha \ll 1$, we can expand the root in equation (2.31) to yield the lowest-order expressions in $\alpha(\alpha_{12} - 1)$

$$\begin{aligned} c_+^2 &\approx c_1^2 + c_2^2 \\ c_-^2 &\approx (c_1^2 + c_2^2)\alpha(1 - \alpha_{12}) \approx c_+^2 \alpha(1 - \alpha_{12}). \end{aligned} \tag{2.32}$$

If $\alpha_{12} > 1$, corresponding to $u_{12}^2 > u_{11}u_{22}$, the inter-species repulsion is sufficiently strong for the mixture to be unstable, and c_-^2 is negative. For $0 < \alpha_{12} < 1$ the mixture is stable. Figure 2.5 shows the “phase diagram” for the scaled effective interaction.

In this diagram, another aspect is highlighted beyond that of the miscibility discussed above, namely that of buoyancy. In an external potential, such as the magnetic trap in our experiments, this is an important aspect that needs consideration. Buoyancy is the lowering of the total energy by the denser component sitting at the bottom of the potential. It is what makes ice float on water. For our 1D system of two-component bosons, this implies that even if the two components are miscible in terms of their interactions, the component with the smallest intra-species scattering length will predominate in the center of the trap. Because of the smaller scattering length, this component tends to have a higher density in equilibrium. To minimize the total energy the other (less dense) component will then be pushed towards the edges of the trap.

To illustrate this, we show the numerically calculated [105] ground state of the two-component Gross-Pitaevskii equations (2.26) in figure 2.6. For this figure, typical parameters were used, namely rubidium atom numbers $N_1 = N_2 = 1800$ in a trap with transverse trapping frequencies $\omega_{x,y}/2\pi = 1.9\,\text{kHz}$ and axial trapping frequency $\omega_x = 26\,\text{Hz}$. For this

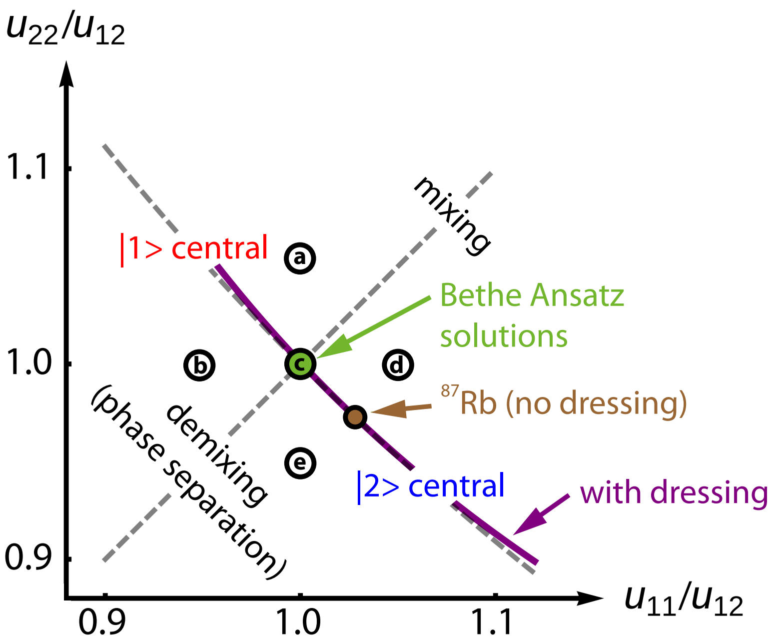

Figure 2.5: Diagram indicating different regimes of the two-component 1D Bose gas. The effective intrastate interactions u_{11} and u_{22} are scaled to the interstate interaction u_{12}. Exact solutions based on a Bethe Ansatz exist only for the point of equal interactions ($u_{12} = u_{11} = u_{22}$). The purple curve indicates the accessible experimental range without Rf-dressing. Each of the ratios marked a,b,c,d,e corresponds to the accordingly named subfigure in figure 2.6, showing the respective calculated ground state densities.

illustration, the trapping was kept state-independent, the inter-species scattering length was set to $a_{12} = 100a_0$ and the intra-species scattering lengths were varied to sample representative points in the $(u_{22}/u_{12}, u_{11}/u_{12})$ parameter space (see labeled points in diagram 2.5).

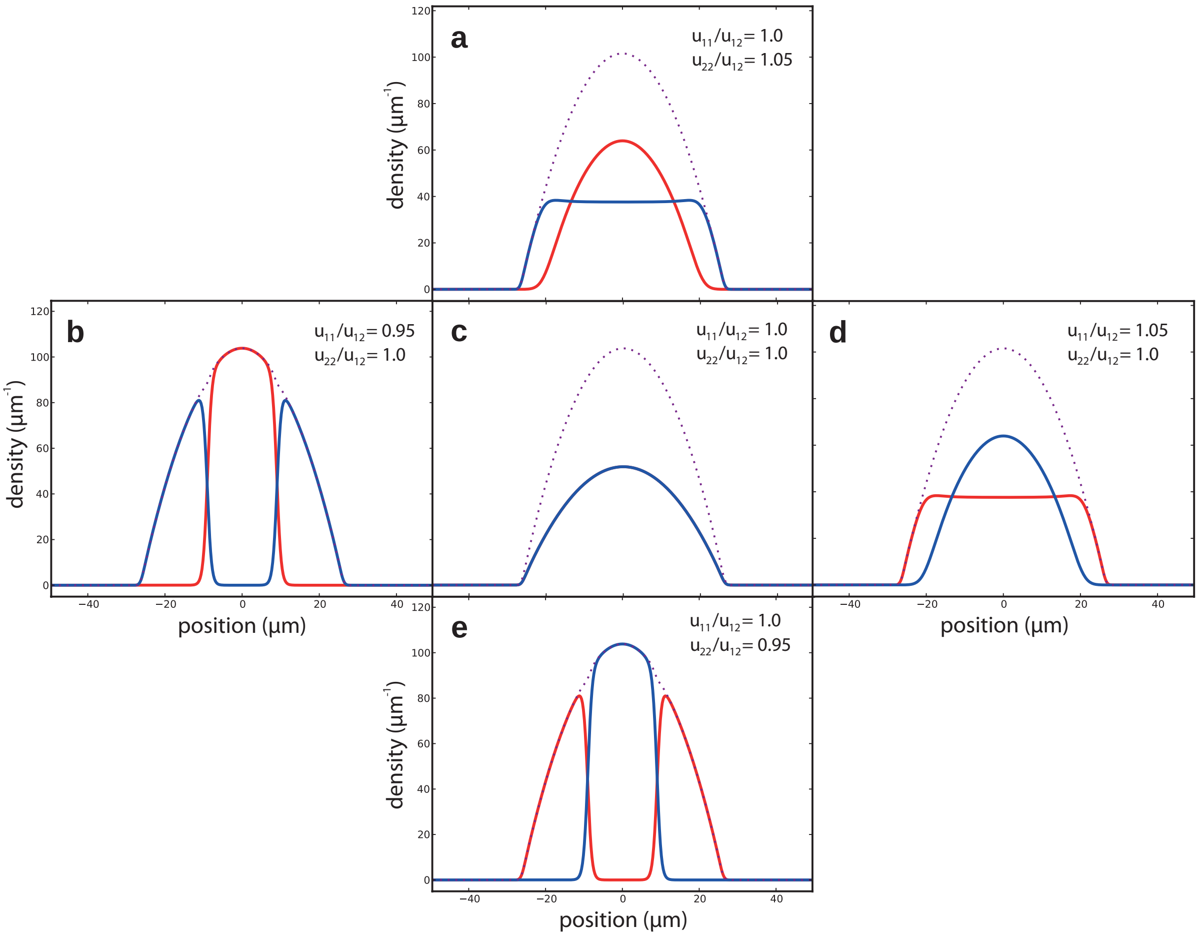

Figure 2.6: Ground state densities of the two-component 1D GPE. Densities of states $|1\rangle$ and $|2\rangle$ are indicated in red and blue, respectively. The total density is depicted by dashed purple lines. Subfigures (a,c,b,d,e) correspond to different ratios of the effective intra-species interactions, labeled accordingly in figure 2.5.

Chapter 3

Experimental setup & methods

3.1 The CELSIUS experiment

This chapter describes the scientific apparatus and the methods used to perform experiments with two-component 1D quantum gases of ^{87}Rb. There are several approaches to making one-dimensional gases. Crossed optical lattices were used to create arrays of equidistant elongated potentials, leading to a multitude of 1D gases. This was used in some of the ground-breaking experiments in the groups of D. S. Weiss [38], I. Bloch [39] and W. D. Phillips [106]. The crossover from the 3D to the 1D regime has been studied in early work with atom chips [107, 108, 109] and atom chips were proposed to create Tonks-Girardeau gases [110]. Coherence lifetimes of internal states in excess of 1 sec have been shown to be independent of the atom-surface distance, which makes this technique interesting for atomic clock applications [111]. In late 2002 our group started designing an atom chip-based experiment, mainly with the aim of reaching the strongly interacting regime but also to access phase and density fluctuations of individual realizations of a 1D gas. This is in contrast to experiments based on optical lattices, where averaging over many lattice sites is hard to avoid [112]. In 2006, our group succeeded in reaching the Bose-Einstein phase transition and also entered the 1D regime.

A detailed description of the pre-existing setup can be found in [90, 113]. Here, we sketch the basics of the experimental apparatus to have a self-contained description. In the next sections, we focus on the changes and additions made in the course of this PhD work, and in particular on the features required to study the two-component 1D Bose gas. The outline is as follows. First, a summary is given of the basic features of the vacuum system, the laser system, the atom chip and the RF-generation, mentioning also the relevant changes made since the previous PhD thesis [113]. Subsequently, the main additions we made to the CELSIUS (Chip Experiment for Low-dimensional, Strongly Interacting Ultracold Systems) experiment, namely the subsystem for microwave generation (section 3.2), a secondary imaging system for imaging along the 1D-axis (section 3.3) and a super-imposed optical lattice along the 1D-axis (section 3.4) are described and characterized in some detail.

3.1.1 Vacuum system

The vacuum system to generate ultra-high vacuum (UHV) conditions for experiments with ultra-cold gases is built around the science chamber (see figure 3.1). This science chamber is custom-made from stainless steel and has an octagonal cross-section. It holds six anti-reflection (AR) coated CF40 viewports and one uncoated CF100 viewport which provide optical access for MOT-, pump- and probe-light. Two additional CF16 viewports are used for monitoring the loading of the MOT by means of small infrared sensitive cameras. The atom chip including its electrical feedthroughs and water cooling is inserted into the top port of the science chamber via a 4 + 1-way cross-piece. The bottom port connects the pump section, consisting of an demountable turbo-molecular pump, an ion getter pump and a titanium-sublimation pump. For maintenance purposes, the pump section can be separated from the science chamber with a gate valve. After pump down and a bake out at 180° C an ionization gauge indicates a residual pressure of $\approx 10^{-11}$ mbar.

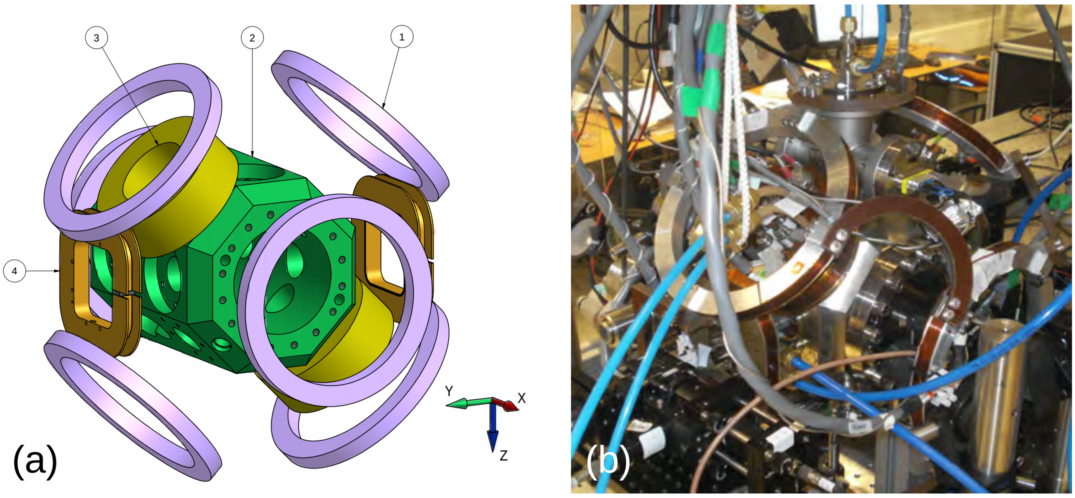

Figure 3.1: Main vacuum chamber (“science chamber”) surrounded by magnetic field coils. (a) Schematic (adapted from [90]). (1) Compensation coils, (2) Science chamber, (3) MOT coils, (4) Y-Bias coils, providing a homogeneous field along the Y-direction for tight waveguide potentials. (b) Photo of the vacuum chamber surrounded by coils, optics, electrical connections and water cooling (blue tubes). The atom chip mount is visible on top of the chamber.

The science chamber is surrounded by three sets of coils (indicated in figure 3.1(a)), which provide the magnetic fields for magneto-optical trapping, the compensation of fields in arbitrary direction and the tight confinement needed for the generation of 1D gases. All coils are powered by programmable analog current supplies (Kepco / BOP 20-10M, BOP 20-20M, BOP 36-12M and BOP 20-5M) and switched (except for the four compensation coils at 45° angles) using home-built MOSFET switches to enable rapid switching.

We also connected the Rubidium dispenser to such a switch to allow digital switch off as an additional safety measure. Two of these dispensers are mounted inside the vacuum chamber slightly below the atom chip. One of them emits away from the atom chip, the other one towards it. We started operating with the dispenser emitting towards the chip in April 2008, after the previously used dispenser showed signs of depletion.

3.1.2 Laser system

Two commercial semiconductor diode lasers in an external cavity setup (Toptica DL100) provide light with a wavelength of 780 nm. One of these lasers serves as the master laser for cooling, pumping and imaging atoms (for a detailed description see [90]). The other laser is used for re-pumping atoms that have fallen into a dark state out of the cooling cycle (see [113]). Both lasers are frequency-locked to atomic transitions in ^{87}Rb with a frequency modulation technique [114]. Acousto-optical modulators (AOMs) are used to shift the frequency of the light for different applications. Mechanical shutters and electro-optical modulators (EOMs) switch laser light on and off before it is coupled into polarization-maintaining single mode optical fibers guiding it to the optical components surrounding the science chamber.

The original optical setup was extended by a second imaging system (see section 3.3), enabling simultaneous imaging along the x- and y-axes. Furthermore, we added an optical lattice along the x-axis, which is described in Sec.3.4. Due to limited optical access, only one of these two additions to the experiment can be used at a time. The optical lattice caused a need for more laser power. Therefore the injection locked high-power laser described in [90] was replaced by a tapered amplifier. The amplifier is mounted in a custom-made housing [115] and yields an output power of 290 mW at current of 0.9 A and 25 mW seeding power.

3.1.3 Atom chip

At the heart of our experiment is the atom chip. The atom chip is a micro-fabricated gold wire pattern (see figure 3.2) on a silicon substrate. In combination with two layers of three macroscopic wires each under the atom chip itself and the external field coils, the on-chip wires serve to generate the extremely steep and elongated potentials necessary for experiments with 1D gases. The characteristics and functions of the individual chip wires numbered 1-8 are listed in table 3.1. The chip is mounted upside-down on a water-cooled copper block at the center of science chamber. Apart from dissipating the heat caused by ohmic heating of the wires, the mount provides electrical vacuum feedthroughs which serve to connect the chip wires to their current sources.

For the experiments presented in this thesis, the following chip wires were used: Wire 5 for trapping, wires 3 and 6 for radio-frequency dressing and wire 4 for RF-induced evaporative cooling. Before the measurements presented in chapter 5, an electrical short between wire 7 and 8 occurred due to an accident involving too much current because of a mistaken connection. This is evident by a resistance measurement between all chip wires, displayed in table 3.2.

3.1.4 Radio-frequency generation

The various radio-frequency (RF) fields for evaporative cooling, coherent transfer between different Zeeman states and dressing atoms in our experiment originate form four direct digital synthesis (DDS) evaluation boards (Analog Devices / AD9854). The boards are housed in a custom-made rack, which provides them with power, interfacing to the control computer and a reference frequency. The RF generation is treated in great detail in [113]. The 10 MHz reference frequency is derived from a frequency standard (see 3.2) and routed

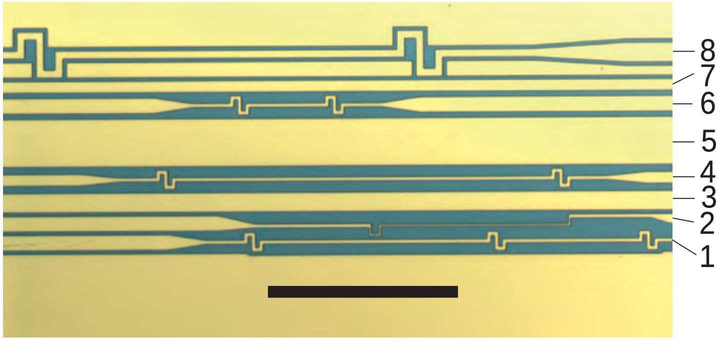

Figure 3.2: Atom chip wire pattern. The characteristics of the individual wires are given in table 3.1. The length of the black scale bar is 500 μm. The wires are defined by 5 μm wide trenches in the 1.8 μm thick gold layer.

wire	w (μm)	R (Ω)	function
1	10	3.15	double box structure
2	5	3.70	wiggle test wire
3	50	1.47	Z wire, radio-frequency field
4	10	3.89	1.00 mm box
5	125	0.72	Z wire, initial trapping
6	10	2.42	0.20 mm box, RF evaporation
7	30	2.06	Z wire, radio-frequency field
8	20	2.30	0.90 mm box

Table 3.1: Characteristics of the wires on the atom chip. Widths w and resistances R of the wires are listed along with their functions for experiments (see [113]).

	1	2	3	4	5	6	7
2	16.4						
3	31.0	19.2					
4	35.0	26.0	21.0				
5	34.6	26.1	25.1	5.7			
6	42.0	33.4	23.9	12.5	6.6		
7	46.3	37.6	33.1	16.3	11.6	7.2	
8	46.3	37.6	33.0	16.3	11.6	7.2	0.004

Table 3.2: Cross-resistance between the chip wires in kΩ measured after completion of the experiments presented in this thesis. The low resistance between wires 7 and 8 indicates an electrical short.

to all four evaluation boards. We found that this common reference is sufficient to keep the output of the evaluation boards in phase lock. The output of DDS board 1 is directly connected to chip wire 4 (see figure 3.2) for evaporative cooling. The outputs of boards 2 and 3 are amplified by 28.5 dB before they are connected to chip wires 3 and 6, respectively.

3.2 Microwave generation

We use a two-photon transition to create coherent mixtures of internal states of ^{87}Rb. The hyperfine splitting of the electronic ground state in ^{87}Rb corresponds to a frequency of $\omega_{hf} = E_{hf}/\hbar = 2\pi \cdot 6.834682\,\text{GHz}$ (see figure 2.1). Furthermore, driving the transition from $|F = 1, m_f = -1\rangle$ to $|F = 2, m_f = 1\rangle$ requires $\Delta m_f = 2$, therefore a two-photon transition is needed. In practice, this can be conveniently achieved by combining a microwave (MW) signal of $\omega_{hf} \approx 2\pi \cdot 6.834682\,\text{GHz}$ with a RF signal of a few MHz [84]. To provide the MW signal with a sufficient amplitude at the position of the trapped atoms and computer-controlled tunability of the frequency, we enhanced the experiment by a microwave subsystem which is shown schematically in figure 3.3 and described below.

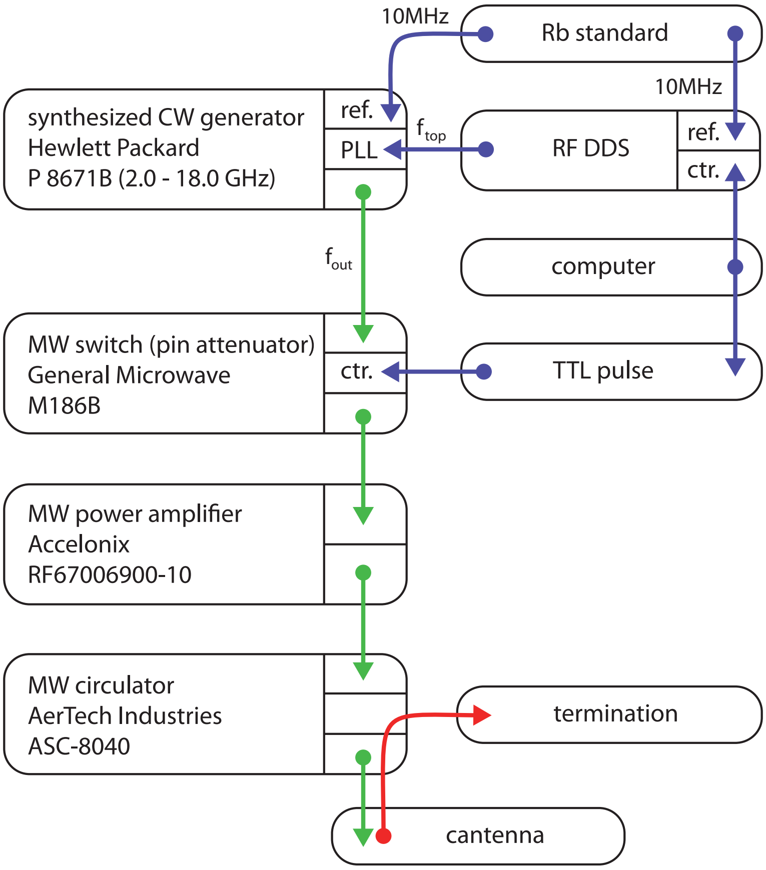

Figure 3.3: Schematic of the microwave subsystem. Blue arrows indicate control signals and reference frequencies, the red arrow indicates the part of the MW signal reflected by the antenna and green arrows denote the actual MW signal with frequency f_{out}.

A rubidium standard (Symmetricom/Model 8040), based on an atomic clock, provides our lab and the neighboring permanent-magnetic atom-chip experiment [116] with a highly stable (Allan deviation averaged over 1 sec less than $3 \cdot 10^{-11}$) 10 MHz signal. This is used as a reference for both the RF generation by means of direct digital synthesis (DDS) (see section 3.1.4) and a continuous-wave MW synthesizer. The MW synthesizer output frequency f_{out} can be tuned by an external RF signal with frequency $f_{top} \approx 20\,\mathrm{MHz}$ derived from the DDS generator. To achieve this, the RF signal is fed into one of the four phase locked loops (PLL) controlling the synthesizer output frequency [117]. The output frequency then is related to the input frequency by

$$f_{out} = 6830\,\mathrm{MHz} + (2 \cdot (30\,\mathrm{MHz} - f_{top}) - 10\,\mathrm{MHz}). \tag{3.1}$$

The synthesizer's output signal with a power of $-7.5\,\mathrm{dBm}$ then enters a pin modulator which is used to rapidly switch on and off the MW signal. The modulator is switched by a TTL pulse originating from the experiment control computer. In this way, the frequency (via f_{top}) and the on/off status of the MW pulse are set by the computer, while the amplitude is fixed.

Due to the re-programming of the DDS boards at the beginning of each experimental cycle, f_{top} cannot be set at all times. Since the synthesizer needs a time of $\approx 5\,\mathrm{ms}$ to lock onto a frequency, a low amplitude fixed 20 MHz signal originating from a frequency generator (not shown in figure 3.3) is mixed with the higher amplitude f_{top} signal. In this way, the synthesizer is kept from unlocking.

The resulting MW pulse is amplified by a solid state MW amplifier. Finally, the output of the amplifier is connected via a circulator to a tube-shaped antenna, popularly known as cantenna (see below). The circulator's reverse port is terminated with a $50\,\Omega$ dummy load. This deflects back reflections off the cantenna due to impedance mismatches and prevents damage to the amplifier by the reflected signal. The cantenna is placed directly outside the CF100 window of the vacuum chamber (see figure 3.4(b)), aiming at the region below the atom chip. On the opposite side of the science chamber, a pickup pin antenna of length $\lambda_{out}/4 \approx 11\,\mathrm{mm}$ is installed to monitor the timing and the amplitude of the MW pulses. The orientation of the pin antenna is perpendicular to the plane of the atom chip.

Cantenna design

Since no appropriate directional antenna for 6.8 GHz was readily available, we decided to adapt a design widely used for WiFi-communication ($\approx$ 2.4 GHz). It is based on a metallic tube with an open and a closed end. Therefore this design is often referred to as cantenna. The signal carrying cable is connected to a metal pin antenna inside a conducting cylinder (see figure 3.4(a)).

According to [118], four parameters are crucial for good operation of the cantenna. First, and most important is the diameter of tube. The mode with the lowest cut-off frequency is the so-called H_{11} mode, in which the electric field lines are mainly perpendicular to the tube cross section with a concentration in the center. The cut-off frequency for this mode

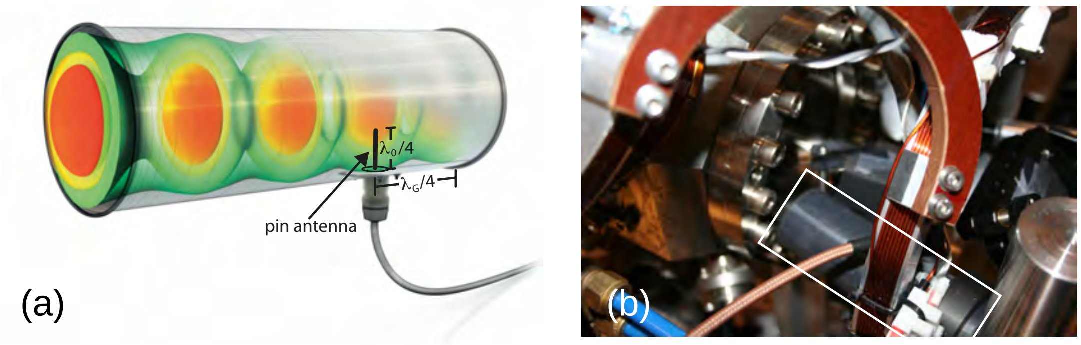

Figure 3.4: (a) Schematic of the cantenna (adapted from [118]). The coax cable ends in a metal pin antenna of length $\lambda_0/4$ and distance $\lambda_G/4$ from the back plane of a metal cylinder. While the cylinder's back side is closed to reflect the incoupled mode, the front is open to emit it. The colors give an impression of the mode profile inside the cylinder. (b) Photo of the cantenna in the experiment. The position of the cantenna is indicated by a white rectangle. The cylinder is covered with black paper to avoid laser reflections.

is $f_c = c/(1.71 \cdot d)$, where c is the speed of light and d is the inner diameter of the tube. We chose a brass tube with $d = 32\,\mathrm{mm}$ such that only the H_{11} mode is excited. The cut-off frequency for the next mode is at 7.15 GHz for our choice of the diameter. Second, the length of the pin should be $\lambda_0/4 = 11$ mm, where λ_0 is the wavelength of the radiation to be transmitted in free space. Third, the distance of the pin from the back plane should be chosen such that the back-reflected wave interferes constructively with the direct wave. This is the case when the distance is equal to $\lambda_G/4 = 18.4$ mm with $\lambda_G = c/\sqrt{f_{out}^2 - f_c^2}$ the wavelength of the mode excited inside the tube. Finally, the overall length of the tube should be such that reflections from the transition from the tube to free space are suppressed. According to [118] the optimal length to achieve this is $5/8\lambda_G + n\lambda_G/2$ with $n = 0, 1, 2, \ldots$. Out of space considerations, we chose for $n = 1$ and therefore the total tube length is 64.3 mm. For tunability of the distance between pin and back plane, the back plane was made of a massive copper cylinder, which tightly fits into the tube, but can still be moved in and out.

3.3 Dual imaging

In addition to the experiments performed with two-component Bose gases, described in chapters 5 and 4, we used radio-frequency dressed potentials to create double-well potentials. These result in two elongated clouds separated by a couple of microns. By changing the relative amplitude or phase of the two RF signals making up the double-well potential, the angle between the two ensembles in the y-z-plane can be tuned to arbitrary values between 0 and 2π. Only in the case where the clouds are separated along the z-axis (vertically) can they be imaged separately and can their in-trap distance be determined. We release the atoms from the double-well potential to investigate the coherence between the split clouds. After some time of flight, they overlap due to expansion and we record the interference patterns.

In a typical experimental setup, elongated ultra-cold gases are probed with light perpendicular to their long axis (according to our definition the x-axis). In this manner, the physics governing the atomic density and motion along the x-axis can be studied. To study the atom clouds along the x-and the y-axis and to fully characterize RF potentials, we added a second imaging system, which is used to take absorption images along the x-axis.

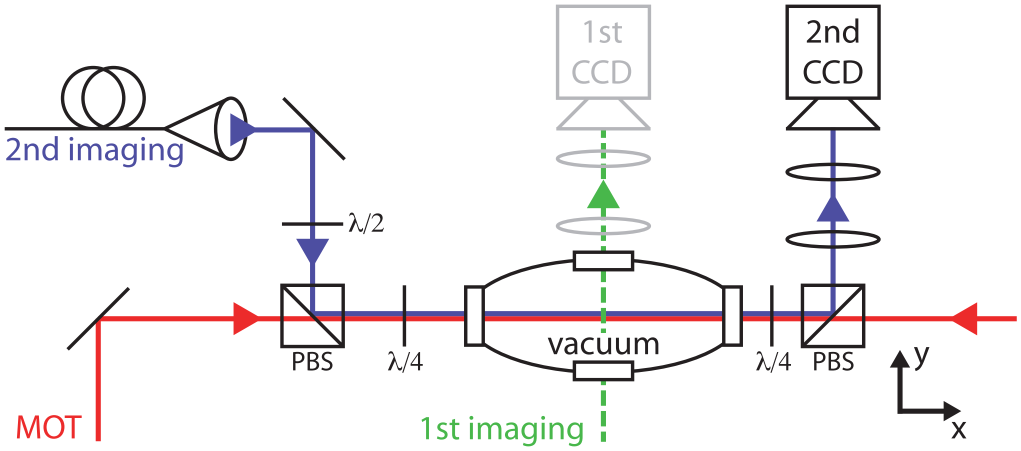

Figure 3.5: Schematic of the dual imaging setup. The laser beams used for the first and the second imaging setup are indicated by dashed green and full blue lines, respectively. The laser beam for magneto-optical trapping are colored red.

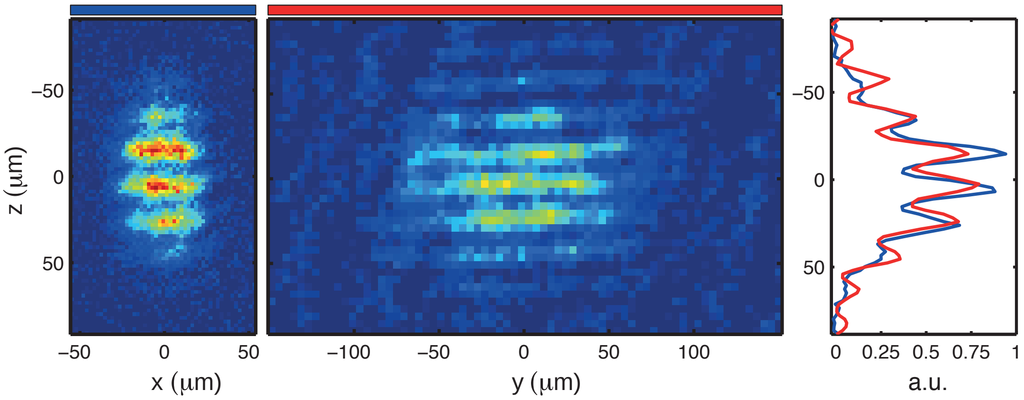

Figure 3.6: Absorption images of interfering atoms. The images were taken simultaneously with the first (indicated by the blue bar) and second (red bar) imaging system. The right figure shows the integrated optical density in arbitrary units for imaging along the y-axis and the x-axis in blue and in red, respectively.

Figure 3.5 schematically depicts the changes made to the optical setup to enable dual imaging. To gain optical access to the x-axis, which is otherwise occupied by two counter-propagating MOT laser beams, we inserted two polarizing beam cube splitters (PBS) to overlap the imaging laser with the MOT beams. Due to the geometry of the chamber and the fact that the first imaging lens of the second imaging system has to be placed behind the beam splitter, the distance atoms-lens, which mainly determines the characteristics of the imaging system, is 20 cm, as compared to 10 cm for the first imaging system. This difference translates to a measured effective pixel size in the object plane of $p_x = 4.07\,\mu\mathrm{m/pixel}$, whereas it is $p_y = 2.15\,\mu\mathrm{m/pixel}$ for the first imaging system. We chose an achromat with $f_1 = 200\,\mathrm{mm}$ focal length as first lens, followed by a second lens with $f_2 = 350\,\mathrm{mm}$ focal. This results in a theoretical magnification of 1.75, compared to a magnification of ≈ 3 for the imaging along the y-axis. The CCD camera used for the second imaging system, is a newer version (Roper Scientific / Coolsnap EZ) of the camera in the first imaging system (Roper Scientific / Coolsnap ES). A TTL signal originating from the experiment control computer triggers the camera and a LabView program, which is processing incoming images. This program runs on an independent computer, which is identical to the experiment control computer.

An example of simultaneously taken images is given in figure 3.6. For this, the atoms have been prepared in an elongated trap and coherently split in the vertical/y-direction by means of radio-frequency dressed potentials. After being released from the double-well potential, the two coherent ensembles expand and overlap. Absorption images, taken after 14 ms time-of-flight, clearly feature horizontal interference patterns.

While the probe light is linearly polarized in the first imaging setup, due to the $\lambda/4$-phase plates needed for the MOT beams it is circularly polarized in the second imaging system. This causes detection efficiency differences. These differences can not be explained by the differing cross-sections alone. Also optical pumping plays a role and is different depending on polarization and the axes. To characterize the system, we probed all combinations of imaging directions and quantization field directions for sequential and simultaneous imaging. The resulting calibration factors are shown in table 3.3. The higher numbers in the case of simultaneous imaging correspond to reduced absorption due to cross-talk.

		sequential imaging		simultaneous imaging	
		quantization axis			
		y	x	y	x
imaging	y	1.00	2.77	1.39	2.88
axis	x	2.42	1.26	2.94	1.64

Table 3.3: Observed calibration factors from absorption to relative atom numbers. The factors were measured for either sequential or simultaneous horizontal (along the y-axis) and longitudinal (along the x-axis) imaging with a quantization field aligned along the x- or y-axis. The table is scaled to the case of the upper left corner.

3.4 1D optical lattice

A periodic potential along the elongated direction of atoms confined to one dimension opens new possibilities for their manipulation. A deep lattice will result in a string of small ensembles or even single atoms. Such a system is well-suited to freeze and subsequently study fluctuations of one-dimensional ensembles. If on the opposite, a shallow lattice is superimposed, this can change the interatomic interactions to the point where the strongly interacting regime is entered [39, 65]. To get access to these promising features, we implemented an optical lattice into the CELSIUS setup. This is the focus of ongoing experiments. Since this work is covered in detail in a master thesis [119], I will only provide a brief description of the changes made to the setup and first results obtained with the optical lattice.

Two counter-propagating laser beams form a standing wave. To avoid scattering light off the atoms, the light frequency is chosen such that it is detuned from the optical transition of the atoms by Δ. Atoms in the standing wave experience a spatially periodic Stark shift. For blue-detuned light ($\Delta > 0$) they are repelled by the maxima of the standing wave, for red-detuned light ($\Delta < 0$) they are attracted.

If the periodic potential is switched on for a time shorter than an oscillation period of an atom in the optical potential, the atoms do not equilibrate, i.e. they do not gather in potential minima or maxima. In this case the standing wave acts as an optical diffraction grating and we observe diffraction of atoms from a "light crystal". In momentum space, the process can also be regarded as simulated Raman diffraction between two momentum states. An atom absorbs a photon from one laser mode and is stimulated to emit a photon into the counter-propagating mode. In this way the atom changes its momentum in units of $2\hbar k$, where k is the wave number of the light.

For the generation of the laser light for the optical lattice, a home-built external-cavity diode laser (ECDL) is amplified by a tampered amplifier [115]. The light is split equally by a non-polarizing beam cube splitter and coupled into polarization-maintaining single mode fibers, guiding it to the optical setup around the science chamber. Acousto-optical modulators are inserted before the fiber couplers for rapid switching of the light. Doppler-free saturation spectroscopy provides a signal to lock the laser on a spectral feature of ^{87}Rb.

Figure 3.7 shows the setup around the science chamber adapted for the optical lattice. The x-axis is already occupied by MOT lasers and the optical lattice beams have to be linearly polarized. This is why we replaced the previously used (see figure 3.5) polarizing beam cube splitters (PBS) by non-PBS and moved the quarter wave plates in the MOT beams to positions before the cubes. In this way, half of the power of the MOT lasers and the lattice lasers is lost to the "wrong" port of the NPBS. This is compensated by more laser power which made necessary the insertion of tapered amplifier in the MOT- and the lattice laser system.

To prevent heating of the atoms due to a shaking optical lattice, the right lattice beam in figure 3.7 can be phase-locked to the left beam. Therefore the two beams are overlapped to interfere on a fast photodiode (PD). The photodiode signal is connected to a PID controller and fed back to a piezo crystal with a mirror mounted on it. In this manner, the optical path length and therefore the phase of the right lattice beam is adjusted the left beam and a stable standing wave is formed.

In a first proof-of-principle experiment we flashed the 3 mm wide, unfocussed lattice beams on a small falling Bose-Einstein condensate for 6 μs after 3 ms time-of-flight (TOF). The resulting absorption image, recorded after a total of 14 ms TOF, is displayed in figure 3.8.

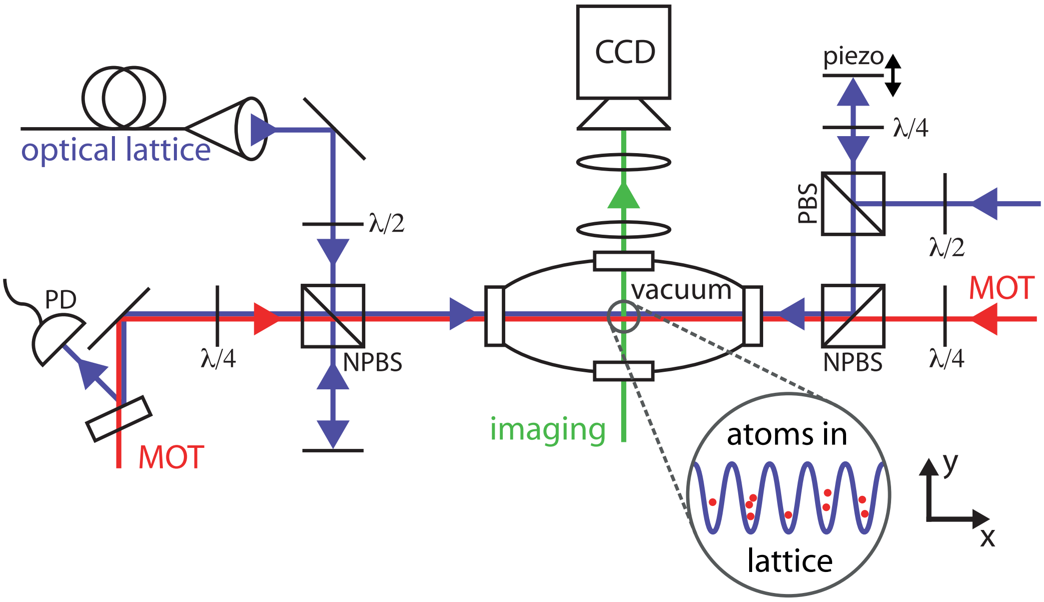

Figure 3.7: Schematic of the optics used to generate an optical lattice. The lasers for the optical lattice are drawn in blue. They counter-propagate in the vacuum chamber, forming the lattice and interfere on the photodiode. The piezo crystal controls the optical path length of the right lattice beam. The laser beams used for imaging and magneto-optical trapping are indicated by green and red lines, respectively.

It clearly shows the first diffraction orders to the left and the right of the central zero momentum cloud.

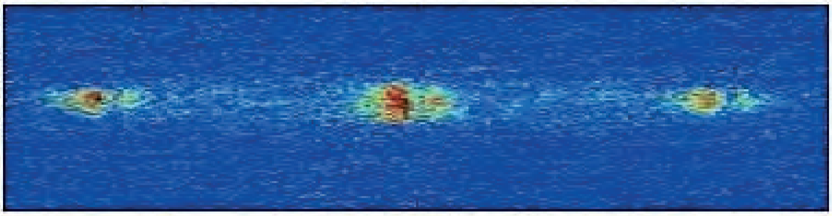

Figure 3.8: Absorption image of diffracted Bose-Einstein condensate. The three clouds correspond to $p_x = -2\hbar k, 0, 2\hbar k$.

Chapter 4

Thermodynamics of a one-dimensional two-component Bose gas

4.1 Introduction

Ultracold gases trapped on atom chips offer unique opportunities to study fundamental problems in quantum (many-body) physics, as may have already become evident from the previous chapters. The one-dimensional (1D), single-component Bose gas with repulsive interactions has emerged as a paradigm system because exact solutions are available from the Lieb-Liniger model [43] for the ground- and excited quantum many-body states for *any* interaction strength. Furthermore, the thermodynamics can also be exactly calculated from the Yang-Yang equations [44] for this system.

As was already alluded to in chapter 2, it is interesting to extend the experimental studies to the multicomponent case. Here, we are interested in the case of the two-component Bose gas. As mentioned, this system has three natural interaction parameters (scattering lengths), and exact eigenstates can be calculated via the Bethe Ansatz if (and only if) these three parameters are all equal. For this specific case also results from the Thermodynamic Bethe Ansatz (TBA) have recently been obtained [47]. It was found that the polarization (the difference in population of the two states) shows some remarkable features, in particular in the polarization at low (but finite) temperatures. Motivated by these predictions, we have investigated the opportunities for experiments with a two-component gas of ^{87}Rb trapped on an atom chip.

We start from a single-component gas at relatively *high* temperature (in the non-degenerate regime), create a two-component cloud with a transfer pulse, and then proceed with evaporative cooling. The aim is to achieve a one-dimensional two-component gas at thermal equilibrium and finite temperature, and compare to predictions such as those of ref. [47]. Although conceptually very similar to the experiments of chapter 5, it turns out that there are a number of challenges to overcome, and we will describe these below.

The outline of this chapter is as follows. In section 4.2 we describe the experimental procedure that was used. We discuss some of the difficulties that were encountered, such as the (re)population of undesired additional states, and how these were circumvented and/or mitigated. In section 4.3 we present the key experimental results, consisting of density profiles of the trapped two-component Bose gas near thermal equilibrium. Section 4.4 discusses the results and to what extent these can be compared to existing theories. Finally, we also present an outlook on desirable future experiments.

4.2 Experimental procedure

The experimental sequence from initial cooling and trapping of atoms to evaporative cooling and finally reaching degeneracy has been described in detail in [90]. We will begin this section with a summary of this sequence. This will be followed by a description of the experimental procedure used to produce a two-component one-dimensional Bose gas.

We begin by pulsing a ^{87}Rb-dispenser first at 20 A for 350 ms and then at 11 A for 850 ms. This releases rubidium atoms into the vacuum chamber. This is followed by switching on two pairs of counter-propagating, red-detuned (with respect to the cycling transition of the D2 line) laser beams. Together with a magnetic field gradient of 15 G/cm generated by the MOT coils, the lasers create a magneto-optical trap (MOT) below the atom chip surface. One pair of laser beams is reflected off the gold-coated chip surface at an angle of 45°, resulting in a mirror-MOT configuration [120]. All laser beams are overlapped with repumping laser beams, which serve to optically pump atoms from a dark state back into the cooling cycle. After a short compressed MOT phase, the atoms are optically pumped into the $|F=2, m_f=2\rangle$ state. At this point, all lasers as well as the MOT coils are switched off and the cloud is trapped magnetically using the mini-wires underneath the atom chip. After a transfer from this wire trap to the chip trap, generated by atom chip wire 5, the trap is drastically compressed, increasing the inter-atomic collision rate. This a perfect starting point for forced evaporative cooling, which we perform by applying a RF-ramp to chip wire 4. At this point, cooling to degeneracy with an RF ramp down to ≈ 2.27 MHz leads to an almost pure condensate of 4.5×10^4 atoms. The overall experimental cycle time is 10 s.

For the experiments described in this chapter, we interrupt the evaporative cooling at 2.4 MHz when the gas can still be considered non-degenerate. The atom are confined in a trap with trap frequencies $\omega_\perp/2\pi = 1.9$ kHz and $\omega_\parallel/2\pi = 26$ Hz. We then create a mixture of atoms in two clock states of ^{87}Rb, $|1\rangle = |F=1, m_f=-1\rangle$ and $|2\rangle = |F=2, m_f=1\rangle$, and finally continue evaporative cooling, reaching degeneracy.

In order to create the mixture of states $|1\rangle$ and $|2\rangle$ we use the following sequence. As a first step after the initial evaporative cooling, we apply a short ($8\,\mu$s) RF pulse, resonant with the level splitting between m_F-states, thereby transferring half of the atoms from $|F=2, m_f=2\rangle$ to $|2\rangle$. Next, a coherent superposition of states $|1\rangle$ and $|2\rangle$ is prepared using a resonant two-photon RF and microwave (MW) coupling [84, 111] as shown in figure 2.1. The microwave frequency is introduced via an external antenna (see section 3.2) while the RF-field is applied directly to the atom chip wires.

To increase the collision rate and thereby also the efficiency of evaporative cooling, the magnetic potential is tightened prior to the final cooling stage. Since state $|2\rangle$ decays faster than state $|1\rangle$ we chose to start evaporation after making an uneven mixture of the two states with an excess of atoms in state $|2\rangle$. This compensates for higher collisional losses experienced by state $|2\rangle$ during evaporative cooling and ensures an even mixture afterwards. For the same reason, the overall time of the final evaporation stage needed to be as short as 350 ms.

Initially, we employed a radio-frequency sweep alongside a constant microwave pulse to expel the unwanted remaining population of $|F = 2, m_F = 2\rangle$ atoms from the trap. This two-photon scheme led to enhanced losses of both states $|1\rangle$ and $|2\rangle$ at the evaporation frequency 2.3 MHz, possibly due to an unintentional cross-resonance between radiofrequency- and the microwave sweeps. It was therefore replaced by a microwave sweep from 7.6 GHz to 6.75 GHz directly coupling the $|F = 2, m_F = 2\rangle$ to the untrapped $|F = 1, m_F = 1\rangle$ state. Furthermore, we found that the purity of the system benefits from an additional 15 ms microwave sweep from 6.75 GHz to 7.2 GHz at the end of this procedure.

The release from the trap and sequential state-selective imaging are performed as described in detail in Appendix A and in section 5.2, with the only difference being a shorter time-of-flight (1 ms). The experimental procedure detailed above was created to ensure the purity of the system and the absence of oscillations in position or shape. It results in a degenerate Bose gas with two components which we expect to be close to thermal equilibrium.

4.3 Results and analysis

Following the procedure of the previous section, we obtained absorption images of the two-component Bose gas close to thermal equilibrium (figure 4.1). While taking these images naturally sums over the atomic density in the z-direction, we integrate the resulting 2D density maps along the y-axis to obtain the 1D density profile along the x-axis. The peak densities (see figure 4.2) do not exceed 100 atoms/μm. For our trap parameters, this means that we can treat the clouds as 1D gases, similar to what was done for the single-component case [41, 121]. In figure 4.2, we show the measured 1D density profiles of the states $|1\rangle$ and $|2\rangle$ for six frequency values of the final evaporative cooling, illustrating the transition from the non-degenerate to the degenerate regime. A complication that arose in these experiments was that upon cooling to degeneracy, the experimental 1D profiles in figure 4.2 show strong fluctuations in the number of atoms and in the relative populations of the clock states.

We now want to compare our experimental data to the results from the thermodynamic Bethe Ansatz (TBA) calculations of ref. [47]. This is computationally intensive and requires searching in a multidimensional parameter space. Therefore we first calculate approximate parameters using a computationally simpler scheme, based on the *single*-component TBA (Yang-Yang) equations [41]. We now first describe this model. This will also be useful for the extension to the two-component case that we introduce subsequently.

The starting point is the numerically obtained equation-of-state in the form $n_{YY}(\mu, T)$ for the 1D density as a function of chemical potential μ and temperature T. For later reference, it is useful to point out here that convenient scaled units can be obtained as follows [122]. For a 1D coupling strength g, the relevant energy scale is

$$E_g = \frac{mg^2}{2\hbar^2}, \tag{4.1}$$

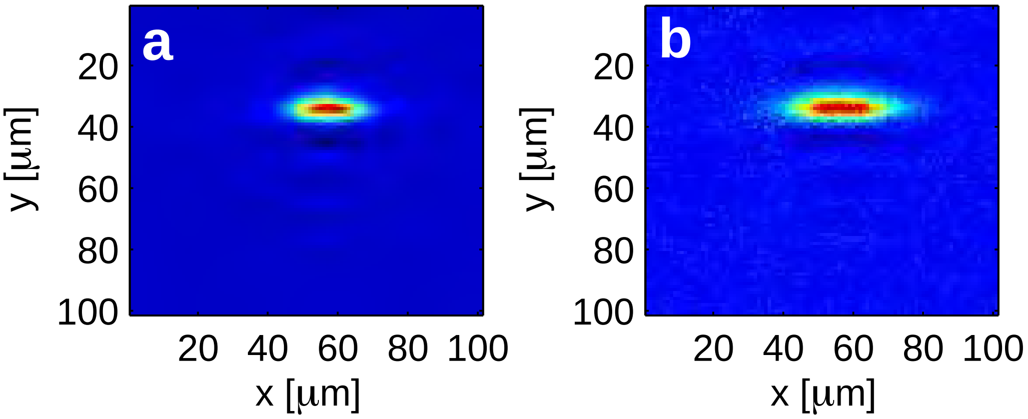

Figure 4.1: Absorption images of the density distribution of the two-component Bose gas near thermal equilibrium. For the profiles shown in this figure fifty density images, recorded under identical conditions along the z-axis, were averaged for each state. Subfigures (a) and (b) show the atomic density of states $|1\rangle$ and $|2\rangle$, respectively.

and the relevant length scale is

$$l_g = \frac{\hbar^2}{mg}. \tag{4.2}$$

Temperature and chemical potential are then most conveniently expressed in units of E_g, while 1D density n_{YY} is in units of $1/l_g$. For instance the famous Lieb-Liniger parameter is given by

$$\gamma = \frac{1}{n_{YY} l_g}. \tag{4.3}$$

The thermodynamic relation $n_{YY}(\mu, T)$ can be combined with the local-density approximation (LDA) to obtain the in-trap density distribution via a local chemical potential $\mu(x) = \mu(0) - V(x)$. An important practical extension is that we also need to account for population in radially excited states, since our temperatures are on the order of the radial level splitting $\hbar\omega_\perp$. This is done by treating each radially excited state (radial quantum number j, degeneracy $j+1$) as an independent ideal 1D Bose gas in thermal equilibrium with the radial ground state, at the same temperature T,

$$\mu_j = \mu(x) - j\hbar\omega_\perp. \tag{4.4}$$

The total linear density n_l is then given by

$$n_l(\mu(x), T) = n_{YY}(\mu(x), T) + \sum_{j=1}(j+1)n_e(\mu(x), T). \tag{4.5}$$

For the radially excited states we use the result of the LDA for the 1D ideal Bose gas,

$$n_e(\mu(x), T) = \frac{1}{\Lambda_T} g_{1/2}(\exp(\mu/k_B T)) \tag{4.6}$$

where $g_{1/2}$ is a Bose function and Λ_T is the thermal de Broglie wavelength

$$\Lambda_T = \sqrt{\frac{2\pi\hbar^2}{mk_B T}}. \tag{4.7}$$

As a first step, we fit the expression (4.5) to the experimental density distributions of each component separately. This neglects the interaction between the two states, and hence is not justified. Nevertheless, we expect that this will yield reasonably good values for the temperature, as we elaborate below, and reasonable starting values for the chemical potentials of the two components. The resulting best fits are shown in figure 4.2 as dashed curves. These fits are surprisingly good, considering the fact that this model ignores the interspecies interactions. The temperatures and chemical potentials extracted from these fits are shown in figure 4.3. The reason we expect the extracted temperatures to be reliable, is that these are dominated by the tails of the distribution, where effects of degeneracy and interaction become small. In that regime, neglecting the interspecies interaction should be justified. Indeed, for each RF value, the temperatures extracted from the two components are in good agreement. Based on the fitted parameters, we then proceed to obtain fit parameters from the two-component model.

For the TBA solution of the homogeneous *two*-component 1D Bose gas, the relevant parameters are the coupling strength g (required to be state-independent), the temperature and the two chemical potentials μ_{maj} and μ_{min}. We have used the TBA code kindly provided by the authors of [47]. This code takes the scaled values of temperature

$$t = \frac{k_B T}{E_g} \tag{4.8}$$

the average chemical potential

$$\tilde{\mu} = \frac{\mu_{maj} + \mu_{min}}{2E_g}, \tag{4.9}$$

and the difference in chemical potential

$$\Omega = \frac{\mu_{maj} - \mu_{min}}{2E_g}. \tag{4.10}$$

To obtain density curves that can be compared to the experiment, again the LDA is used, and the radially excited states are accounted for in the same way as in (4.5), with a separate peak chemical potential for the two components μ_{maj} and μ_{min}. We fix the temperature to the average of the two values obtained from the single-component fits (except for the data of figure 4.2(a), where the temperature of the majority component dominates). Next, we vary μ_{maj} and μ_{min} to be close to the peak (central) density of each component. The resulting density profiles are shown as solid curves in figure 4.2, while the used temperatures and resulting chemical potentials are shown in figure 4.3.

4.4 Discussion and outlook

The obtained fitted density distributions are in reasonable agreement with the experimental data. Before discussing possible reasons for the discrepancies, we first make a few more general remarks.

First, it should be pointed out that the usual bimodal description of partially condensed clouds does not work in 1D, as elaborated upon in ref. [41]. The main reason for this is that

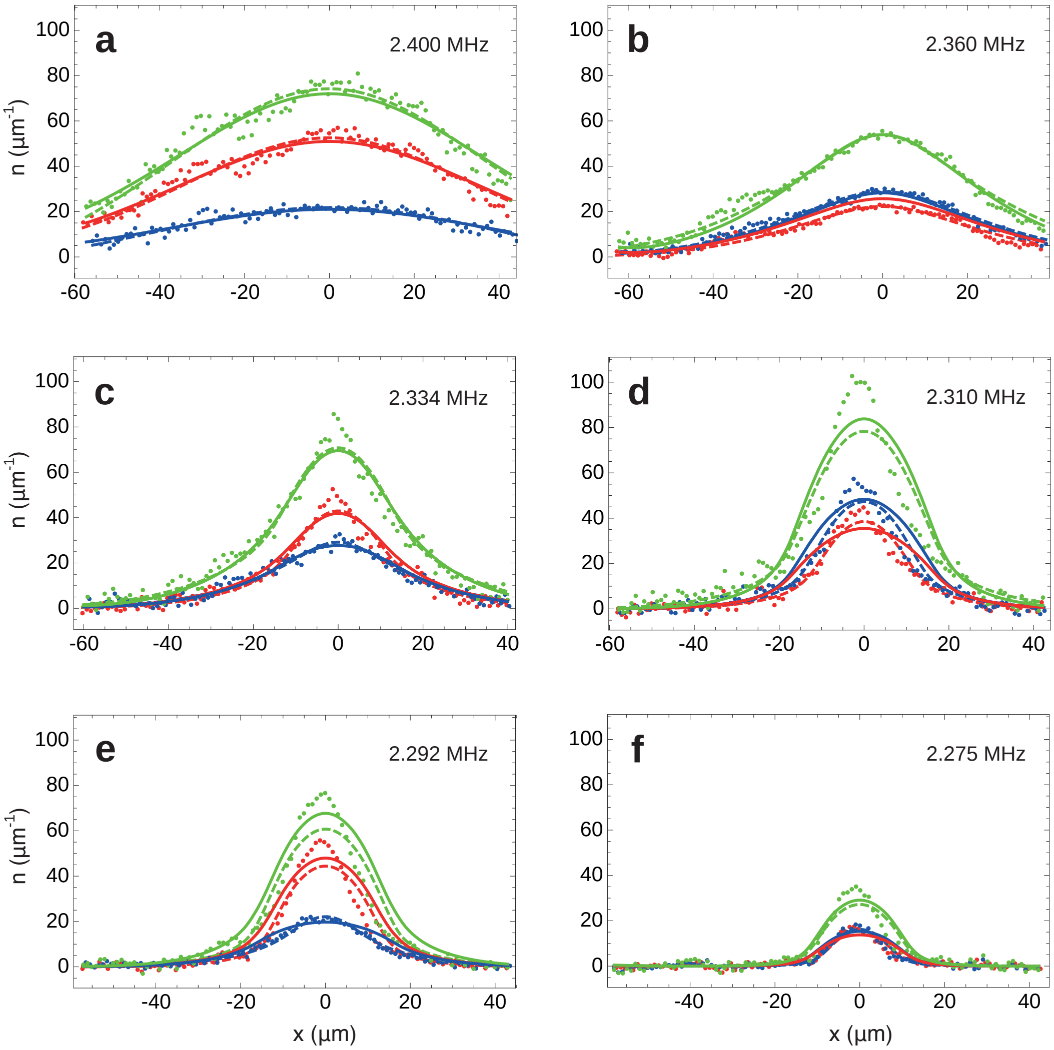

Figure 4.2: Averaged density distribution of two-component Bose gas near thermal equilibrium as a function of the final evaporation frequency. The densities of states $|1\rangle$ and $|2\rangle$ are colored red and blue, respectively. The overall density is colored green. The experimental data is represented by dots. To obtain the profiles, for each state 50 density images were recorded under identical conditions and averaged. The plots show the atomic density summed along the z-direction, i.e. the 1D-density. A single component fit to the data is indicated by dashed lines, while the solid lines represent a fit based on the thermodynamic Bethe-Ansatz (TBA) according to [47].

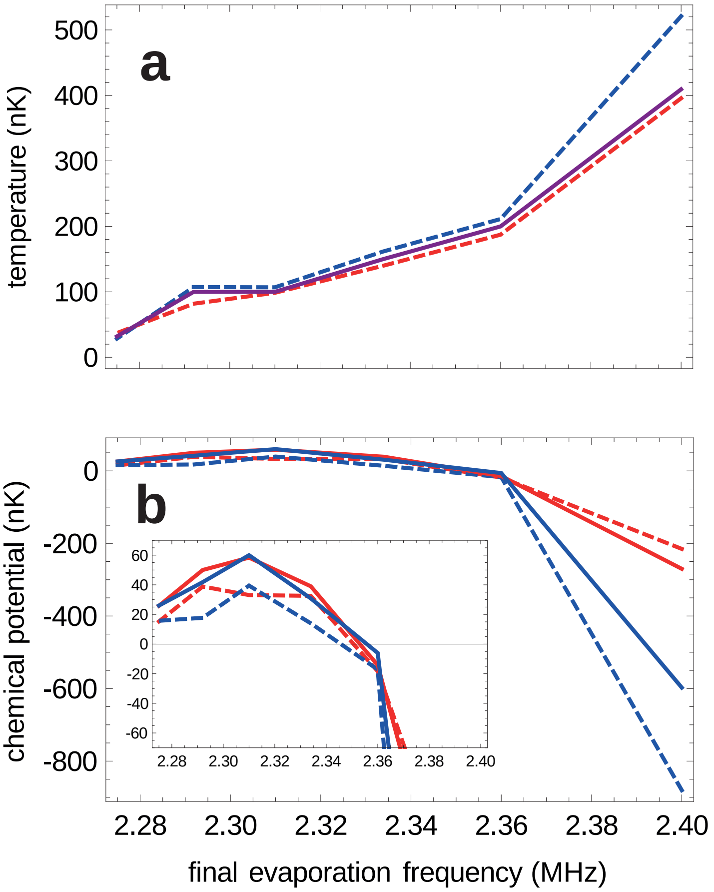

Figure 4.3: Temperature (a) and chemical potential (b) of the two-component 1D Bose gas as function of the final evaporation frequency. Fits based single-component calculations are shown as dashed lines. States $|1\rangle$ and $|2\rangle$ are colored red and blue, respectively. The solid purple line in (a) represents the temperature values used for the two-component TBA calculations, that yield chemical potentials shown as solid curves in (b).

the 1D ideal Bose gas exhibits a diverging density as the chemical potential approaches zero from below, so that the crossover from ideal-gas to (quasi-)condensate can not be properly described. The same argument holds for the two-component case, so that the two-component TBA solutions are an important tool in describing our data.

Second, the obtained chemical potentials for the two-component case are different from the separate chemical potentials from the single-component fits. This is to be expected from the results of ref. [47], which show that at low temperatures, the gas favors a strong polarization (difference in densities of the two components) even for small differences in chemical potential between the two components. This shows up in figure 4.3(b) as a much reduced difference in chemical potential for the two-component TBA fit, as compared to the two chemical potentials from the single-component TBA fits. In the experiments, the atom number is set (within experimental limitations). Hence, for a near-equal mixture, the required difference in chemical potentials in the two-component TBA rapidly diminishes as degeneracy is reached.

The main message of this work is that the two-component TBA calculations are very useful for our experimental results. There are, however, also several reasons why discrepancies are to be expected. First, as detailed in chapter 2, the interactions are not strictly state-independent because of the slight differences in scattering lengths among the two clock states of ^{87}Rb. For relatively high temperatures ($k_B T > n\Delta g$) one might expect these small differences to be of minor relevance. For our densities of order 50 per micron, the relevant energy scale is $n\Delta g/k_B = 1\,\mathrm{nK}$. Our temperatures are higher than this scale (see figure 4.3(a)), so that this may not be a limiting factor. On the other hand, as we will see in the next chapter, these small energy differences can lead to significant dynamics at long time scales ($\approx 100\,\mathrm{ms}$). This is comparable to the time of evaporative cooling used here.

Another, harder to address, issue is the coherence between the two states. The goal has been to eliminate this coherence by the losses and dissipation of the evaporative cooling process. It is, however, hard to test to what extent this leads to complete decoherence.

For a completely coherent mixture, one would actually expect the single-component description to work for the total density. For the fully decoherent mixture the two-component TBA description should be applicable. Our experimental data shows similar agreement to best fits for both models, so that we are unable at this point to decide on the achieved (de)coherence based on this comparison.

Generally, the visibility of effects associated with the two-component gas and the comparison to TBA theory would benefit from a strong increase in interaction strength. For a more strict adherence to the condition of state-independent interactions (allowing a more detailed comparison to TBA theory) it would be desirable to extend the experiments of this chapter by combining this approach with the techniques of the following chapter. Namely, a next step would be to try and obtain thermal equilibrium in a two-component Bose gas via evaporative cooling, while tuning the one-dimensional interaction parameters to the point of integrability (via state-dependent potentials). While this natural combination of ideas has not escaped our attention, it is beyond the scope of the present thesis. Pursuing further investigations along these lines is left as a challenge for others.

Chapter 5

Controlling one-dimensional spin motion with state-dependent potentials

5.1 Introduction

In this chapter, we present the main results of this thesis. These results have also been submitted for publication [123]. We show that radio-frequency-dressed potentials on atom chips offer a new way to tune the effective interactions in 1D and to control spin motion. We make use of the fact that, for elliptical RF polarizations, different hyperfine states experience different dressed potentials, allowing for state-dependent manipulation [124]. Here we exploit the dependence of the 1D coupling strength on the transverse confinement frequency $\omega_\perp$ [34]. By tuning the transverse confinement for the two states independently through the RF polarization and amplitude, we show that it is possible to control the interactions in a state- and time-dependent manner. Suddenly changing interactions, combined with the state dependence of the axial trapping then results in dynamical evolution in the spin degree of freedom. In particular, we are able to tune to *(i)* the point where the spin motion is frozen, and *(ii)* the point where the 1D interactions become spin-independent.

5.2 Experimental procedure

We first discuss our results on the one-dimensional non-equilibrium dynamics for state-*in*dependent potentials, highlighting the importance of small differences in interaction parameters. The experimental procedure of the experiments detailed in this chapter is similar to the one used for the experiments of chapter 4. In fact, the individual steps of the two procedures are identical up to an intermediate step in a series of evaporative cooling stages. Whereas in chapter 4 we first mixed the states $|1\rangle$ and $|2\rangle$ when the gas could still be considered non-degenerate and then continued evaporative cooling to degeneracy, here all cooling is performed prior to creating a two-component system. We provide a documented example of the program code used to generate a two-component 1D Bose gas in Appendix A.

The starting point of our experiments is a nearly-pure 1D quasi-condensate in the $|1\rangle = |F=1, m_f=-1\rangle$ state of ^{87}Rb in a highly elongated magnetic trap created by an atom chip. To prepare this state, initial evaporative cooling to 120 kHz above the trap bottom is performed (see chapter 4.2), leading to a cold, non-degenerate gas. After this, we apply a short RF pulse with a frequency of 2.22 MHz. This serves to transfer atoms from $|F=2, m_f=2\rangle$ to $|2\rangle = |F=2, m_f=1\rangle$, as described in chapter 4.2.

Then, we drive a two-photon transition by applying a combined RF (1 MHz)- and MW (6.83 GHz) field. For a pulse time of 0.5 ms, the atomic population is transferred from $|2\rangle$ to $|1\rangle = |F=1, m_f=-1\rangle$ with nearly 100% transfer efficiency. The single transitions are detuned by 1.26 MHz from the intermediate $|F=2, m_f=0\rangle$ level to avoid transfer to this untrapped state. Subsequently, the trap is tightened by ramping up the current in chip wire 5 and the coils responsible for the bias field within 60 ms. This creates a highly elongated Ioffe-Pritchard microtrap with trap frequencies of $\omega_\perp/2\pi = 1.9\,\text{kHz}$ and $\omega_\parallel/2\pi = 26\,\text{Hz}$.

In the following step, we perform a second and final RF evaporation sweep to $\approx 25\,\text{kHz}$ above the trap bottom in order to achieve quantum degeneracy of state $|1\rangle$. This sweep is accompanied by a MW pulse to remove the still populated fully stretched state $|F=2, m_f=2\rangle$ by coupling to the untrapped $|F=1, m_f=1\rangle$ state. The peak linear atomic density is $n_1 \lesssim 100\ \mu\text{m}^{-1}$. In this system, both the temperature and chemical potential are small compared to the radial excitation energy $(\mu, k_B T < \hbar\omega_\perp)$ and the dynamics are restricted to the axial dimension (1D regime).

From this clean starting point, in which only state $|1\rangle$ has a noticeable population, we induce a sudden transition to a coherent superposition of the $|1\rangle$ and $|2\rangle = |F=2, m_f=1\rangle$ hyperfine states via a second two-photon pulse, effectively creating a spin-1/2 system [84, 111]. We recorded Rabi oscillations between the two coupled states by varying the two-photon pulse duration and determining the number of atoms per state. An example of the oscillations, recorded under slightly different conditions, is shown in figure 5.1. From a sine fit to this data we deduce a two-photon Rabi frequency of 1.8 kHz.

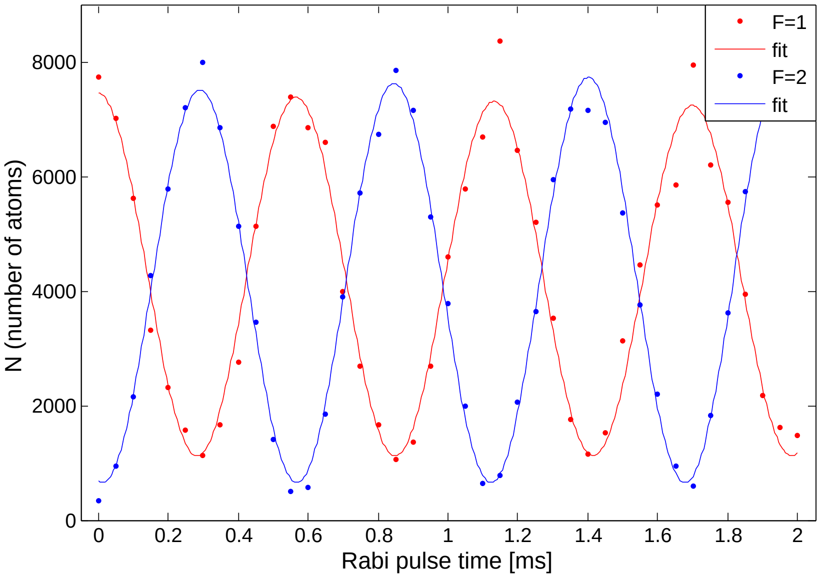

Figure 5.1: Rabi oscillations between states $|1\rangle$ and $|2\rangle$ driven by coherent two-photon transition. The number of atoms in states $|1\rangle$ and $|2\rangle$ is indicated red and blue, respectively. Sine fits to the data yield a Rabi frequency of 1.8 kHz.

The two-photon Rabi frequency for the experiments described here is determined as 1.14 kHz, corresponding to a $\pi/2$-pulse duration of 0.22 ms. This is fast compared to the timescale for axial dynamics, but sufficiently slow to prevent radial excitations. Coherence times in excess of 1 s have been measured in this setup via Ramsey spectroscopy of dilute thermal clouds.

After performing a $\pi/2$-pulse, which leads to an equal mixture of atoms in states $|1\rangle$ and $|2\rangle$, the resulting non-equilibrium situation is allowed to evolve. The time evolution of the spin distribution is measured by varying the hold time and subsequent sequential state-dependent absorption imaging.

After a short time-of-flight of typically 1 ms, we image the longitudinal distributions, and obtain the linear densities n_1 and n_2 of the two states along the length of the trap by integrating along the radial direction. Atoms in state $|2\rangle$ are imaged directly using absorption on the $F = 2, F' = 3$ transition with an exposure time of $30\,\mu$s and an optical resolution of $4.2\,\mu$m. Due to an extra repumping step we find a 20% lower detection efficiency for state $|1\rangle$ and a poorer resolution of $\sim 8\,\mu$m due to photon recoil, visible in figure 5.8.

5.3 Spin motion

In figure 5.2 we present measurements of the evolution of spin polarization $(n_1 - n_2)$ and the total linear density $(n_1 + n_2)$ as a function of hold time. The spin pattern shows clear dynamical evolution [figure 5.2(a)] whereas the total density remains approximately constant with no significant dynamics [figure 5.2(b)]. The spin dynamics can be interpreted as a “focusing” of state $|2\rangle$ in the presence of state $|1\rangle$, resulting in a negative spin polarization $(n_2 > n_1)$ toward the center of the trap.

We find good agreement with the experimental data using the coupled 1D Gross-Pitaevskii equations (1D-GPE) with solutions also shown in figure 5.2(c,d). The 1D-GPE is obtained by integrating the full 3D-GPE over the transverse ground-state wavefunctions (see equations (2.26)), with interaction parameters derived from the intra- and interstate scattering lengths taken from ref. [98]: $a_{11} = 100.4 \cdot a_0$, $a_{22} = 95.44 \cdot a_0$ and $a_{12} = 98.006 \cdot a_0$, where a_0 is the Bohr radius. Generalizing for state-dependent harmonic confinement (as will be relevant below) we obtain for the 1D interaction parameters u_{ij} (equations (2.27) with $\omega_{iy} = \omega_{iz}$):

$$\begin{aligned} u_{11} &= 2\hbar\omega_{\perp,1}a_{11}, \\ u_{22} &= 2\hbar\omega_{\perp,2}a_{22}, \\ u_{12} &= 4\hbar\frac{\omega_{\perp,1}\omega_{\perp,2}}{(\omega_{\perp,1}+\omega_{\perp,2})}a_{12}, \end{aligned} \tag{5.1}$$

with $\omega_{\perp,j}$ the transverse trap frequency for state $|j\rangle$. Similarly we use values for the scaled rate constants for inelastic two-body and three-body losses derived (see equations (2.28)) from the 3D values in ref. [98]. The 1D-GPE simulations reproduce the features of the experiment, i.e. absence of dynamics in the total density and the overall structure of the spin dynamics including the time of maximum state separation around $t \approx 75$ ms.

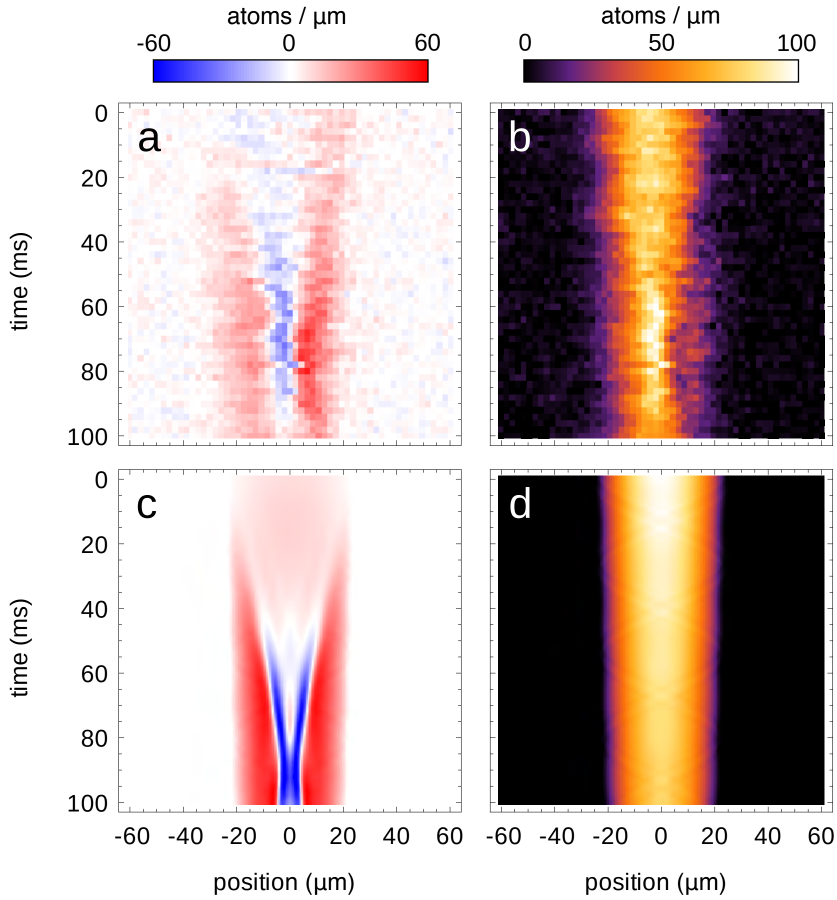

Figure 5.2: One-dimensional spin dynamics and total density after a sudden transfer of internal-state population, for the case of state-independent trapping potentials. Shown are spin polarization ($n_1 - n_2$, left) and total linear density ($n_1 + n_2$, right), as a function of axial position and time after the transfer. Top: experiments, bottom: corresponding simulations resulting from integration of two coupled 1D Gross-Pitaevskii equations (GPE). The spin polarization data clearly shows how n_2 is focused towards the center (blue), while n_1 moves towards the sides (red); the total density shows little dynamics. Differences between experiment and simulation can be explained by the limited optical resolution of our imaging system and a small tilt of the trap, leading to a slight spatial asymmetry in the experiments.

The decay in atom number on a $\gtrsim 100$ ms timescale is dominated by two-body losses in intrastate interactions and between $|2\rangle$ atoms (γ_{12} and γ_{22}) [98].

The rate of spin focusing/defocusing is critically dependent on the precise differences in 1D interaction strengths for the respective internal states, a fact that is readily confirmed by changing these differences in the simulations. The observed general behavior can be understood as follows: in the initial state (an interacting trapped quantum gas in a single internal state in equilibrium) the repulsive interactions balance the external confining potential. Suddenly transferring a fraction of the population to a second internal state with weaker intra- and interstate interactions results in a net contracting force (a confining effective curvature, $c_2 > 0$ in equations (5.3) below) on the population in this second state that dominates the dynamics in the spin polarization. Because the spin-dependent part of the interactions is relatively small, the dynamics in the *total* density are dominated by the (relatively large) average scattering length which remains nearly constant. Hence the total density shows only weak dynamics; the focusing in n_2 is accommodated by "pushing" n_1 to the sides (red in figure 5.2).

5.4 Controlling spin motion in a 1D Bose gas

We now describe the state-dependent radio-frequency-dressed potentials that we use to control the spin motion. We consider near-resonant coupling ($\hbar\omega_{rf} \lesssim g_F\mu_B|B|$) of the RF-field with tuneable polarization determined by the relative phase of two independently controlled RF-fields. A cross section of the wire geometry used is shown in figure 5.3(a). The fields originate from direct digital synthesis (DDS) supplied currents in two wires neighboring the Z-shaped trapping wire [125]. With these two fields we can readily control the ellipticity of the total RF-field at the trap position by controlling the relative phase ϕ of the RF currents in the two wires. This includes linear (horizontal and vertical) and circular ($\sigma^{\pm}$) polarizations.

The corresponding dressed-state potential for state $|j\rangle$ (with $j = 1, 2$) has the form $V_j(x, y, z) = ((V_0(x, y, z) - \hbar\omega_{rf})^2 + \hbar^2\Omega_j^2)^{1/2}$ where $V_0(x, y, z)$ is the bare magnetic (harmonic) potential. The state-dependent part of the potential enters through the coupling Rabi frequency Ω_j [126, 94] (see equation 2.9), which acts to weaken the overall confinement near the trap bottom by an amount given by the dressing parameter δ_j. Taking the second derivative of the potential V_j around the origin yields new trap frequencies,

$$\tilde{\omega}^2_{\perp,\parallel} = \delta_j\omega^2_{\perp,\parallel}, \text{where } \delta_j = \Delta/\sqrt{\Omega_j^2 + \Delta^2}, \tag{5.2}$$

with detuning $\Delta = \omega_L - \omega_{rf}$ and Larmor frequency ω_L.

The state-dependent RF potential is characterized using dressed-state RF spectroscopy with a weak additional RF probe [127, 128]. The potential energy at the trap bottom is characterized by the onset of loss as a function of probe frequency which we fit to extract $V_j(0, 0, 0)$. Figure 5.3(b) shows the measured trap bottom as a function of the dressing

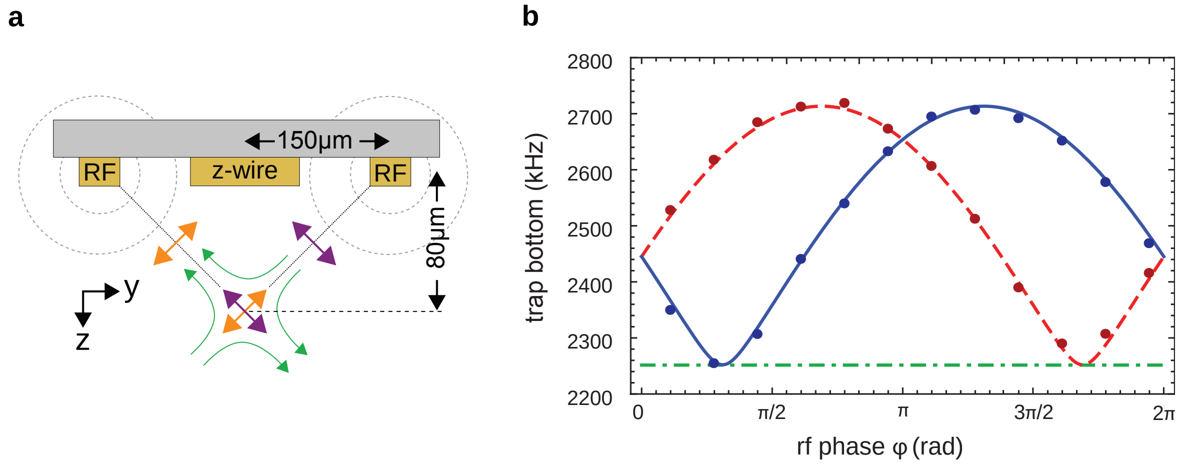

Figure 5.3: State-dependent potentials. (a) wire geometry used for state-dependent radio-frequency-dressed traps (as in fig. 2.3). The static quadrupole magnetic field and the two RF-fields are indicated by green, orange and purple arrows respectively. The direction of the bias *Ioffe* field which defines the quantization axis is into the plane of the figure. (b) Trap bottom determined via dressed state RF spectroscopy as a function of ϕ. Data points correspond to the measured trap bottom for state $|1\rangle$ (red) and state $|2\rangle$ (blue). Solid and dashed curves are fits to the data. The dash-dotted green line indicates the fitted trap Larmor frequency $\omega_L/2\pi = 2.25$ MHz.

phase ϕ, for $\omega_{rf} = 2\pi \times 2.20$ MHz. The trap bottom varies with RF phase between 2250 kHz and 2700 kHz corresponding to a maximum Rabi frequency of $\Omega_j/2\pi = 450$ kHz. For $\phi = 0.31\pi$ and $\phi = 1.68\pi$ the potential is maximally state-dependent, corresponding to the pure circular polarizations σ^- and σ^+ respectively (dressing only state $|1\rangle$ and only state $|2\rangle$, respectively). The potentials are state-independent for linear polarization at $\phi = 0, \pi$ (equal dressing of state $|1\rangle$ and $|2\rangle$). The deviation from a simple $\sin^2(\phi)$ behavior is due to the wire geometry, as the two RF-fields are not quite orthogonal at the trap position.

A fit to the data (solid and dashed curves) taking into account the wire geometry results in an accurate calibration of the key experimental parameters, in particular the Larmor frequency $\omega_L = 2.25$ MHz, RF-field amplitudes $b_1 = b_2 = 0.53$ G from the two RF wires and the trap-surface distance of 80 μm.

To control the spin motion we turn on the state-dependent dressing directly after preparing the equal superposition of $|1\rangle$ and $|2\rangle$. This is done by ramping up the RF currents through chip wires 3 and 6 within 2 ms. The radio-frequency, $\omega_{rf} = 2\pi \times 2.20$ MHz, is chosen slightly below the trap bottom to prevent the formation of a double-well potential. The ramp time is slow compared to the inverse Larmor frequency and the inverse radial trap frequency, but sudden with respect to any axial motion. We use the two circular RF polarizations and various RF amplitudes, corresponding to $0.8 < \delta_1 < 1, \delta_2 = 1$ and $0.8 < \delta_2 < 1, \delta_1 = 1$. For each time step we extract the widths of the axial distributions in both states.

Results for the full range of dressing parameters are depicted in figure 5.6. Figure 5.6(a) shows the calculated interaction strengths taken from equation (5.1) as a function of δ_1 and δ_2. We have compared the measured widths of the distributions as a function of time

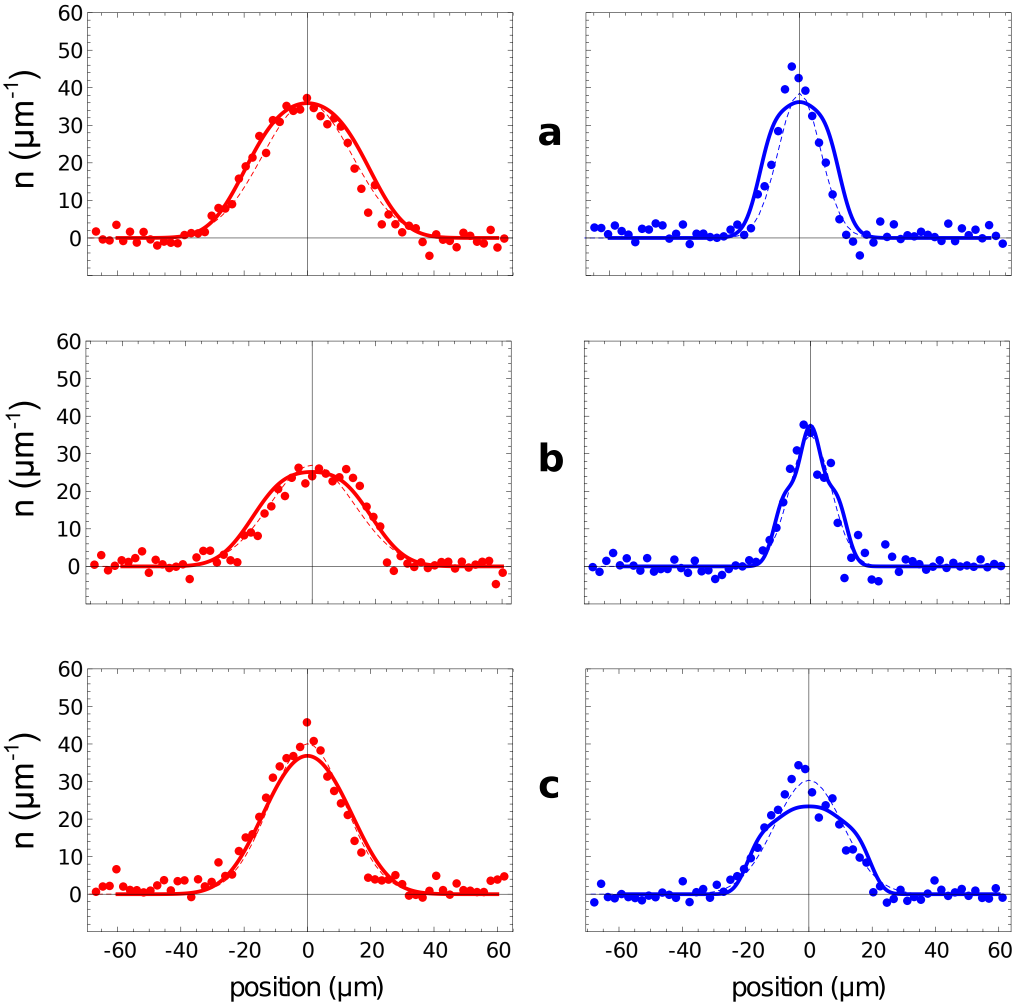

Figure 5.4: 1D density profiles at hold time $t = 44\,\mathrm{ms}$ for (a) no RF dressing, (b) dressing of state $|1\rangle$ alone ($\phi = 0.31\pi$, $\delta_1 = 0.904$) and (c) dressing state $|2\rangle$ alone ($\phi = 1.68\pi$, $\delta_2 = 0.968$). States $|1\rangle$ and $|2\rangle$ are indicated in red and blue, respectively. The experimental data is represented by dots, gaussian fits by thin dashed lines and the profiles resulting from the corresponding coupled 1D-GP simulation are represented by solid lines.

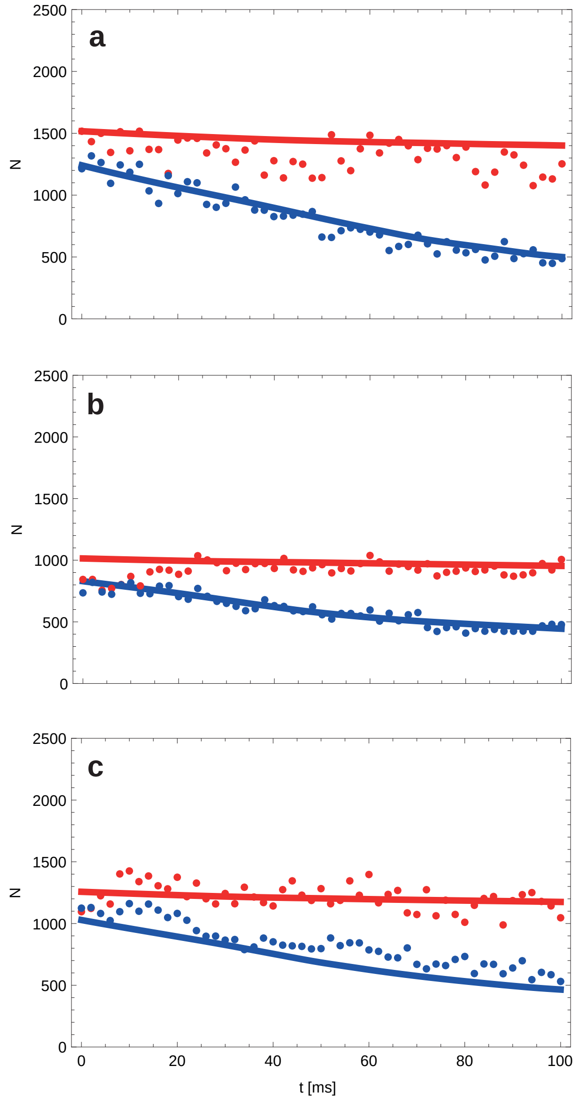

Figure 5.5: Number of atoms in states $|1\rangle$ (red) and $|2\rangle$ (blue) as function of the hold time in the magnetic trap for three different RF dressing parameters. Subfigure (a) corresponds to no RF dressing, (b) to dressing of state $|1\rangle$ alone ($\phi = 0.31\pi$, $\delta_1 = 0.904$) and (c) shows the data for dressing state $|2\rangle$ alone ($\phi = 1.68\pi$, $\delta_2 = 0.968$). The solid lines are the corresponding decay curves obtained from the GP simulations.

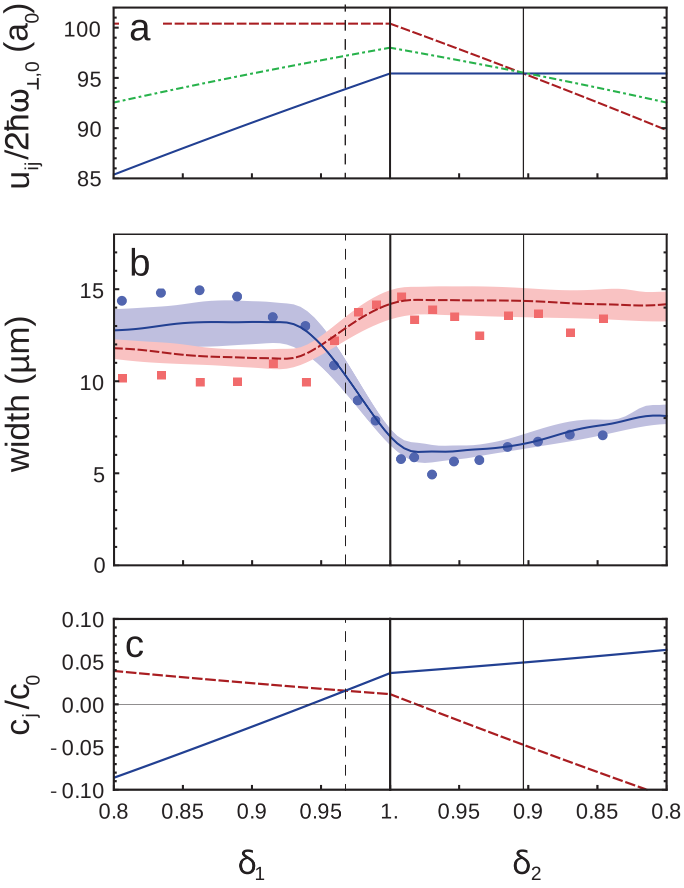

Figure 5.6: Overview of the possibilities of the state-dependent potentials, as a function of the dressing parameters (left: varying δ_2, with $\delta_1 = 1$; right: varying δ_1 with $\delta_2 = 1$). (a): 1D interaction strengths, u_{ij} normalised by the bare transverse trap frequency $\omega_{\perp,0}$. (b) Widths of the distribution at $t = 44\,\text{ms}$ and (c) scaled effective curvature c_j/c_0 at $t = 0$. Red indicates state $|1\rangle$ (and u_{11}) and blue state $|2\rangle$ (and u_{22}) and in (a) u_{12} is indicated in green. The widths in (b) are obtained by a fit to the experimentally measured density profiles (dots) and to GPE simulation (shaded regions). The shaded areas in (b) represent the effect of shot-to-shot atom number fluctuations in the experiment.

with solutions of the coupled 1D-GPE. An example of Gaussian fits to the experimental data taken at $t = 44\,\mathrm{ms}$ including the corresponding 1D density profiles resulting from the 1D-GPE simulations is shown in figure 5.4. The evolution of the number of trapped atoms with hold time is given in figure 5.5. The observed decay of the atom numbers matches the simulation based on the numbers in ref. [98]. The widths and the corresponding simulations for one fixed hold time of 44 ms are shown in figure 5.6(b). The measured widths follow the 1D-GPE simulations closely (taking into account the finite optical resolution), with the biggest uncertainties originating from atom number fluctuations which cause the peak linear density to vary between $70\mu\mathrm{m}^{-1}$ and $100\ \mu\mathrm{m}^{-1}$ throughout the entire data set (systematic uncertainty shown by shaded regions). The solid vertical line at $\delta_1 = 0.904$ indicates the point where the difference in interaction strengths is minimized [figure 5.6(a)] with u_{11}, u_{22} and u_{12} differing by less than 0.09% (30 times reduction in differences when compared to the unmodified interactions). These conditions are of interest for comparing to Bethe Ansatz solutions which require spin-independent interactions [27, 47].

In the two-component ("spin-1/2") 1D Bose gas, the presence of spin-independent (symmetric) interactions is of particular interest. For all interaction strengths (weak and strong) the dispersion relation of spin waves is quadratic here [104, 27], and the low-energy spin velocity vanishes. As a consequence the usual Luttinger-liquid description [129, 30, 130, 40] cannot be applied. However, it is precisely the point where exact Bethe Ansatz methods can be used [27, 47]. Furthermore, it is the point where buoyancy effects vanish and in the weakly interacting (mean-field) regime it also lies on the border that separates miscible and immiscible regimes of binary superfluids [104], see figure 2.5.

5.5 Effective potentials

To explain the data we have to consider both the effect of RF-dressing on the collisional interaction strengths as well as the state-dependent modification to the axial potential. A simple analytical description can be obtained using a Thomas-Fermi description near the cloud center where the cloud shape is an inverted parabola. The combination of the state-dependence of the axial trapping frequency and of the interactions can then be expressed as a net harmonic potential characterised by an effective state-dependent curvature c_j. We solve for the effective curvatures (figure 5.6c) for $t \gtrsim 0$ in our experiments in terms of δ_j, and find

$$\begin{aligned} \frac{c_1}{c_0} &= \delta_1 - (1-\beta)\sqrt{\delta_1} - \frac{a_{12}}{a_{11}} \frac{2\beta\sqrt{\delta_1\delta_2}}{\sqrt{\delta_1}+\sqrt{\delta_2}} \\ \frac{c_2}{c_0} &= \delta_2 - \beta\frac{a_{22}}{a_{11}}\sqrt{\delta_2} - \frac{a_{12}}{a_{11}} \frac{2(1-\beta)\sqrt{\delta_1\delta_2}}{\sqrt{\delta_1}+\sqrt{\delta_2}} \end{aligned} \tag{5.3}$$

Here the first term on the right-hand side reflects the modification to the external axial potential and the second and third terms deal with the modified interactions u_{ij}. The axial curvature of the bare potential is $c_0 = \omega_{\parallel}^2/2$ and β corresponds to the fraction of the population transferred to state $|2\rangle$ ($\beta \approx 1/2$ for our experiments).

The dashed line at $\delta_2 = 0.968$ in figure 5.6 indicates the point where the difference in interactions is compensated by the state-dependent longitudinal potential and $c_1 = c_2$. This point is characterized by small equal curvatures of the effective potentials (including interaction energy) for both states [figure 5.6(c)], which result in frozen spin dynamics. These conditions are important for applications with on-chip atomic clocks, to minimize inhomogeneous broadening due to mean field shifts. For $\delta_2 < 0.968$ the difference in interaction strengths is further enhanced and the time evolution of the spin dynamics becomes inverted, with focusing of state $|1\rangle$ while state $|2\rangle$ is pushed outward, as is visible in figure 5.6(b).

Figure 5.7 shows the full time evolution of the spin polarization for two selected RF-dressing parameters. The selected cases are: dressing of state $|1\rangle$ alone ($\phi = 0.31\pi$, $\delta_1 = 0.904$) [figure 5.7(a)] and dressing state $|2\rangle$ alone ($\phi = 1.68\pi$, $\delta_2 = 0.968$) [figure 5.7(b)], corresponding to the intersection points in figure 5.6(a) and (c), respectively. Qualitatively state $|2\rangle$ focuses faster with RF-dressing applied to state $|1\rangle$, when compared to the case of state independent potentials [figure 5.2(a)]. Generally, the simulated density profiles reveal a rich and dynamic nonlinear evolution of the spin polarization, reminiscent of filament propagation in optical systems with competing nonlinearities [131]. This is clearly visible in figure 5.7(c) for example. This detailed structure depends sensitively on the precise values of the dressing. The development and propagation of this fine structure in the spin polarization is partially observed in the experimental data, but is not fully resolved due to the finite imaging resolution. Convolving the simulated profiles with the point-spread function of our imaging system yields excellent agreement with all of the data. With weak dressing of state $|2\rangle$ ($\delta_2 = 0.968$) it is possible to freeze spin dynamics altogether such that the two states maintain their overlap and the widths remain constant (apart from a small in-phase quadrupole oscillation and decay from state $|2\rangle$), see figure 5.7(b,d). A more quantitative representation of the data, showing excellent agreement between experiment and simulation, is given in figure 5.8, where the widths of the two states are shown for different evolution times. Clearly, the focus point can be identified in figure 5.8(a) around $t = 75$ ms and in figure 5.8(b) around $t = 30$ ms, whereas no focussing is present in figure 5.8(c).

5.6 Outlook

We have shown that by introducing a small state-dependence to the radial trapping potential using RF-dressing we can precisely tune the 1D interaction parameters in a two-component quantum gas by more than 10%, over an experimentally significant range. In our experiments this modification competes with the state dependence of the axial trapping and provides a new “knob” to control spin motion, leading to tuneable nonlinear behavior.

Our method can be naturally extended in several ways. For instance, control over the interactions *without* the accompanying state-dependence of the axial trapping can be obtained by using one-dimensional box-shaped potentials [125]. By introducing an additional displacement of the transverse potential in a state-dependent way it is possible to further

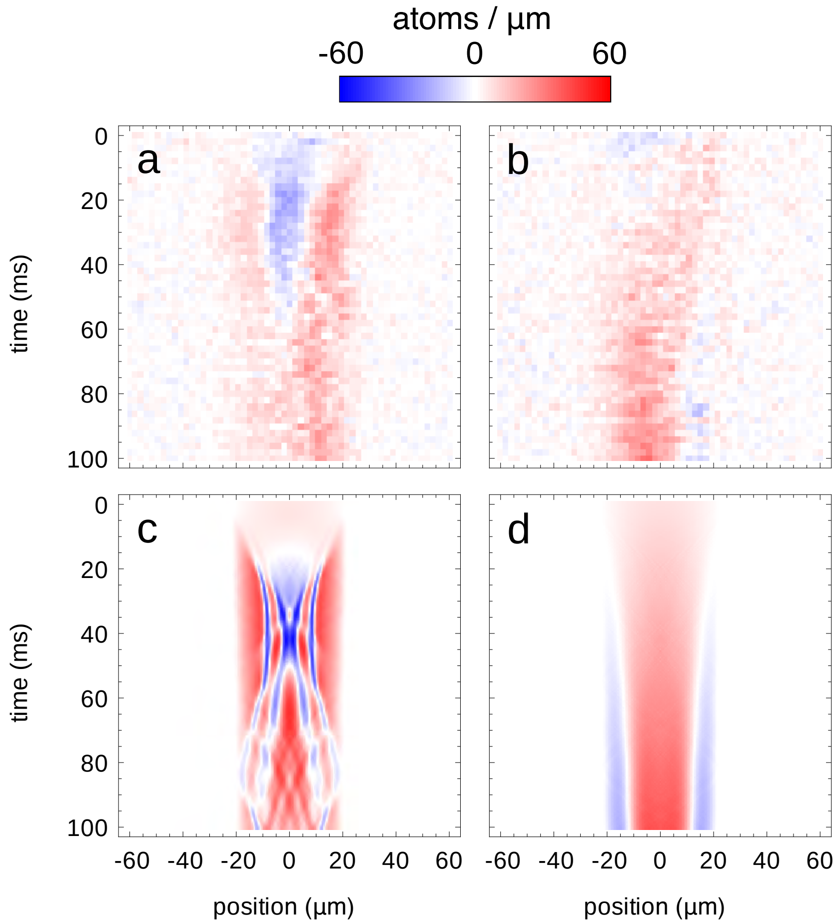

Figure 5.7: Spatiotemporal behavior of the spin polarization $(n_1 - n_2)$ following the sudden transfer to the state-dependent potentials. States $|1\rangle$ and $|2\rangle$ are indicated red and blue, respectively. (a) shows the evolution with RF parameters corresponding to equal inter-atomic interactions $(\delta_1 = 0.904, \delta_2 = 1)$ and (b) equal effective potentials $(\delta_1 = 1, \delta_2 = 0.968)$. (c) and (d) show the results of 1D-GPE simulations corresponding to (a) and (b), respectively.

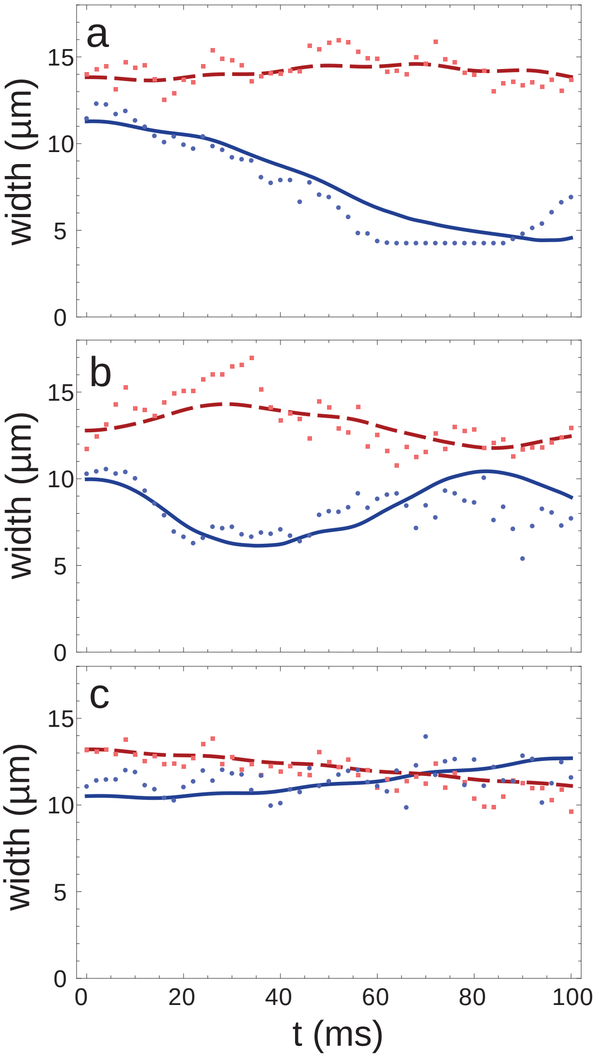

Figure 5.8: Widths of the atomic distributions as function of hold time, for the parameters indicated by the three vertical lines in figure 5.6. Dots are fits to experimental data, lines are results of 1D GPE solutions. States $|1\rangle$ and $|2\rangle$ are indicated red and blue, respectively. In (a) no RF-dressing is applied $\delta_{1,2} = 1$, as in figure 5.2. (b) and (c) correspond to the data in figure 5.7. (b) shows the evolution with RF parameters corresponding to equal inter-atomic interactions ($\delta_1 = 0.904, \delta_2 = 1$), and (c) equal effective potentials ($\delta_1 = 1, \delta_2 = 0.968$).

reduce u_{12}, allowing all three interaction parameters to be tuned independently, something that is not generally possible with a magnetically controlled Feshbach resonance.

The observed spin dynamics depend critically on the precise differences in interaction strengths. For ^{87}Rb, the three relevant scattering lengths are nearly equal and therefore weak dressing is sufficient to tune the system parameters to the point of symmetric interactions or to where the spin dynamics become frozen. Since the RF parameters can be precisely known, such experiments could also allow precision determination of the scattering length differences. More generally, tuning the system parameters around the point of spin-independent interactions strongly affects the dispersion relation of the spin excitations [104]. In particular this allows the spin velocity to be tuned around zero, providing a new handle for the study of spin waves in one-dimensional atomic gases.

Tunable interactions in two-component quantum gases have important applications in the areas of spin-squeezing and quantum metrology [61, 62], and the ability to control spin motion opens new avenues for future studies of quantum coherence in interacting quantum systems [30, 111, 85, 86, 132]. Our current experiments are performed in the weakly interacting 1D regime and at low temperature, and we find that a description based on two coupled 1D Gross-Pitaevskii equations is sufficient to describe our data. The methods presented here to tune interactions are not limited to this regime, however. In particular, we plan to apply these methods to systems with stronger interactions (e.g., by lowering the 1D density) and with higher temperatures. This will provide experimental tests of (and challenges to) more sophisticated theoretical methods, for both equilibrium and non-equilibrium phenomena. For instance, it will be possible to experimentally explore predictions of the thermodynamic Bethe Ansatz for the two-component Bose gas [47] (as already indicated in chapter 4) and to explore quantum quenches in strongly interacting 1D systems by dynamical control over the spin-dependent interactions. Finally, we expect that the experimental control over spin motion and interactions, as demonstrated here, will benefit the realization of spin-“charge” separation in a Bose gas [27, 29].

Chapter 6

Extension to Bose-Fermi mixtures

6.1 Introduction

All results presented in this work were obtained with the CELSIUS apparatus described in chapter 3. Even though the existing setup has proven very fruitful and reliable, there are a number of improvements on our wish list for a next generation setup. First and foremost, we intend to extend our studies of one-dimensional (1D) systems to Bose-Fermi and Fermi-Fermi mixtures. Atom chips offer many advantages in this regard: rapid sympathetic cooling of the fermion ^{40}K by the boson ^{87}Rb on an atom chip has already been demonstrated [133], atom chips enable the study of individual realizations of 1D quantum gases [41, 124], and finally they make possible the use of versatile radio-frequency dressed potentials [124, 128] that can be both state- and species-selective [134]. The latter allows tuning the interaction parameters, which enables comparison to exactly solvable models in our experiments (see chapter 5). Our interest is in dynamics, coherence, relative phase, phase separation [135] and coupling between components of a Bose-Fermi mixture in one dimension. Apart from an added species, an improved general performance is desirable. A new apparatus should provide a longer vacuum lifetime, shorter experimental cycle times, better optical access and increased flexibility in the use of on-chip traps.

In this chapter, we present our design of the KELVIN (K15, Experiment for Low-dimensional, Variable-Interaction systems, Next generation) apparatus to investigate quantum degenerate mixtures of Rb and K. It includes a double chamber vacuum setup and a two-species mirror-MOT powered by a system of amplified diode lasers. The setup can be subdivided into three parts: the diode laser system, the vacuum system and the atom chip.

6.2 Laser system

Coherent light for cooling, repumping, optical pumping and imaging of ^{87}Rb (780 nm) and ^{40}K (767 nm) is provided by a system of diode lasers, acousto-optical modulators (AOMs) and tapered amplifiers (TAs) (see figure 6.1). Three grating-stabilized external cavity diode lasers (ECDLs) serve as master lasers for the cooling light for Rb and K and the repumping light for K. The lasers are frequency-stabilized by means of FM-spectroscopy. Whereas standard laser diodes in home-built mounts are used for the Rb lasers, an anti-reflection coated diode with a broad gain spectrum (Eagleyard, EYP-RWE-0790) [136] is employed as K master laser. Repumping light for K is generated by frequency-shifting part of the 767 nm light by 1.2 GHz with an AOM in four-pass configuration and subsequent amplification by injection into a high-power slave laser. Amplification by three

TAs (Eagleyard, EYP- TPA-0780 for Rb and EYPTPA-0765 for K) in home-built, highly temperature-stable mounts, yields a total power of maximally 2 W per amplifier. A splitting and frequency shifting stage consisting of ten doubly passed AOMs allows independent control over the individual frequencies. After recombination according to time and location of its application, all light is coupled into six single-mode optical fibers, guiding it towards outcouplers mounted around the vacuum chamber. In this manner the laser light arriving at the chamber has perfect gaussian mode profiles and stray light from the laser system can easily be shielded.

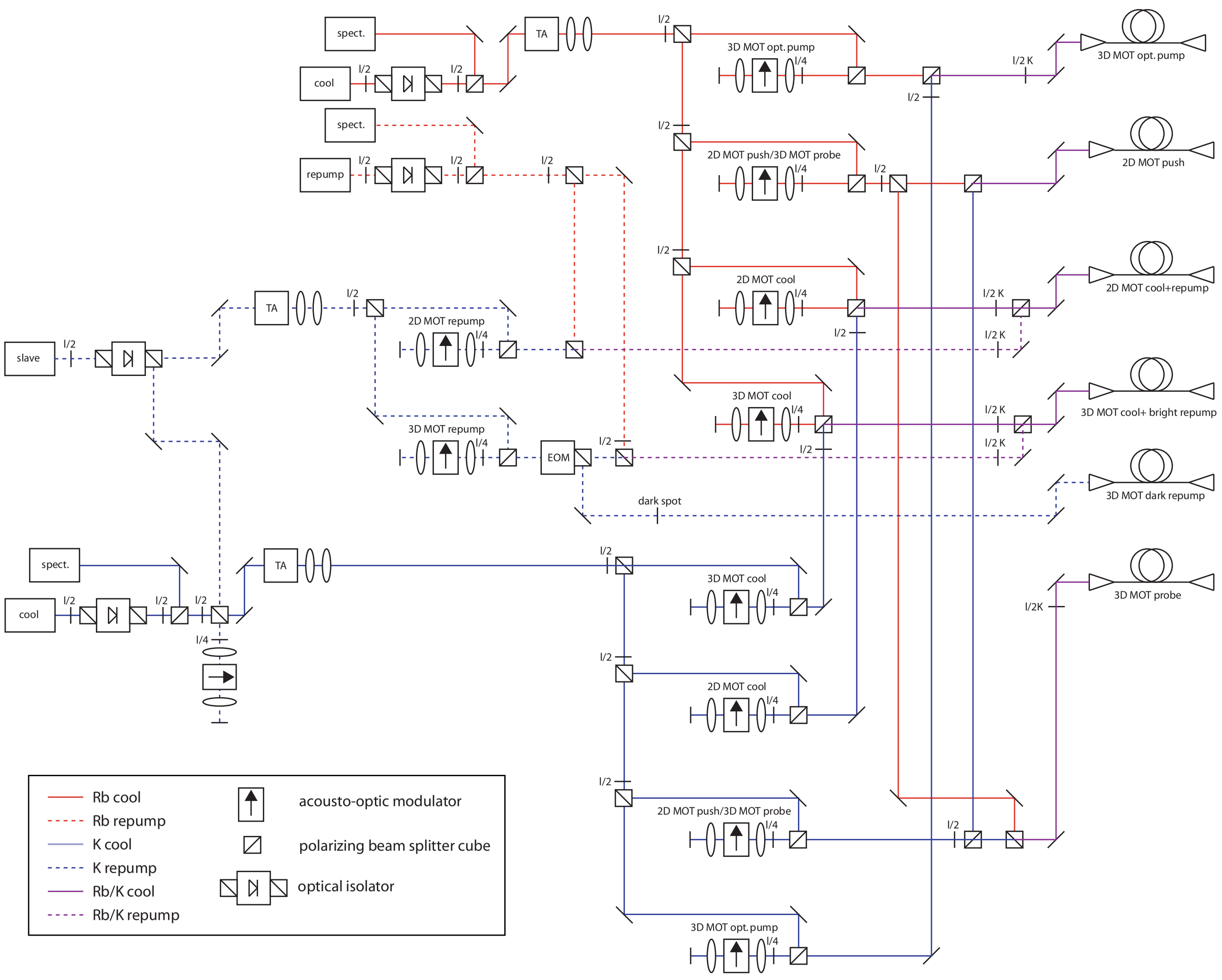

Figure 6.1: Laser system for cooling, optical pumping and probing a mixture of ^{87}Rb and ^{40}K. Laser beams for application with rubidium are colored red, those for potassium blue and combined beams are colored purple.

6.3 Vacuum system

We chose a two-chamber approach, illustrated in figure 6.2, to separate the low vacuum (10^{-7} mbar) volume of the 2D-MOT source from the high vacuum (10^{-11} mbar) of the main chamber containing the atom chip. This is necessary because potassium will have a higher vapor pressure than rubidium under the planned operating conditions, which would cause increased collisions of the trapped gas with the background gas. The 2D-MOT part is formed by a quartz glass cuvette mounted under a four-way cross piece. The latter provides optical access for atom beam characterization as well as ports for a 5 l/s ion pump and current feedthroughs for powering the dispensers containing ^{87}Rb and enriched ^{40}K. A gate valve between the 2D-MOT part and the underside of the main chamber allows for rapid exchange of empty dispensers without affecting the high vacuum. The 2D-MOT works such that both species are simultaneously and transversely laser-cooled and pushed through an aperture, thereby forming an intense beam of slow ($10 - 20$ m/s) atoms [137, 138, 139, 101]. The aperture between the two chambers has a diameter of 1 mm and a length of 12 mm, resulting in a pumping resistance of 100 s/l. These dimensions ensure that the pressure on the high vacuum side is not limited by differential pumping. Additionally the aperture restricts the opening angle of the atomic beam to 40 mrad, matching the size of the mirror-MOT trapping volume. Close couplers between vacuum components are used to minimize the distance from the 2D-MOT capture region to the mirror-MOT.

A spherical octagon with eight CF40 flanges and two CF100 viewports on the outside serves as main chamber. It is extended by a tube to allow for large conductance connection of a 75 l/s ion pump, a turbo-molecular pump and a titanium sublimation pump. The atom chip is mounted from the top on a water-cooled copper block and is positioned 1 cm above the center of the octagon. The other two top flanges are used for a vacuum gauge and current feedthroughs. Three sets of water-cooled coils around the main chamber generate the field for the mirror-MOT and bias fields with arbitrary direction for magnetic traps. The main chamber is surrounded by three sets of coils, generating the magnetic fields for the mirror-MOT, compensation of the earth's magnetic field and bias fields in arbitrary direction for magnetic trapping. For improved clarity, only two of the pairs of coils are shown in figure 6.2. A third pair is mounted on the front side CF100 flange and around the extended tube.

6.4 Conveyor belt atom chip

The double layer atom chip design, depicted in figure 6.3, is formed by a silver foil with milled wire patterns [140] and a nano-fabricated science chip glued on top. The dimensions of the silver foil are $62 \times 30 \times 0.25$ mm. A 2 mm thick Macor substrate is epoxied between the silver foil and a water-cooled copper block for electric isolation. A "U"- and a "Z"-wire with a 4 mm long central section followed by a meandering conveyor belt pattern are milled into the silver foil, which also acts as the reflective surface of the mirror-MOT. The wires are 500 μm wide and separated by 150 μm, the minimum groove size. They support a current of up to 20 A. At $z = 2$ mm distance from the chip surface the "U"-

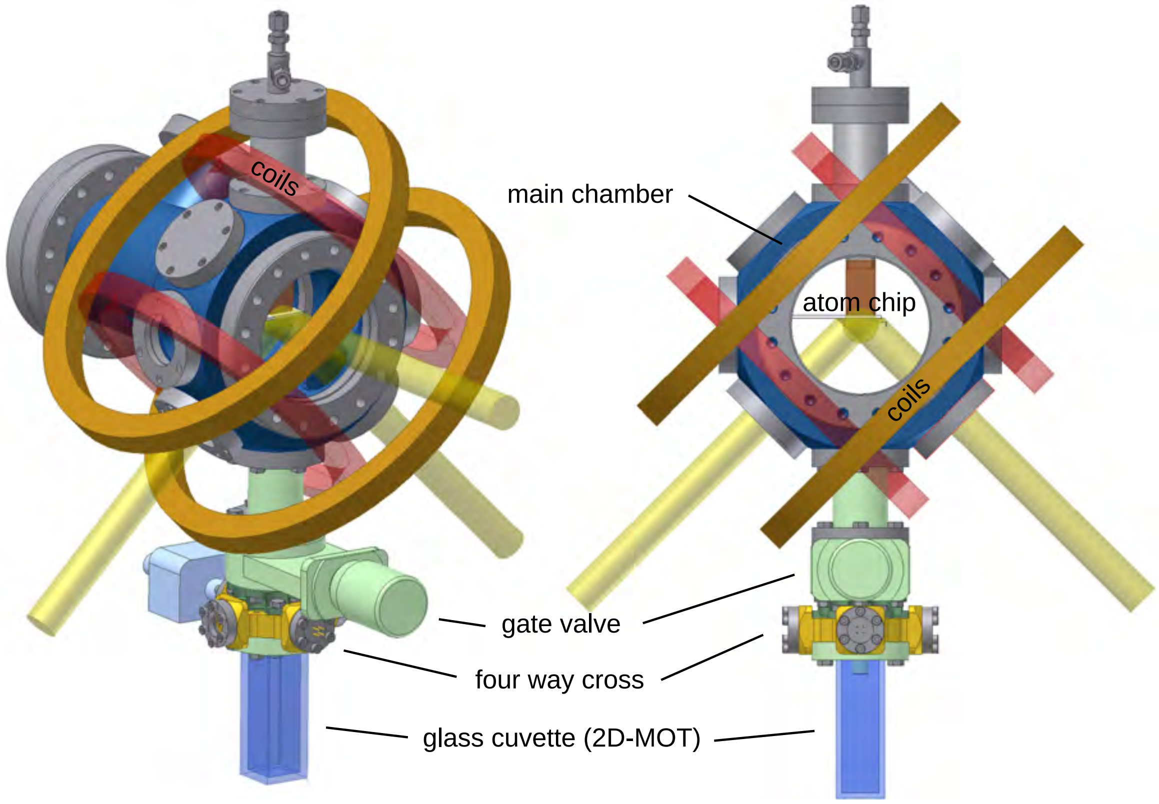

Figure 6.2: Two views of the double chamber vacuum system. The atom chip is mounted into the spherical octagon vacuum chamber via its top port. A gate valve is connecting the bottom of the chamber to a glass cuvette, which forms part of the 2D-MOT. Two pairs of coils for magnetic field generation are depicted in brown and red. The laser beams of the mirror MOT are colored yellow.

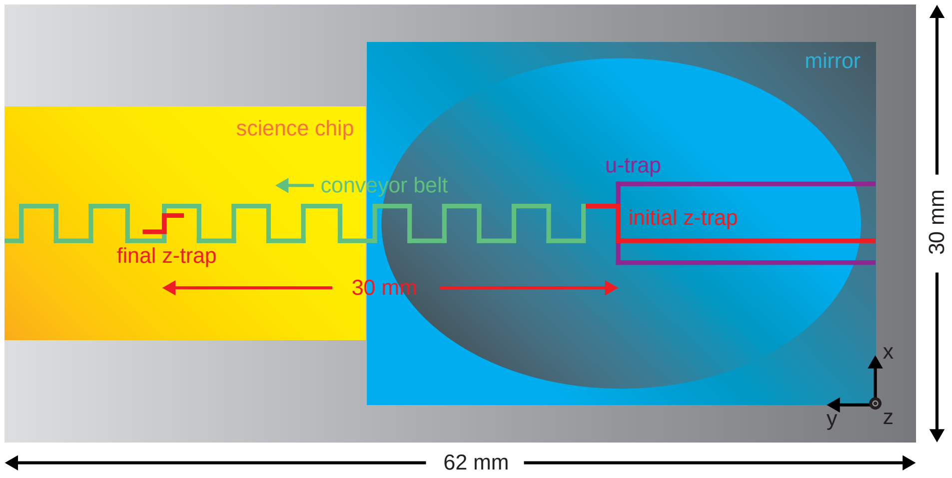

Figure 6.3: Double layer atom chip design. The blue rectangle symbolizes the part of the silver foil which is used as a mirror for the magneto-optical trap. The ellipse therein is the area illuminated by the two laser beams entering the chamber at an angle of 45 °. The conveyor belt is located under the science chip.

trap, when operated at 15 A, yields a trap with a magnetic field gradient of $16, 57, 45\,\mathrm{G/cm}$ in x,y,z-direction, where the x-axis is parallel to the central wire and the z-axis points in the direction of gravity. For a current of 20 A the "Z"-trap produces a gradient of $1200, 1200, 19\,\mathrm{G/cm}$ at $z = 0.5\,\mathrm{mm}$ with a trap depth of 58 G, or correspondingly 3.8 mK. For calibration purposes, quantum degeneracy can already be achieved in this trap. By multiple rotations of the bias field in the y-z-plane, the trap minimum can be shifted as far as 3 cm along the conveyor belt [73] to a final position below the science chip. In this manner the capture region is separated from the science region, enabling good optical access along the x- and the y-axis. Even in-vacuum lenses for maximum numerical aperture are an option in this setup.

6.5 Experiment cycle time

With background loading replaced by loading from the clean, intense and rapidly switchable atomic beam output from the 2D-MOT, the loading time is reduced to approximately 2 s and the vacuum lifetime in the main chamber will be significantly increased. The large area mirror allows for a bigger capture volume and thereby a higher initial number of trapped atoms. This guarantees an improved robustness against number fluctuations induced by electronic and acoustic noise. After the mirror-MOT and optical pumping stages, we anticipate the atoms can be transferred into the "U"- and the "Z"- trap and finally moved below the science chip within 1 sec. At this position, the atoms are taken over by the "Z"-trap of the science chip, marked as final "Z"-trap in figure 6.3. Another second is needed for the final evaporative cooling of Rb and sympathetic cooling of K, before reaching a degenerate Bose-Fermi mixture. The overall cycle time can be as short as 5 s. Furthermore this design facilitates future science chips which could incorporate multiple, individually addressable trap geometries.

6.6 Concluding remarks

A major guideline to the presented design has been minimizing the time before first experiments can be performed. Where possible, the setup is based on readily available components, reducing the need for home-built parts. In a first step, an already existing compatible atom chip will be glued onto a milled silver substrate to from a double-layer chip. First tests with milling grooves into the silver substrate to create the desired wire pattern were undertaken successfully. The existing CELSIUS setup (see chapter 3) was used for experiments with ^{87}Rb alone. In comparison, besides the increased experimental possibilities provided through the added second species, the KELVIN setup offers improvements in many regards.

The two-chamber approach separates the atom source from the capture region. This not only speeds up the loading of atoms in the MOT as pointed out in section 6.5, but also avoids contamination of volume the experiments are conducted in. This will greatly enhance the lifetime of trapped atoms. As already mentioned, the time needed to perform a single experiment will be reduced by approximately a factor of two, leading to a higher temporal stability during the operation of the experiment. By using a smaller main chamber and bigger windows, the optical access will be improved. Separating the capture region from the science region below the double layer atom chip serves the same purpose. Together, these two improvements will make possible a higher numerical aperture in the imaging system, resulting in a better optical resolution.

At the time of writing all components for the optical setup (figure 6.1) and the vacuum apparatus (figure 6.2) have been either ordered or manufactured. The new atom chip design is yet to be implemented.

Chapter A

Experimental sequence for two-component 1D Bose gas

The purpose of this appendix is to provide a more detailed description of the experimental program used to obtain the main results of this thesis, specifically for chapter 5. The first part of this procedure, from starting by cooling atoms in a magneto-optical trap, via loading and compressing a purely magnetic trap to finally generating a 1D Bose-Einstein condensate, is explained in [90] . Here, we focus on the additions and changes made to create a two-component Bose gas, state-selective potentials using radio frequency fields and to image atoms state-selectively.

The initial part of the experimental procedure is very similar to that described in [90] to achieve a BEC in this setup. To test proper operation of the setup we measure the number of atoms in the condensate. This number is typically $N = 45000$, in a Ioffe-Pritchard type static magnetic trap created with the broad "Z"-wire (see chapter 3.1.3) and miniwire two. The trap, formed by running currents of 1.055 A through the "Z"-wire and 3 A through miniwire two, has trap frequencies $\omega_x = 48\,\text{Hz}$ and $\omega_{y,z} = 1060\,\text{Hz}$. The final evaporation frequency is 2.3 MHz. . With this test sequence checked, we take out the final evaporation stage to BEC, and instead ramp down the evaporation radio-frequency to a value that is $\sim 100\,\text{kHz}$ higher than the value needed to reach BEC.

In what follows we go through the essentials of the subsequent steps in the sequence used for the experiments of chapters 5 and 4 (the latter with modifications detailed in chapter 4.2). These steps are illustrated by specific lines in the so-called "time frame", a text file that is interpreted by the experiment control computer running LabView, as described in more detail in [113].

The tables in this appendix show the key parts of the actual time frame. Each line of the time frame contains a waiting time before a device is set to the specified value. Depending on the device, a value can be set instantaneously or continuously ramped within a specified time. Different ramp types can be pre-programmed: "ramp" followed by a number is a linear ramp, where the number encodes the time resolution. "DDSramp" is a linear ramp optimized for use with the direct digital synthesis (DDS) boards we use to generate radio frequencies (see chapter 3.1.4) for evaporative cooling and RF dressing (see chapter 5). Lines starting with "External parameter" attribute a value to a variable.

Table A.1 shows how DDS channels 3 and 4 are set to output the same frequency. Even though only one of the two channels might has a non-zero output amplitude at this time, it was found necessary to program their frequencies to be the same at all times. This ensures a stable relative phase of the two RF signals during later stages of RF dressing.

At this stage, the trapped atoms are still in the $|F = 2, m_f = 2\rangle$ state. As mentioned in

comment	time [ms]	device	value	unit	ramp type	ramp time [ms]
hold	s9+25	DDS 3 freq	f0+1	MHz	DDSramp	10
sync dds	0	DDS 4 freq	f0+1	MHz	DDSramp	10

Table A.1: Synchronizing DDS channels 3 and 4

comment	time [ms]	device	value	unit	ramp type
mix spins	External	parameter	0.008		m1
	10	DDS 3 freq	2.22	MHz	step
sync dds	0	DDS 4 freq	2.22	MHz	step
	0.1	DDS 3 ampl	0.675	mA	step
	m1	DDS 3 ampl	0	mA	step

Table A.2: Transfer from the $|2,2\rangle$ state to the $|2,2\rangle$ state of ^{87}Rb

chapter 4.2, we transfer about 20000 atoms to the $|2\rangle = |F = 2, m_f = 1\rangle$ state with a 8 μs RF pulse resonant with the level splitting of the $F = 2$ state (see table A.2).

Next, by using the two-photon transition illustrated in figure 2.1, we coherently transfer the atoms from the $|2\rangle$ state to the $|1\rangle$ state with almost 100 % efficiency. Table A.3 shows the code used to perform this transfer. To prevent the intermediate state $|F = 2, m_f = 0\rangle$ from being populated, we detune the microwave about 1 MHz away from this transition. Since it takes some time for the microwave generator to lock onto a newly programmed frequency (via radio frequency channel DDS 1, see also chapter 3.2), a delay time is introduced. By using a negative relative time, the command is moved backwards in the time sequence. This assures a stable microwave frequency by the time the pulse is switched on.

Subsequently, the magnetic trapping potential is tightened by increasing the current in the z-shaped chip wire and in the coils generating the bias field in the y-direction. This causes a higher collision rate and therefore facilitates the following last step of evaporative cooling to degeneracy. The details of this step are listed in table A.4. While cooling atoms in state $|1\rangle$, remaining atoms in state $|F = 2, m_f = 2\rangle$ are removed by coupling to the untrapped $|F = 1, m_f = 0\rangle$ state by means of a constant microwave pulse combined with a RF sweep. Due to the change of the magnetic potential, microwave detuning and RF frequencies have slightly changed with respect to earlier stages of the procedure. After evaporative cooling for 620 ms we achieve condensation with a gas of typically 13000 atoms in state $|1\rangle$. A variable waiting time is inserted to reduce the number of atoms by three-body collisions and collisions with the background gas. This is needed to reach the low densities required by the 1D condition (2.22).

comment	time [ms]	device	value	unit	ramp type
quarter cycle time	External	parameter	0.25		m6
mw detuning	External	parameter	-1005.5		d0
conversion kHz to MHz	External	parameter	d0/1000		d1
rf amplitude (two photon)	External	parameter	2		k7
mw programming delay	External	parameter	8.5		l8
	-l8	DDS 1 freq	22.6586945-d1/2	MHz	step
mw pulse	l8	microwave	high	TTL	
rf pulse	0	DDS 3 freq	1	MHz	step
sync dds	0	DDS 4 freq	1	MHz	step
	0	DDS 3 ampl	k7	mA	step
	m6*2	microwave	low	TTL	
	0	DDS 3 ampl	0	mA	step

Table A.3: Combined radio-frequency and microwave pulse to coherently transfer from state $|2\rangle$ to state $|1\rangle$

comment	time [ms]	device	value	unit	ramp type	ramp time [ms]
mw detuning	External	parameter	-1006.2		d3	
conversion kHz to MHz	External	parameter	d3/1000		d4	
initial rf evap freq	External	parameter	2.55		r4	
final rf evap freq	External	parameter	2.283		r5	
evap time	External	parameter	620		x7	
initial rf F=2	0	DDS 2 freq	5.7	MHz	step	
evaporative cooling 2	0	DDS 3 freq	r4	MHz	step	
sync dds	0	DDS 4 freq	r4	MHz	step	
	0	DDS 3 ampl	0.12	mA	step	
	0	DDS 2 ampl	4.0	mA	step	
	0.1	DDS 3 freq	r5	MHz	DDSramp	x7
sync dds	0	DDS 4 freq	r5	MHz	DDSramp	x7
final rf F=2	0	DDS 2 freq	5.5	MHz	DDSramp	x7
mw to remove mf=2	0	DDS 1 freq	22.6586945-d4/2	MHz	step	
	0	microwave	high	TTL		
	x7	microwave	low	TTL		
	0	DDS 2 ampl	0	mA	step	
wait to remove atoms	75	DDS 3 ampl	0	mA	step	

Table A.4: Final stage of evaporative cooling

comment	time [ms]	device	value	unit	ramp type	ramp time [ms]
rf ampl	External	parameter	1		a7	
ramp time	External	parameter	2		h9	
dressing freq	External	parameter	2.16		f9	
rel. phase	External	parameter	304		p7	
offset	0	DDS 3 phase	p7	deg	step	
	0	DDS 4 phase	0	deg	step	
	0	DDS 3 freq	f9	MHz	step	
	0	DDS 4 freq	f9	MHz	step	
	1	DDS 3 ampl	a7/1.0673	mA	ramp	h9
	0	DDS 4 ampl	a7	mA	ramp	h9

Table A.5: Switching on radio-frequency dressing

A final transfer pulse (like the one described in table A.3) mixes the - now degenerate - population of states $|1\rangle$ and $|2\rangle$. Rabi cycles of this transition are shown in figure 5.1. After creating an even mixture of the two states, we turn on the RF dressing (see table A.5) by simultaneously increasing the RF current through chip wires on both sides of the trapping z-wire. The current originating from DDS channel 3 needs to be attenuated by a small empirically determined factor in order to achieve equal RF amplitudes at the position of the trapped gas.

Lastly, we take separate absorption images of atoms in both states of the two-component Bose gas. To illustrate the way the state-selective imaging is performed, we provide three tables: Firstly, imaging of state $|2\rangle$ is shown in table A.6 with lines irrelevant for imaging this state omitted. Secondly, table A.7 demonstrates the procedure used for state $|1\rangle$, containing two additional stages. Finally, tableA.8 shows how a single variable controls which state is imaged. Each time a time frame is executed, the parameter $f1$ is set to either 0 or 1, to image state $|1\rangle$ or $|2\rangle$, respectively.

In both cases, state $|1\rangle$ and state $|2\rangle$, the intensity of the probe laser pulse is controlled via the MOT EOM value, while its frequency is set by MOT AOM. The atom cloud is released from the trap for 1 ms time-of-flight to improve the detection efficiency while preserving the longitudinal distribution. The exposure is controlled by three nested time windows created by the opening and closing of the mechanical probe shutter, the MOT EOM (9.4 V corresponds to closed) and the camera trigger, where TTL low triggers the camera. After the state-selective part of the imaging procedure explained below, an absorption image (using the $F = 2, F' = 3$ transition), a light image and a dark image are taken, each with an exposure time of 30 μs and a delay of 35 ms in between exposures.

As already mentioned, probing atoms in state $|1\rangle$ requires two extra steps before the actual exposure. First atoms in state $|2\rangle$ are removed with a 2 ms resonant light pulse (see table A.7). This is followed by a second step, in which a 0.7 ms repumping pulse from $F = 1$ to $F = 2$ is applied. After this, the atoms are imaged in the same way as atoms in state $|2\rangle$.

comment	time [ms]	device	value	unit	ramp type
prepare probe	External	parameter	6		i8
	0	MOT AOM	6.5	V	step
	0	MOT EOM	i8	V	step
...					
time of flight	1	Probe shutter	open	TTL	
1st trigger	1.2	Camera trigger	low	TTL	
	0	MOT EOM	i8	V	step
	1	Camera trigger	high	TTL	
	0	MOT EOM	9.4	V	step
	5	Probe shutter	shut	TTL	

Table A.6: Imaging of atoms in state $|2\rangle$

comment	time [ms]	device	value	unit	ramp type
prepare probe	External	parameter	6		i8
	0	MOT AOM	6.3	V	step
	0	MOT EOM	i8	V	step
...					
blow away F=2	-2	Probe shutter	open	TTL	
	0	MOT EOM	2	V	step
	2	MOT EOM	9.4	V	step
	0	Probe shutter	shut	TTL	
	External	parameter	0.7		x1
time of flight	1	Probe shutter	open	TTL	
	-x1	Repump shutter	open	TTL	
repump F=1 to F=2	0	MOT EOM	9.4	V	step
	0	Repump EOM	0	V	step
1st trigger	1.2+x1	Camera trigger	low	TTL	
	0	MOT EOM	i8	V	step
	1	Camera trigger	high	TTL	
	0	MOT EOM	9.4	V	step
	5	Probe shutter	shut	TTL	

Table A.7: Imaging of atoms in state $|1\rangle$

comment	time [ms]	device	value	unit	ramp type
image (F=1/F=2)=(0/1)	External	parameter	0		f1
prepare probe	External	parameter	6		i8
	0	MOT AOM	6.3*(1-f1)+6.5*f1	V	step
	0	MOT EOM	i8	V	step
...					
blow away F=2	-2+5*f1	Probe shutter	open	TTL	
	-5*f1	MOT EOM	2	V	step
	2	MOT EOM	9.4	V	step
	0	Probe shutter	shut	TTL	
	External	parameter	0.7		x1
time of flight	1	Probe shutter	open	TTL	
open for F=1 only	-x1+5*f1	Repump shutter	open	TTL	
repump for F=1	-5*f1	MOT EOM	9.4	V	step
	0	Repump EOM	0	V	step
1st trigger	1.2+x1	Camera trigger	low	TTL	
	0	MOT EOM	i8	V	step
	1	Camera trigger	high	TTL	
	0	MOT EOM	9.4	V	step
	5	Probe shutter	shut	TTL	

Table A.8: State-selective imaging of atoms

Bibliography

[1] A. Einstein. Quantentheorie des einatomigen idealen Gases. *Sitzungsberichte der Preussischen Akademie der Wissenschaften zu Berlin*, pages 261–267, 1924.

[2] A. Einstein. Quantentheorie des einatomigen idealen Gases II. *Sitzungsberichte der Preussischen Akademie der Wissenschaften zu Berlin*, pages 3–14, 1925.

[3] A. Einstein. Zur Quantentheorie des idealen Gases. *Sitzungsberichte der Preussischen Akademie der Wissenschaften zu Berlin*, pages 18–25, 1925.

[4] S.N. Bose. Plancks Gesetz und Lichtquantenhypothese. *Z. Phys.*, 26:178, 1924.

[5] M. H. Anderson, J. R. Ensher, M. R. Matthews, C. E. Wieman, and E. A. Cornell. Observation of Bose-Einstein Condensation in a Dilute Atomic Vapor. *Science*, 269:198–201, July 1995.

[6] K. B. Davis, M. O. Mewes, M. R. Andrews, N. J. van Druten, D. S. Durfee, D. M. Kurn, and W. Ketterle. Bose-Einstein Condensation in a Gas of Sodium Atoms. *Phys. Rev. Lett.*, 75(22):3969–3973, Nov 1995.

[7] C. C. Bradley, C. A. Sackett, J. J. Tollett, and R. G. Hulet. Evidence for Bose-Einstein Condensation in an Atomic Gas with Attractive Interactions. *Phys. Rev. Lett.*, 75(9):1687–1690, 1995.

[8] Immanuel Bloch, Jean Dalibard, and Wilhelm Zwerger. Many-body physics with ultracold gases. *Rev. Mod. Phys.*, 80:885–964, 2008.

[9] UltraCold Atom News - Research Groups.

[10] B. DeMarco and D. S. Jin. Onset of Fermi Degeneracy in a Trapped Atomic Gas. *Science*, 285(5434):1703–1706, 1999.

[11] G. Modugno, G. Ferrari, G. Roati, R. J. Brecha, A. Simoni, and M. Inguscio. Bose-Einstein Condensation of Potassium Atoms by Sympathetic Cooling. *Science*, 294:1320, 2001.

[12] Giovanni Modugno, Giacomo Roati, Francesco Riboli, Francesca Ferlaino, Robert J. Brecha, and Massimo Inguscio. Collapse of a Degenerate Fermi Gas. *Science*, 26:2240–2243, 2002.

[13] Michael Köhl, Henning Moritz, Thilo Stöferle, Kenneth Günter, and Tilman Esslinger. Fermionic Atoms in a Three Dimensional Optical Lattice: Observing Fermi Surfaces, Dynamics, and Interactions. *Phys. Rev. Lett.*, 94:080403, 2005.

[14] Giovanni Modugno. Fermi-Bose mixture with tunable interactions. *arXiv*, cond-mat:0702277, 2007.

[15] C. Ospelkaus, S. Ospelkaus, K. Sengstock, and K. Bongs. Interaction-Driven Dynamics of 40K-87Rb Fermion-Boson Gas Mixtures in the Large-Particle-Number Limit. *Phys. Rev. Lett.*, 96:020401, 2006.

[16] C. Ospelkaus and S. Ospelkaus. Heteronuclear quantum gas mixtures. *J. Phys. B: At. Mol. Opt. Phys.*, 41:203001, 2008.

[17] Cheng Chin, Rudolf Grimm, Paul Julienne, and Eite Tiesinga. Feshbach resonances in ultracold gases. *Rev. Mod. Phys.*, 82:1225–1286, 2010.

[18] C. A. Regal, M. Greiner, and D. S. Jin. Observation of Resonance Condensation of Fermionic Atom Pairs. *Phys. Rev. Lett.*, 92:040403, 2004.

[19] M. Bartenstein, A. Altmeyer, S. Riedl, S. Jochim, C. Chin, J. Hecker Denschlag, and R. Grimm. Crossover from a Molecular Bose-Einstein Condensate to a Degenerate Fermi Gas. *Phys. Rev. Lett.*, 92:120401, 2004.

[20] M. W. Zwierlein, C. A. Stan, C. H. Schunck, S. M. F. Raupach, A. J. Kerman, and W. Ketterle. Condensation of Pairs of Fermionic Atoms near a Feshbach Resonance. *Phys. Rev. Lett.*, 92:120403, 2004.

[21] Axel Griesmaier, Jörg Werner, Sven Hensler, Jürgen Stuhler, and Tilman Pfau. Bose-Einstein Condensation of Chromium. *Phys. Rev. Lett.*, 94:160401, 2005.

[22] B. Pasquiou, G. Bismut, E. Maréchal, P. Pedri, L. Vernac, O. Gorceix, and B. Laburthe-Tolra. Spin relaxation and band excitation of a dipolar Bose-Einstein condensate in 2D optical lattices. *Phys. Rev. Lett.*, 106:015301, 2011.

[23] Daniel Comparat and Pierre Pillet. Dipole blockade in a cold Rydberg atomic sample. *J. Opt. Soc. Am. B*, 27:A208–A232, 2010.

[24] M. Saffman, T. G. Walker, and K. Mølmer. Quantum information with Rydberg atoms. *Rev. Mod. Phys.*, 82:2313–2363, 2010.

[25] J. Stenger, S. Inouye, D. M. Stamper-Kurn, H.-J. Miesner, A. P. Chikkatur, and W. Ketterle. Spin domains in ground-state Bose-Einstein condensates. *Nature*, 396:345, 1998.

[26] H. Schmaljohann, M. Erhard, J. Kronjäger, M. Kottke, S. van Staa, L. Cacciapuoti, J. J. Arlt, K. Bongs, and K. Sengstock. Dynamics of F=2 spinor Bose-Einstein condensates. *Phys. Rev. Lett.*, 92:040402, 2004.

[27] J. N. Fuchs, D. M. Gangardt, T. Keilmann, and G. V. Shlyapnikov. Spin Waves in a One-Dimensional Spinor Bose Gas. *Phys. Rev. Lett.*, 95:150402, 2005.

[28] M. B. Zvonarev, V. V. Cheianov, and T. Giamarchi. Spin dynamics in a one-dimensional ferromagnetic Bose gas. *Phys. Rev. Lett.*, 99:240404, 2007.

[29] A. Kleine, C. Kollath, I. P. McCulloch, T. Giamarchi, and U. Schollwöck. Spin-charge separation in two-component Bose gases. *Phys. Rev. A*, 77:013607, 2008.

[30] A. Widera, S. Trotzky, P. Cheinet, S. Fölling, F. Gerbier, I. Bloch, V. Gritsev, M. D. Lukin, and E. Demler. Quantum Spin Dynamics of Mode-Squeezed Luttinger Liquids in Two-Component Atomic Gases. *Phys. Rev. Lett.*, 100:140401, 2008.

[31] Jochen Kronjäger, Christoph Becker, Parvis Soltan-Panahi, Kai Bongs, and Klaus Sengstock. Spontaneous Pattern Formation in an Antiferromagnetic Quantum Gas. *Phys. Rev. Lett.*, 105(9):090402, Aug 2010.

[32] M. Vengalattore, J. Guzman, S. R. Leslie, F. Servane, and D. M. Stamper-Kurn. Periodic spin textures in a degenerate F=1 ^{87}Rb spinor Bose gas. *Phys. Rev. A*, 81:053612, 2010.

[33] Y.-A. Liao, Ann Sophie C. Rittner, Tobias Paprotta, Wenhui Li, Guthrie B. Partridge, Randall G. Hulet, Stefan K. Baur, and Erich J. Mueller. Spin-imbalance in a one-dimensional Fermi gas. *Nature*, 467:567–569, 2010.

[34] M. Olshanii. Atomic Scattering in the Presence of an External Confinement and a Gas of Impenetrable Bosons. *Phys. Rev. Lett.*, 81:938, 1998.

[35] D. S. Petrov, G. V. Shlyapnikov, and J. T. M. Walraven. Regimes of quantum degeneracy in trapped 1D gases. *Phys. Rev. Lett.*, 85:3745, 2000.

[36] A. Recati, P. O. Fedichev, W. Zwerger, and P. Zoller. Spin-Charge Separation in Ultracold Quantum Gases. *Phys. Rev. Lett.*, 90:020401, 2003.

[37] K. V. Kheruntsyan, D. M. Gangardt, P. D. Drummond, and G. V. Shlyapnikov. Pair Correlations in a Finite-Temperature 1D Bose Gas. *Phys. Rev. Lett.*, 91:040403, 2003.

[38] Toshiya Kinoshita, Trevor Wenger, and David S. Weiss. Observation of a One-Dimensional Tonks-Girardeau Gas. *Science*, 305:1125–1128, 2004.

[39] B. Paredes, A. Widera, V. Murg, O. Mandel, S. Fölling, I. Cirac, G. V. Shlyapnikov, T. W. Hänsch, and I. Bloch. Tonks-Girardeau gas of ultracold atoms in an optical lattice. *Nature*, 429:277–281, 2004.

[40] S. Hofferberth, I. Lesanovsky, T. Schumm, A. Imambekov, V. Gritsev, E. Demler, and J. Schmiedmayer. Probing quantum and thermal noise in an interacting many-body system. *Nature Phys.*, 4:489–495, 2008.

[41] A. H. van Amerongen, J. J. P. van Es, P. Wicke, K. V. Kheruntsyan, and N. J. van Druten. Yang-Yang thermodynamics on an atom chip. *Phys. Rev. Lett.*, 100:090402, 2008.

[42] D. S. Petrov, D. M. Gangardt, and G. V. Shlyapnikov. Low-dimensional trapped gases. *J. Phys. IV (France)*, 116:5, 2004.

[43] E. H. Lieb and W. Liniger. Exact Analysis of an Interacting Bose Gas. I. The General Solution and the Ground State. *Phys. Rev.*, 130:1605, 1963.

[44] C. N. Yang and C. P. Yang. Thermodynamics of a One-Dimensional System of Bosons with Repulsive Delta-Function Interaction. *J. Math. Phys.*, 10:1115, 1969.

[45] V. E. Korepin, N. M. Bogoliubov, and A. G. Izergin. *Quantum Inverse Scattering Method and Correlation Functions.* Cambridge University Press, Cambridge, England, 1993.

[46] Minoru Takahashi. *Thermodynamics of One-Dimensional Solvable Models.* Cambridge University Press, Cambridge, England, 1999.

[47] Jean-Sébastien Caux, Antoine Klauser, and Jeroen van den Brink. Polarization suppression and nonmonotonic local two-body correlations in the two-component Bose gas in one dimension. *Phys. Rev. A*, 80:061605(R), 2009.

[48] Toshiya Kinoshita, Trevor Wenger, and David S. Weiss. Local Pair Correlations in One-Dimensional Bose Gases. *Phys. Rev. Lett.*, 95(19):190406, 2005.

[49] E. Haller, M. Gustavsson, M. J. Mark, J. G. Danzl, R. Hart, G. Pupillo, and H-C. Nägerl. Realization of an excited, strongly correlated quantum gas phase. *Science*, 325:1224, 2009.

[50] E. Haller, M. J. Mark, R. Hart, J. G. Danzl, L. Reichsöllner, V. Melezhik, P. Schmelcher, and H-C. Nägerl. Confinement-induced resonances in low-dimensional quantum systems. *Phys. Rev. Lett.*, 104:153203, 2010.

[51] S. Hofferberth, I. Lesanovsky, B. Fischer, T. Schumm, and J. Schmiedmayer. Non-equilibrium coherence dynamics in one-dimensional Bose gases. *Nature*, 449:324, 2007.

[52] H. Pichler, A. J. Daley, and P. Zoller. Nonequilibrium dynamics of bosonic atoms in optical lattices: Decoherence of many-body states due to spontaneous emission. *Phys. Rev. A*, 82:063605, 2010.

[53] David P. DiVincenzo. The Physical Implementation of Quantum Computation. *Fortschritte der Physik*, 48:711–783, 2000.

[54] P. S. Jessen, I. H. Deutsch, and R. Stock. Quantum Information Processing with Trapped Neutral Atoms. *Quantum Information Processing*, 3:15–27, 2004.

[55] D. Jaksch and P. Zoller. The cold atom Hubbard toolbox. *Annals of Physics*, 315:52–79, 2005.

[56] V. Y. F. Leung, A. Tauschinsky, N. J. van Druten, and R. J. C. Spreeuw. Microtrap arrays on magnetic film atom chips for quantum information science. *Quantum Information Processing*, 6:955–974, 2011.

[57] S. Wildermuth, S. Hofferberth, I. Lesanovsky, S. Groth, P. Krüger, J. Schmiedmayer, and I. Bar-Joseph. Sensing electric and magnetic fields with Bose-Einstein condensates. *Appl. Phys. Lett.*, 88:264103, 2006.

[58] B. Canuel, F. Leduc, D. Holleville, A. Gauguet, J. Fils, A. Virdis, A. Clairon, N. Dimarcq, Ch. J. Bordé, and A. Landragin. Six-Axis Inertial Sensor Using Cold-Atom Interferometry. *Phys. Rev. Lett.*, 97:010402, 2006.

[59] A. Lenef, T. D. Hammond, E. T. Smith, M. S. Chapman, R. A. Rubenstein, and D. E. Pritchard. Rotation Sensing with an Atom Interferometer. *Phys. Rev. Lett.*, 78(5):760–763, 1997.

[60] Gretchen K. Campbell and William D. Phillips. Ultracold atoms and precise time standards. *Phil. Trans. R. Soc. Lond. A*, 369:4078–4089, 2011.

[61] M. F. Riedel, P. Böhi, Y. Li, T. W. Hänsch, A. Sinatra, and P. Treutlein. Atom-chip-based generation of entanglement for quantum metrology. *Nature*, 464:1170–1173, 2010.

[62] C. Gross, T. Zibold, E. Nicklas, J. Estève, and M. K. Oberthaler. Nonlinear atom interferometer surpasses classical precision limit. *Nature*, 464:1165–1169, 2010.

[63] I. Bloch. Ultracold quantum gases in optical lattices. *Nature Phys.*, 1:23–30, 2005.

[64] D. Jaksch, C. Bruder, J. I. Cirac, C. W. Gardiner, and P. Zoller. Cold Bosonic Atoms in Optical Lattices. *Phys. Rev. Lett.*, 81:3108–3111, 1998.

[65] M. Greiner, O. Mandel, T. Esslinger, T. W. Hänsch, and I. Bloch. Quantum phase transition from a superfluid to a Mott insulator in a gas of ultracold atoms. *Nature*, 415:39–44, 2002.

[66] W. Hofstetter, J. I. Cirac, P. Zoller, E. Demler, and M. D. Lukin. High-Temperature Superfluidity of Fermionic Atoms in Optical Lattices. *Phys. Rev. Lett.*, 89:220407, 2002.

[67] O. Mandel, M. Greiner, A. Widera, T. Rom, T. W. Hänsch, and I. Bloch. Controlled collisions for multiparticle entanglement of optically trapped atoms. *Nature*, 425:937–940, 2003.

[68] P. J. Lee, M. Anderlini, B. L. Brown, J. Sebby-Strabley, W. D. Phillips, and J. V. Porto. Sublattice addressing and spin-dependent motion of atoms in a double-well lattice. *Phys. Rev. Lett.*, 99:020402, 2007.

[69] T. Calarco, E. A. Hinds, D. Jaksch, J. Schmiedmayer, J. I. Cirac, and P. Zoller. Quantum gates with neutral atoms: Controlling collisional interactions in time-dependent traps. *Phys. Rev. A*, 61:022304, 2000.

[70] J. Reichel. Microchip traps and Bose-Einstein condensation. *Appl. Phys. B*, 74:469–487, 2002.

[71] J. Fortágh and C. Zimmermann. Magnetic microtraps for ultracold atoms. *Rev. Mod. Phys.*, 79:235, 2007.

[72] J. Reichel and V. Vuletic, editors. *Atom Chips.* Wiley-VCH, 2011.

[73] R. Long, T. Rom, W. Hänsel, T. W. Hänsch, and J. Reichel. Long distance magnetic conveyor for precise positioning of ultracold atoms. *Eur. Phys. J. D*, 35:125–133, 2005.

[74] Akifumi Takamizawa, Tilo Steinmetz, Rémi Delhuille, Theodor W. Hänsch, and Jakob Reichel. Miniature fluorescence detector for single atom observation on a microchip. *Opt. Express*, 14(23):10976–10983, 2006.

[75] Ying-Ju Wang, Dana Z. Anderson, Victor M. Bright, Eric A. Cornell, Quentin Diot, Tetsuo Kishimoto, Mara Prentiss, R. A. Saravanan, Stephen R. Segal, and Saijun Wu. Atom Michelson Interferometer on a Chip Using a Bose-Einstein Condensate. *Phys. Rev. Lett.*, 94:090405, 2005.

[76] T. Schumm, P. Krüger, S. Hofferberth, I. Lesanovsky, S. Wildermuth, S. Groth, I. Bar-Joseph, L. M. Andersson, and J. Schmiedmayer. A Double Well Interferometer on an Atom Chip. *Quantum Information Processing*, 5(6):537–558, 2006.

[77] J.T.M. Walraven. Atomic hydrogen in magnetostatic traps. In G.-L. Oppo, S.M. Barnett, E. Riis, and M. Wilkinson, editors, *Quantum dynamics of symple systems*, volume 44 of *SUSSP Proceedings*, Bristol, 1996. IOP.

[78] Wolfgang Ketterle and N. J. van Druten. Evaporative cooling of trapped atoms. *Advances in Atomic, Molecular and Optical Physics*, 37:181–236, 1996.

[79] O. Zobay and B. M. Garraway. Two-Dimensional Atom Trapping in Field-Induced Adabiatic Potentials. *Phys. Rev. Lett.*, 86:1195–1198, 2001.

[80] I. Lesanovsky, T. Schumm, S. Hofferberth, L. M. Andersson, P. Krüger, and J. Schmiedmayer. Adiabatic radio-frequency potentials for the coherent manipulation of matter waves. *Phys. Rev. A*, 73:033619, 2006.

[81] T. Schumm, S. Hofferberth, L. M. Andersson, S. Wildermuth, S. Groth, I. Bar-Joseph, J. Schmiedmayer, and P. Krüger. Matter-wave interferometry in a double well on an atom chip. *Nature Phys.*, 1:57–62, 2005.

[82] P. Böhi, M. F. Riedel, J. Hoffrogge, J. Reichel, T. W. Hänsch, and P. Treutlein. Coherent manipulation of Bose-Einstein condensates with state-dependent microwave potentials on an atom chip. *Nature Phys.*, 5:592–597, 2009.

[83] Patrick Medley, David M. Weld, Hirokazu Miyake, David E. Pritchard, and Wolfgang Ketterle. Spin gradient demagnetization cooling of ultracold atoms. *arXiv:1006.4674*, 2010.

[84] D. M. Harber, H. J. Lewandowski, J. M. McGuirk, and E. A. Cornell. Effect of cold collisions on spin coherence and resonance shifts in a magnetically trapped ultracold gas. *Phys. Rev. A*, 66:053616, 2002.

[85] K. M. Mertes, J. W. Merrill, R. Carretero-González, D. J. Frantzeskakis, P. G. Kevrekidis, and D. S. Hall. Nonequilibrium Dynamics and Superfluid Ring Excitations in Binary Bose-Einstein Condensates. *Phys. Rev. Lett.*, 99(19):190402, 2007.

[86] R. P. Anderson, C. Ticknor, A. I. Sidorov, and B. V. Hall. Spatially inhomogeneous phase evolution of a two-component Bose-Einstein condensate. *Phys. Rev. A*, 80:023603, 2009.

[87] Y. V. Gott, M. S. Ioffe, and V. G. Telkovskii. Some new results on confinement in magnetic traps. *Nucl. Fusion, Suppl.*, Pt. 3:1045 and 1284, 1962.

[88] David E. Pritchard. Cooling Neutral Atoms in a Magnetic Trap for Precision Spectroscopy. *Phys. Rev. Lett.*, 51(15):1336–1339, 1983.

[89] Jom Luiten. *Lyman-α spectroscopy of magnetically trapped atomic hydrogen.* PhD thesis, Universiteit van Amsterdam, 1993.

[90] A. H. van Amerongen. *One-dimensional Bose gas on an atom chip.* PhD thesis, Universiteit van Amsterdam, 2008.

[91] Claude N. Cohen-Tannoudji. Manipulating atoms with photons. *Rev. Mod. Phys.*, 70:707–719, 1998.

[92] C. Cohen-Tannoudji, J. Dupont-Roc, and G. Grynberg. *Atom-Photon Interactions.* Wiley, New York, 1992.

[93] I. Lesanovsky, S. Hofferberth, J. Schmiedmayer, and P. Schmelcher. Manipulation of ultracold atoms in dressed adiabatic radio-frequency potentials. *Phys. Rev. A*, 74:033619, 2006.

[94] T. Fernholz, R. Gerritsma, P. Krüger, and R. J. C. Spreeuw. Dynamically controlled toroidal and ring-shaped magnetic traps. *Phys. Rev. A*, 75:063406, 2007.

[95] Franco Dalfovo, Stefano Giorgini, Lev P. Pitaevskii, and Sandro Stringari. Theory of Bose-Einstein condensation in trapped gases. *Rev. Mod. Phys.*, 71, 1999.

[96] C.J. Pethick and H. Smith. *Bose-Einstein Condensation in Dilute Gases.* Cambridge University Press, Cambridge, 2002.

[97] D. S. Petrov, G. V. Shlyapnikov, and J. T. M. Walraven. Regimes of Quantum Degeneracy in Trapped 1D Gases. *Phys. Rev. Lett.*, 85:3745–3749, 2000.

[98] M. Egorov, B. Opanchuk, P. Drummond, B.V. Hall, P. Hannaford, and A. I. Sidorov. Precision measurements of s-wave scattering lengths in a two-component Bose-Einstein condensate. *arXiv*, cond-mat:1204.1591v1, 2012.

[99] L. Salasnich, A. Parola, and L. Reatto. Effective wave equations for the dynamics of cigar-shaped and disk-shaped Bose condensates. *Phys. Rev. A*, 65:043614, 2002.

[100] M. Greiner, C. A. Regal, and D. S. Jin. Emergence of a molecular Bose–Einstein condensate from a Fermi gas. *Nature*, 426:537–540, 2003.

[101] Antje Ludewig. *Feshbach Resonances in ^{40}K.* PhD thesis, University of Amsterdam, 2011.

[102] A. Marte, T. Volz, J. Schuster, S. Dürr, G. Rempe, E. G. M. van Kempen, and B. J. Verhaar. Feshbach Resonances in Rubidium 87: Precision Measurement and Analysis. *Phys. Rev. Lett.*, 89:283202, 2002.

[103] M. Erhard, H. Schmaljohann, J. Kronjäger, K. Bongs, and K. Sengstock. Measurement of a mixed-spin-channel Feshbach resonance in ^{87}Rb. *Phys. Rev. A*, 69:032705, 2004.

[104] E. Timmermans. Phase Separation of Bose-Einstein Condensates. *Phys. Rev. Lett.*, 81:5718–5721, 1998.

[105] calculated using code provided by S. Whitlock, 2011.

[106] B. Laburthe Tolra, K. M. O'Hara, J. H. Huckans, W. D. Phillips, S. L. Rolston, and J. V. Porto. Observation of Reduced Three-Body Recombination in a Correlated 1D Degenerate Bose Gas. *Phys. Rev. Lett.*, 92(19):190401, 2004.

[107] J.-B. Trebbia, J. Estève, C. I. Westbrook, and I. Bouchoule. Experimental evidence for the breakdown of a Hartree-Fock approach in a weakly interacting Bose gas. *Phys. Rev. Lett.*, 97:250403, 2006.

[108] J. Estève, J.-B. Trebbia, T. Schumm, A. Aspect, C. I. Westbrook, and I. Bouchoule. Observations of Density Fluctuations in an Elongated Bose Gas: Ideal Gas and Quasicondensate Regimes. *Phys. Rev. Lett.*, 96:130403, 2006.

[109] P. Krüger, L. M. Andersson, S. Wildermuth, S. Hofferberth, E. Haller, S. Aigner, S. Groth, I. Bar-Joseph, and J. Schmiedmayer. Potential roughness near lithographically fabricated atom chips. *Phys. Rev. A*, 76:063621, 2007.

[110] Jakob Reichel and Joseph H. Thywissen. Using magnetic chip traps to study Tonks-Girardeau quantum gases. *J. Phys. IV (France)*, 116:265–274, 2004.

[111] Philipp Treutlein, Peter Hommelhoff, Tilo Steinmetz, Theodor W. Hänsch, and Jakob Reichel. Coherence in Microchip Traps. *Phys. Rev. Lett.*, 92:203005, 2004.

[112] Christof Weitenberg, Manuel Endres, Jacob F. Sherson, Marc Cheneau, Peter Schauß, Takeshi Fukuhara, Immanuel Bloch, and Stefan Kuhr. Single-spin addressing in an atomic Mott insulator. *Nature*, 471:319–324, 2011.

[113] J. J. P. van Es. *Bose-Einstein condensates in radio-frequency-dressed potentials on an atom chip.* PhD thesis, Universiteit van Amsterdam, 2008.

[114] R. W. P. Drever, J. L. Hall, F. V. Kowalski, J. Hough, G. M. Ford, A. J. Munley, and H. Ward. Laser phase and frequency stabilization using an optical resonator. *Appl. Phys. B*, 31(2):97–105, 1983.

[115] Paul Cleary. *in preparation.* PhD thesis, University of Amsterdam, 2012.

[116] S. Whitlock, C. F. Ockeloen, and R. J. C. Spreeuw. Sub-Poissonian Atom-Number Fluctuations by Three-Body Loss in Mesoscopic Ensembles. *Phys. Rev. Lett.*, 104:120402, 2010.

[117] Hewlett-Packard. *Obtaining Millihertz Resolution from the 8671A/8672A*, application note 218-2 edition, 1977.

[118] Sven Dortmund and Gunnar Armbrecht. Funkdosen-Theorie. *c't*, 25:220–222, 2007.

[119] L. Hoendervanger. Introducing an optical lattice to a one-dimensional Bose-Einstein condensate on an atom chip. Master's thesis, Van der Waals-Zeeman Institute / University of Amsterdam, 2010.

[120] J. Reichel, W. Hänsel, and T. W. Hänsch. Atomic Micromanipulation with Magnetic Surface Traps. *Phys. Rev. Lett.*, 83(17):3398–3401, 1999.

[121] J. Armijo, T. Jacqmin, K. Kheruntsyan, and I. Bouchoule. Mapping out the quasi-condensate transition through the 1D-3D dimensional crossover. *Phys. Rev. A*, 83:021605(R), 2011.

[122] I. Bouchoule, N.J. van Druten, and C.I. Westbrook. *Atom Chips and One-Dimensional Bose Gases.* Wiley-VCH, 2011.

[123] P. Wicke, S. Whitlock, and N.J. van Druten. Controlling spin motion and interactions in a one-dimensional Bose gas. *arXiv*, cond-mat:1010.4545, 2010.

[124] S. Hofferberth, I. Lesanovsky, B. Fisher, J. Verdu, and J. Schmiedmayer. Radio-frequency-dressed-state potentials for neutral atoms. *Nature Phys.*, 2:710–716, 2006.

[125] J. J. P. van Es, P. Wicke, A. H. van Amerongen, C. Rètif, S. Whitlock, and N. J. van Druten. Box traps on an atom chip for one-dimensional quantum gases. *J. Phys. B: At. Mol. Opt. Phys.*, 43:155002, 2010.

[126] I. Lesanovsky, T. Schumm, S. Hofferberth, L. M. Andersson, P. Krüger, and J. Schmiedmayer. Adiabatic radio-frequency potentials for the coherent manipulation of matter waves. *Phys. Rev. A*, 73:033619, 2006.

[127] S. Hofferberth, B. Fischer, T. Schumm, J. Schmiedmayer, and I. Lesanovsky. Ultracold atoms in radio-frequency dressed potentials beyond the rotating-wave approximation. *Phys. Rev. A*, 76:013401, 2007.

[128] J. J. P. van Es, S. Whitlock, T. Fernholz, A. H. van Amerongen, and N. J. van Druten. Longitudinal character of atom-chip-based rf-dressed potentials. *Phys. Rev. A*, 77:063623, 2008.

[129] T. Giamarchi. *Quantum physics in one dimension.* Internat. Ser. Mono. Phys. Clarendon Press, Oxford, 2004.

[130] S. Hofferberth, I. Lesanovsky, B. Fischer, T. Schumm, and J. Schmiedmayer. Non-equilibrium coherence dynamics in one-dimensional Bose gases. *Nature*, 449:324, 2007.

[131] A. Couairona and A. Mysyrowicz. Femtosecond filamentation in transparent media. *Phys. Rep.*, 441:47–189, 2007.

[132] C. Deutsch, F. Ramirez-Martinez, C. Lacroûte, F. Reinhard, T. Schneider, J-N. Fuchs, F. Piéchon, F. Laloë, J. Reichel, and P. Rosenbusch. Spin self-rephasing and very long coherence times in a trapped atomic ensemble. *Phys. Rev. Lett.*, 105:020401, 2010.

[133] S. Aubin, S. Myrskog, M. H. T. Extavour, L. J. Leblanc, D. McKey, A. Stummer, and J. H. Thywissen. Rapid sympathetic cooling to Fermi degeneracy on a chip. *Nature Phys.*, 2:384, 2006.

[134] M. H. T. Extavour, L. J. LeBlanc, T. Schumm, B. Cieslak, S. Myrskog, A. Stummer, S. Aubin, and J. H. Thywissen. Dual-species Quantum Degeneracy of ^{40}K and ^{87}Rb on an Atom Chip. In Christian Roos, Hartmut Häffner, and Rainer Blatt, editors, *Atomic Physics 20*, pages 241–249, New York, 2006. AIP Conference Proceedings 869.

[135] Kunal K. Das. Bose-Fermi Mixtures in One Dimension. *Phys. Rev. Lett.*, 90:170403, 2003.

[136] R. A. Nyman, G. Varoquaux, B. Villier, D. Sacchet, F. Moron, Y. Le Coq, A. Aspect, and P. Bouyer. Tapered-amplified antireflection-coated laser diodes for potassium and rubidium atomic-physics experiments. *Rev. Sci. Instr.*, 77:033105, 2006.

[137] K. Dieckmann, R. J. C. Spreeuw, M. Weidemüller, and J. T. M. Walraven. Two-dimensional magneto-optical trap as a source of slow atoms. *Phys. Rev. A*, 58(5):3891–3895, 1998.

[138] Kai Dieckmann. *Bose-Einstein Condensation with High Atom Number in a Deep Magnetic Trap.* PhD thesis, Universiteit van Amsterdam, 2001.

[139] Tobias Tiecke. *Feshbach resonances in ultracold mixtures of the fermionic quantum gases Feshbach resonances in ultracold mixtures of the fermionic quantum gases ^{6}Li and ^{40}K.* PhD thesis, University of Amsterdam, 2009.

[140] C. J. Vale, B. Upcroft, M. J. Davis, N. R. Heckenberg, and H. Rubinsztein-Dunlop. Foil-based atom chip for Bose-Einstein condensates. *J. Phys. B*, 37:2959–2967, 2004.

Summary

When atoms are cooled to temperatures close to absolute zero (about 150 nanokelvin in our case), their quantum statistics become apparent. Depending on whether the total number of constituent protons, neutrons and electrons is even or odd, the atom is a boson or a fermion, respectively. When being trapped and cooled in an external potential, bosons condense into the quantum mechanical ground state and can be treated as a coherent matter wave called a Bose-Einstein condensate (BEC). Fermions on the other hand are subject to the Pauli exclusion principle, which prohibits two identical fermions from occupying the same quantum state. Therefore, in a cold Fermi gas, all quantum states up to a certain energy are occupied by exactly one atom. Most experiments with quantum gases (BECs and Fermi gases) are performed in traps that allow motion in all three dimensions. The focus of this work in on one-dimensional (1D) bosonic quantum gases, in which the atoms are confined such that they can only move along a single direction.

One-dimensional quantum gases feature phenomena not present in their 2D or 3D counterparts. For example, a 1D Bose gas becomes more strongly interacting as the density decreases. Under specific conditions these 1D systems can be described by exactly solvable models, whereas the description of systems with higher dimensionality inherently relies on approximations.

In spinor quantum gases, the atoms can occupy multiple internal states. This offers the opportunity to study the interplay between internal (spin) and external (motion) degrees of freedom. This interplay is important in generally relevant and challenging phenomena such as quantum magnetism.

In our experiments, exclusively performed with a specific, bosonic isotope of rubidium, ^{87}Rb, we create a two-component (spinor) Bose gas in a 1D potential. The states involved are the two clock states of ^{87}Rb that experience the same magnetic trapping potentials. At the heart of our experimental setup is an atom chip, a micro-fabricated wire pattern on a silicon substrate used to generate magnetic potentials. It allows for trapping of atoms in strong magnetic gradients at a distance of a few to a few hundred micrometers from the chip surface. A 1D potential is formed by strongly increasing the confinement in the two spatial dimensions perpendicular to the field-generating wire. In this way the motion of the atoms is restricted to only one dimension.

To achieve the aforementioned conditions for a two-component Bose gas, besides ultracold temperatures and low atomic densities, control over the interatomic interactions is

required. Traditionally, interactions among ultra-cold atoms are controlled via Feshbach resonances by changing the background magnetic field. Since the magnetically trappable states of ^{87}Rb do not have any convenient Feshbach resonances, we developed a novel approach to tuning the interactions between atoms in 1D gases by means of radio-frequency dressed potentials.

By applying radio-frequency fields, we couple the original state to all states within the same hyperfine manifold, resulting in a modified (dressed) potential. The coupling depends on the ellipticity of the RF polarization through the sign of the g-factor of the atomic state. Since the clock states have opposed g-factors and we can tune the RF polarization, the dressed potentials are state-dependent.

In 1D Bose gases, the effective interactions between atoms depend on the trapping potential. We exploit the state-dependence of RF dressed potentials to tune the effective inter- and intrastate atomic interactions. This technique provides access to the point of spin-independent interactions where exact quantum many-body solutions are available and the point where spin motion is frozen. As the main result of this work, we show the corresponding time evolutions of the spin polarization derived from state-selective absorption images. A simulation based on coupled 1D Gross-Pitaevskii equations yields excellent agreement with the data.

This technique developed in this work paves the way for new experiments on 1D many-body physics. The natural next step is to extend our studies to Bose-Fermi mixtures. The corresponding design of the next generation experimental apparatus is presented in the last chapter. In a wider sense, tuning interactions in 1D Bose gases could lead to accuracy improvements in (atom chip based) atomic clocks and prove beneficial to quantum computing schemes.

Samenvatting

Wanneer atomen afgekoeld worden tot temperaturen dicht bij het absolute nulpunt (ongeveer 150 nanokelvin in ons geval), wordt hun kwantumstatistiek duidelijk zichtbaar. Afhankelijk van of het totale aantal samenstellende protonen, neutronen en elektronen in het atoom even of oneven is, is het atoom respectievelijk een boson of een fermion. Wanneer ze worden gevangen en afgekoeld in een externe potentiaal, condenseren bosonen in de kwantummmechanische grondtoestand, en kunnen ze beschreven woren als een coherente materiegolf die Bose-Einstein condensaat (BEC) genoemd wordt. Fermionen, daarentegen, zijn onderworpen aan Pauli's uitsluitingsprincipe dat verbiedt dat twee identieke fermionen dezelfde kwantumtoestand bezetten. Daarom worden in een koud Fermi gas alle kwantumtoestanden tot een bepaalde energie bezet door precies één atoom. De meeste experimenten met kwantumgassen (BECs en Fermi gassen) worden uitgevoerd met vallen die beweging in alle drie de richtingen toestaan. Het hier beschreven werk draait om ééndimensionale (1D) bosonische kwantumgassen, waarin de atomen zo zijn opgesloten dat ze slechts in één richting kunnen bewegen.

Eéndimensionale kwantumgassen vertonen verschijnselen die niet in hun 2D en 3D evenbeelden aanwezig zijn. Bijvoorbeeld: een 1D Bose gas wordt sterker wisselwerkend als de dichtheid afneemt. Onder specifieke omstandigheden kunnen deze 1D systemen worden beschreven door exact-oplosbare modellen, terwijl de beschrijving van systemen met hogere dimensie inherent benaderingen nodig heeft.

In spinor quantumgassen kunnen de atomen meerdere interne toestanden bezetten. Dit biedt de mogelijkheid om de wisselwerking tussen interne (spin) en externe (beweging) vrijheidsgraden te bestuderen. Deze wisselwerking is belangrijk in algemeen relevante en uitdagende fenomenen zoals kwantummagnetisme.

In onze experimenten, die allemaal zijn uitgevoerd met een specifiek, bosonisch isotoop van rubidium, ^{87}Rb, maken we een twee-component (spinor) Bose gas in een 1D potentiaal. De gebruikte toestanden zijn de twee kloktoestanden van ^{87}Rb die dezelfde magnetische valpotentiaal ondergaan. In het hart van onze experimentele opstelling bevindt zich een atoomchip, een gemicrofabriceerde structuur op een silicium substraat die wordt gebruikt om magnetische potentialen te maken. Deze maakt het mogelijk om atomen te vangen in sterke magnetische gradiënten op een afstand van enkele tot enkele honderden micrometers van het chip-oppervlak. Een ééndimensionale potentiaal wordt gevormd door de opsluiting in twee ruimtelijke richtingen loodrecht op de veldmakende draad sterk te vergroten. Op deze manier wordt de beweging van de atomen beperkt tot slechts één dimensie.

Om de bovengenoemde omstandigheden te bereiken voor een twee-components Bose gas is, naast ultralage temperaturen en lage atomaire dichtheden, ook controle over de interatomaire wisselwerkingen nodig. Traditioneel worden de wisselwerkingen tussen ultrakoude atomen ingesteld via Feshbach resonanties door het achtergrondmagneetveld te varieren. Aangezien de magnetisch vangbare toestanden van ^{87}Rb geen geschikte Feshbach resonanties hebben, hebben wij een nieuwe methode ontwikkeld om de wisselwerkingen tussen atomen in 1D gassen te variëren door middel van radio-frequente “aangeklede” (“dressed”) potentialen.

Door radio-frequente velden aan te leggen, koppelen we de oorspronkelijke toestand met alle andere Zeeman-subniveaus binnen dezelfde hyperfijn toestand, en dit resulteert in een veranderde (aangeklede) potentiaal. De koppeling hangt af van de ellipticiteit van de RF polarisatie via het teken van de g-factor van de atomaire toestand. Omdat de kloktoestanden tegengestelde g-factoren hebben en we de RF polarisatie kunnen variëren, zjin de aangeklede potentialen toestandsafhankelijk.

In 1D Bose gassen hangen de effectieve wisselwerkingen tussen de atomen van de valpotentiaal af. We maken gebruik van de toestandsafhankelijkheid van de met RF aangeklede potentialen om de effectieve atomaire wisselwerkingen te verstemmen, zowel tussen de toestanden (inter-state) als binnen dezelfde toestand (intra-state). Deze techniek geeft toegang tot het punt van spin-onafhankelijke wisselwerkingen waar exacte kwantumveeldeeltjesoplossingen beschikbaar zijn, en tot het punt waar de spinbeweging bevroren is. Als hoofdresultaat van ditw erk laten we de corresponderende tijdsevolutie van de spinpolarisatie zien, afgeleid van toestandsafhankelijke absorptiebeelden. Een simulatie gebaseerd op gekoppelde Gross-Pitaevskii vergelijkingen geeft uistekende overeenkomst met de metingen.

De techniek die hier is ontwikkeld maakt de weg vrij voor nieuwe experimenten aan 1D veeldeeltjesfysica. De natuurlijke volgende stap is het uitbreiden van ons werk naar Bose-Fermi mengsels. Een daarbij passend ontwerp voor de volgende generatie van de experimentele opstelling wordt gepresenteerd in het laatste hoofdstuk. In bredere context zou het verstemmen van wisselwerkingen in 1D Bose gassen kunnen leiden tot verbeterde nauwkeurigheid van (op atoomchip gebaseerde) atoomklokken en zou het voordeel kunnen bieden bij bepaalde ontwerpen voor kwamtumcomputers.

Zusammenfassung

Wenn Atome bis kurz vor den absoluten Nullpunkt (in unserem Fall bis ungefähr 150 Nanokelvin) gekühlt werden, wird ihre Quantenstatistik sichtbar. Abhängig davon, ob die Gesamtanzahl der einzelnen Protonen, Neutronen und Elektronen gerade oder ungerade ist, ist das Atom ein Boson oder ein Fermion. Gefangen in einem externen Potential, neigen gekühlte Bosonen dazu, in den quantenmechanischen Grundzustand zu kondensieren und können als eine kohärente Materiewelle, genannt Bose-Einstein Kondensat (BEC), behandelt werden. Fermionen unterliegen dem Pauli'schen Ausschlussprinzip, welches zwei identischen Fermionen verbietet, den selben Quantenzustand einzunehmen. Aus diesem Grund werden in einem kalten Fermigas alle Quantenzustände bis zu einer bestimmten Energie mit exakt einem Atom besetzt. Die meisten Experimente mit Quantengasen (BECs und Fermigasen) werden mit Fallen durchgeführt, die eine Bewegung der Atome in allen drei Raumrichtungen erlauben. Der Fokus dieser Arbeit liegt bei eindimensionalen (1D) bosonischen Quantengasen, in welchen die Atome so eingeschlossen werden, dass sie sich nur noch entlang einer einzigen Richtung bewegen können.

Eindimensionale Quantengase weisen Phänomene auf, die in 2D- oder 3D-Gasen nicht vorkommen. Zum Beispiel wird die Wechselwirkung zwischen den Atomen in einem 1D Bosegas stärker, wenn dessen Dichte abnimmt. Unter besonderen Bedingungen können diese 1D-Systeme durch exakt lösbare Modelle beschrieben werden, während Systeme mit höherer Dimensionalität nur mithilfe von Näherungen beschrieben werden können.

In Spinor-Quantengasen können die Atome mehrere interne Zustände einnehmen. Dadurch wird es möglich das Wechselspiel zwischen (internen) Spin- und (externen) Bewegungs-Freiheitsgraden zu untersuchen. Dieser Zusammenhang spielt eine wichtige Rolle bei anspruchsvollen Phänomenen wie zum Beispiel dem Quantenmagnetismus.

In unseren Experimenten arbeiten wir mit dem bosonischen Rubidium-Isotop ^{87}Rb. Wir erzeugen ein zweikomponentiges (Spinor-) Bosegas in einem 1D-Potential. Die dabei verwendeten Zustände sind die "clock"-Zustände von ^{87}Rb, die das gleiche magnetische Fallenpotential erfahren. Das Herz unseres experimentellen Aufbaus ist ein Atomchip, eine mikrofabrizierte Struktur elektrischer Leiterbahnen auf einem Siliziumsubstrat, die verwendet wird um magnetische Potentiale zu generieren. Der Atomchip ermöglicht das Fangen von Atomen in starken magnetischen Gradientenfeldern im Abstand von einigen wenigen bis zu einigen Hundert Mikrometern zur Oberfläche des Chips. Das eindimensionale Potential wird durch eine starke Erhöhung der Fallengradienten in den zwei Raumrichtungen senkrecht zum felderzeugenden Leiter geformt. Auf diese Weise wird die Bewegung der Atome auf nur eine Dimension beschränkt.

Um die oben erwähnten Bedingungen für ein zwei-komponentiges Bosegas zu erfüllen, wird neben ultra-kalten Temperaturen und geringer Atomdichte auch Kontrolle über die interatomaren Wechselwirkungen benötigt. Traditionell werden Wechselwirkungen zwischen ultra-kalten Atomen über Feshbach-Resonanzen kontrolliert, welche wiederum über das magnetische Feld eingestellt werden. Da ^{87}Rb keine geeigneten Feshbach-Resonanzen in den magnetischen fangbaren Zuständen aufweist, haben wir eine neue Methode entwickelt, bei der die Wechselwirkung zwischen den Atomen eines 1D-Gases mithilfe von Radiofrequenz(RF)-Potentialen eingestellt wird.

Hierfür verwenden wir Radiofrequenzfelder, um den urspünglichen Zustand mit allen Zuständen derselben Mannigfaltigkeit zu koppeln und somit ein modifiziertes Potential ("dressed potential") zu erzeugen. Die Kopplung hängt dabei via das Vorzeichen des g-Faktors des Atomzustands von der Elliptizität der RF-Polarisation ab. Da die "clock"-Zustände entgegengesetzte g-Faktoren haben und wir die RF-Polarisation beliebig einstellen können, sind die so modifizierten Potentiale zustandsabhängig.

In 1D-Gasen hängen die effektiven Wechselwirkungen vom Fallenpotential ab. Wir nutzen die Zustandsabhängigkeit der RF-Potentiale, um die effektiven Wechselwirkungen zwischen Atomen desselben Zustands, sowie zwischen Atomen unterschiedlichen Zustands einzustellen. Diese Technik ermöglicht das Einfrieren der Spinbewegung sowie das Untersuchen der spin-unabhängige Wechselwirkungen, für die exakte Vielteilchen-Lösungen existieren. Als Hauptresultat dieser Arbeit zeigen wir die entsprechende zeitliche Entwicklung der Spinpolarisation, die wir aus zustandsabhängigen Absorptionsbildern bestimmt haben. Eine Simulation, basierend auf gekoppelten 1D-Gross-Pitaevskii Gleichungen, zeigt eine hervorragende Übereinstimmung mit unseren Daten.

Die im Rahmen dieser Arbeit entwickelte Technik ermöglicht neue Experimente im Bereich der eindimensionalen Vielteilchenphysik. Unser nächster Schritt wird es sein, unsere Untersuchungen auf Bose-Fermi-Gemische auszuweiten. Das Design für einen entsprechenden experimentellen Aufbau ist Gegenstand des letzten Kapitels. Im weiteren Sinne kann die Forschung an 1D Bosegasen zu Verbesserungen der Genauigkeit von Atomchip-basierten Atomuhren führen und einen Beitrag zur Entwicklung von Quantencomputern leisten.

Acknowledgements

This work was aided and supported in many different ways and by numerous people from both, professional and private circles. Trying to come up with a comprehensive list, I would almost certainly forget someone. Therefore, before I nevertheless give the list a try, I want to express my gratitude to each and everyone who helped me during my line-land adventures in the flatlands.

First of all, I want to thank my supervisor and co-promotor Klaasjan van Druten for his support and perseverance. Klaasjan, what I have learned from you during the last years goes far beyond the often one-dimensional world of quantum gases and extends into such strange fields as dutch society. Also, I am very happy about the freedom you granted me in running the lab. Finally, I want to thank you for your trust and for giving me the opportunity to work with you on this exciting subject. I thank Jook Walraven for being a great promotor by cherishing every possible problem and helping to solve it.

Aaldert van Amerongen and Jan-Joris van Es, you made me feel very welcome right from the start. I very much enjoyed working with you and I benefitted a lot from you by inheriting a very well-designed and reliable setup. A special thank goes to JJ for consistently refusing to speak English with me after some fence time and thereby giving my Dutch language skills a big boost.

Shannon Whitlock, during endless hours in the lab, the Kriterion conference room and traveling all over Europe you shared your motivation, passion for science, insights and humor with me. You taught me your way to break down the most complex problems into small units. Thank you for being the best imaginable postdoc out there.

Thanks to the whole quantum gases group: Ben van Linden van den Heuvell (your Mathematica wizardry made me feel like a sorcerer's apprentice), Robert Spreeuw, Tom Hijmans (your view on science often helped me to put things into perspective), Sebastian Kraft, Thomas Fernholz, Frederik Spiegelhalder, Vanessa Leung, Wojtek Lewoczko-Adamczyk (I wish you all the best for continuing the experiment, maybe we meet again on a Greek island one day), Tobias Tiecke, Vlad Ivanov, Rene Gerritsma, Antje Ludewig (my trusted companion on the physics journey, thanks for making landing and take-off in Amsterdam and even more so the time in between a pleasure with your support and friendship), Paul Cleary, Carolijn van Ditzhuijzen, Richard Newell (I already start missing your humour), Atreju Tauschinsky, Rutger Thijssen, Caspar Ockeloen and Lynn Hoendervanger (you have been a topnotch master student). Together you created a very cooperative and cordial atmosphere, that I enjoyed working in. I wish you success with your current and

future projects.

I want to thank Jean-Sébastien Caux for the close collaboration on exactly solvable 1D systems and his endless patience in explaining them. Furthermore, he deserves praise for choosing Pasquale Calabrese, Alexandre Faribault, Guillaume Palacios and Antoine Klauser as his staff. I am thankful to all of them for their contributions both inside and outside university. Also, I am grateful to Gora Shlyapnikov for supporting our work.

Without the help and professional work of all the people at both, the mechanical and the electronics workshop, this work would have been unthinkable. Thanks to all of you for understanding the needs of a PhD student who sometimes asked you to deliver next-to-impossible contraptions yesterday. I want to thank Hans Agema for his exceptional efforts to help us acquire and operate the microwave equipment. Thanks to Rita Vinig, Ineke Baas and Luuk Lusink not only for making administrative matters as easy as possible, but also for their interest in my progress.

My housemates had to bear me in many different states throughout the last years. Thank you Alessia, Nadine and Britta for the good times and for making KP4 the home it has been to me. Hendrik, I simply want to thank you for being the friend that you are (the list would be too long). I want to thank Salvo, Nacho, Manu, Miranda, Diego, Rob, Javier, Sara, Bahar, Salima, Tommaso, Stefania, Raffa, Mariangela, Véro, Sarah, Adriel, Steffi, Silke, Marc, Bernadette, Stefan, Lisa, Bas, Alwin, Gert, Maya, Jens, Giuliana, Thetis and a lot more people for all the good times we had together in Amsterdam. Big ups to everyone at Crunch for keeping my body in shape by making me run really hard for that frisbee. Keep up the good spirit. Amsterdam, I want to thank you for being the great city that you are, for your quality of living, for the fun I had riding everywhere by bicycle, for all the open-minded, international people you made me meet and finally for making me feel at home. You should should work on your weather, though. A big thank goes to all my friends in Germany for their moral support, for providing shelter whenever needed and for occasionally delivering a very welcome loaf of proper bread. I want to thank my brother Jona for knowing how to handle his brother and for often enough infecting him with his cheerfulness.

Dear Katja, my private reason, I thank you for your endless patience and trust, for your joyful smiles, for understanding me and finally for the place you give me in your life.

As long as I can think my parents have encouraged me to go my own way and supported me in all possible ways regardless of what I was doing, with this thesis being no exception. Thank you!

List of publications

- J Fortágh, S. Kraft, A. Günther, C. Trück, P. Wicke, and C. Zimmermann. Perspectives of ultracold atoms trapped in magnetic micro potentials. *Opt. Commun.*, 243:45–56, 2004.
- S. Kraft, A. Gunther, P. Wicke, B. Kasch, C. Zimmermann, and J. Fortágh. Atom-optical elements on micro chips. *Eur. Phys. J. D*, 35:119–123, 2005.
- A. H. van Amerongen, J. J. P. van Es, P. Wicke, K. V. Kheruntsyan, and N. J. van Druten. Yang-Yang thermodynamics on an atom chip. *Phys. Rev. Lett.*, 100:090402, 2008.
- J. J. P. van Es, P. Wicke, A. H. van Amerongen, C. Rètif, S. Whitlock, and N. J. van Druten. Box traps on an atom chip for one-dimensional quantum gases. *J. Phys. B: At. Mol. Opt. Phys.*, 43:155002, 2010.
- P. Wicke, S. Whitlock, and N. J. van Druten. Controlling spin motion and interactions in a one-dimensional Bose gas. *arXiv*, cond-mat:1010.4545, 2010.